Forschungszentrum Jülich
in der Helmholtz-Gemeinschaft

Institut of Bio- and Nanosystems

Label-free detection of biomolecules by a field-effect transistor microarray biosensor with bio-functionalized gate surfaces

Yinhua Han

Jül-4227

Label-free detection of biomolecules by a field-effect transistor microarray biosensor with bio-functionalized gate surfaces

Yinhua Han

Berichte des Forschungszentrums Jülich ; 4227
ISSN 0944-2952
Institute of Bio- and Nanosystems Jül-4227
D 82 (Diss., RWTH Aachen, 2006)

Zu beziehen durch: Forschungszentrum Jülich GmbH · Zentralbibliothek, Verlag
D-52425 Jülich · Bundesrepublik Deutschland
☎ 02461 61-5220 · Telefax: 02461 61-6103 · e-mail: zb-publikation@fz-juelich.de

Abstract

The aim of this work was to bio-functionalize the SiO_2 gate of ion-sensitive field-effect transistor (ISFET) to covalent bind DNA sequences via a series of chemical reactions. On the modified surface, the detection of the DNA hybridization and in particular single nucleotide polymorphism (SNP) detection was achieved. Furthermore, to explore the working principle of the field-effect detection, polyelectrolyte multilayers (PEMs) buildup and recognition reaction of biotin and streptavidin were also analyzed with the ISFET biosensors.

Up to now, labeling detection systems dominated the DNA detection bioassays. Here either the probe or the catcher DNA are labeled with fluorescence-, radioactive- or enzymatic-labels. In recent years, many new approaches for signal generation that avoid labeling have been reported. Based on the demand of a fast, cheap, highly sensitive, label-free and direct electronic readout, ISFET biosensor are ideally suited.

In my work, I started with bio-functionalization of SiO_2 control substrates, leading to a covalent binding of the probe biomolecules, i.e. single stranded DNA and biotin. In this surface modification process, a step-by-step protocol was setup, firstly cleaning/activation with MeOH/HCl for 30 mins generated the highest -OH bond density. Secondly, silanization with 3-aminopropyltriethoxysilane (APTES) in gas phase left a thinner, more homogeneous silane layer. Crosslinking with succinic anhydride solution for 2 hours controlled the following DNA immobilization. The DNA position-specific microarrays for hybridization detection were fabricated by a custom-made aligned microspotter system. The DNA-DNA hybridization has higher efficiency in higher ionic strength solution (SSC buffer solution) and higher selectivity for SNP detection in lower ionic strength TE buffer solutions. All bioassay protocols were successfully transferred to the fully encapsulated ISFET devices and were “mild” enough for the encapsulation material of the chips.

In the direct current (DC) readout, ISFETs as a potentiometric biosensors monitor the change of the solid/liquid interface potential caused by the attachment of biomolecules. To investigate the detection principle of the ISFETs in general, polyelectrolyte multilayers (PEMs) were used as a model system. During the layer-by-layer buildup, the thickness of the PEMs and the outer charge of the layer system are changing, which can be recorded by the ISFETs. The recorded results confirmed the surface charge sensitivity of the ISFETs.

With increasing distance away from the surface, the charge detection of the ISFETs decreased exponentially.

To reduce the long-term drift of the FET readout and exclude possible side effects from temperature, pH changes, and buffer solutions etc., a reference chip or a reference channel were used to perform differential readout detections. The DNA immobilization between covalent binding and electrostatic adsorption caused a gate voltage change of 4mV. It confirmed that the covalent binding of DNA immobilization introduced a higher surface coverage compared to the electrostatic adsorption. The differential DNA hybridization between a perfect matched (PM) and a fully mismatched (FMM) probe sequence also gave a clear signal. However, the SNP is barely distinguishable in DC readout as potential changes.

Therefore, ISFETs as impedimetric biosensors were developed to record the impedance change at the gate input in an alternating current (AC) mode. In the optimized detection solution, a reliable recording of ex-situ SNP was achieved and in-situ detection showed DNA hybridization kinetically. In the first proof of principle experiment, the adding of gold-nanoparticle (AuNPs) to the target DNA did not enhance the selectivity of the SNPs detection, which confirmed the valid charge sensitive of ISFET in electrical double layer. Furthermore, in-situ and ex-situ measurements of biotin/streptavidin binding revealed distinct effects on the transfer function curves.

The recordings of the multilayer buildup in AC and DC readouts modes offered details for the principle explanation of the signals and evidence about the main components in the equivalent circuit simulations. The main parameters such as contact lane capacitance and solution resistance were firstly identified and the influence of a biomembrane attached to the ISFET gate was in a first approximation modeled.

Zusammenfassung

Das Ziel dieser Arbeit war die Biofunkionalisierung von SiO_2 Gates in ionensensitiven Feldeffekttransistoren (ISFET), um DNA Sequenzen kovalent durch eine Reihe von chemischen Reaktionen zu binden. Es gelang, DNA Hybridisierung und insbesondere Einzel-Nukleotid- Polymorphismen auf der modifizierten Oberfläche nachzuweisen. Des weiteren wurde, um das Prinzip der Feldeffektdetektion zu untersuchen, der Aufbau von Polyelektrolyten sowie die Detektion von Biotin und Streptavidin Reaktionen mit den ISFET Biosensoren analysiert.

Bis jetzt haben Systeme basierend auf dem Etikettierungsansatz den Markt der DNA Bioassays dominiert. Bei diesem Verfahren wird entweder die Sonden oder Ziel-DNA mit einer fluoreszierenden, radioaktiven oder enzymatischen Markierung versehen. In den letzten Jahren sind viele alternative Verfahren vorgestellt worden, die das Markieren umgehen. Basierend auf der Nachfrage nach schnellen, billigen, höchst empfindlichen und markierungsfreien Systemen ist der ISFET Biosensor bestens geeignet.

In meiner Arbeit habe ich mit der Biofunktionalisierung von SiO_2 Kontrollsubstraten begonnen. Dies funkionalisierung führt zu einer kovalenten Bindung des Probenmoleküls z.B. Einzelstrang DNA und Biotin. Für diese Oberflächenfunktionalisierung wurde ein Protokoll eintwickelt, das aus folgenden Schritten besteht: Zuerst wir die Probe mit MeOH/HCL für 30 min gesäubert und aktiviert. Dies generiert die höchste Dichte an -OH Bindungen. In einem zweiten Schritt hinterlässt die Silanisierung mit 3-aminopropyltriethoxysilane (APTES) aus der Gasphase eine dünne und homogene Silanschicht. Eine Vernetzung mit succinic anhydride Lösung für zwei Studen kontrollierte die darauffolgende DNA Immobilisierung. Die DNA positionsspezifischen Matrizen für die Hybridisierungsdetektion, wurden mittels eines Microspottersystems hergestellt. Die DNA-DNA Hybridisierung hat eine höhere Effiktivität in Lösungen mit einer hohen Ionenstärke (SSC Pufferlösung) und eine höhere Selektivität für SNP Detektion in Lösungen mit einer geringen Ionenstärke (TE Pufferlösungen). Alle bioassay Protokolle wurden erfolgreich für verkapselte ISFETs adaptiert.

Bei der Gleichstrommessung, arbeiten die ISFETs als ein potientiometrischer Biosensor, welcher die Veränderung des Potentials der fest/flüssig Grenzschicht detektiert. Dieses Potential wird durch ein andockendes Biomolekül verändert. Um das generelle Detektionsprinzip zu untersuchen wurden Polyelektrolyte als Modellsystem verwendet.

Während das lagenweisen Aufbaus, verändern sich die Dicke und Ladung des PEM systems. Dies kann mit ISFET detektiert werden. Die Aufnahmen bestätigten die Oberflächenladungsempfindlichkeit des ISFETs. Mit zunehmenden Abstand von der Oberfläche, nahm die Ladungsdetektion exponentiell ab.

Um die Langzeitdrift des FETS zu reduzieren und um mögliche unerwünschte Einflüsse von Temperatur, pH Wert, Pufferlösung etc. zu verhindern wurde ein Referenzchip oder Referenzkanal für eine differentielle Messung benutzt. Die DNA Immobilisierung zwischen kovalenter Bindung und elektrostatischer Absorption resultierte in einer Änderung der Gatespannung um 4mV. Dies bestätigte, dass die kovalente Bindung der DNA Immobilisierung eine bessere Flächenabdeckung herbeiführte, als eine elektrostatische Absorption. Die differentielle DNA Hybridisierung zwischen einer perfekt übereinstimmenden Probe (PM) und einer vollkommen fehl angepassten Probe (FMM) gab auch ein klares Signal. Allerdings ein Einzel-Nukleotid-Polymorphismus nur schwer im Gleichstrommodus zu erkennen.

Darum wurden impedimetrische ISFETs entwickelt, mittels denen die Veränderung der Impedanz im Wechselstrombereich am Gate gemessen werden konnte. In der optimierten Detektionslösung wurde eine verlässliche Methode gefunden um ex-situ Einzel-Nukleotid-Polymorphismen nachzuweisen. In-Situ Messungen zeigten die Kinetik der DNA Hybridisierung. In einem ersten “Proof of principle“ Experiment wurde die Selektivität für die Detektion von Einzel-Nukleotid Polymorphismen durch Zugabe von gold Nanopartikeln nicht verbessert. Dies bestätigte die korrekte Ladungsempfindlichkeit im ISFET “double layer“. Des weiteren wurde in in-situ und exsitu Messungen von Biotin/Streptavidin Bindungen eine klare Veränderung der Transferkennlinie beobachtet.

Die Aufnahmen des Multilagenaufbaus im Gleichstrom- und Wechselstrombereich ergaben Hinweise auf das Funktionsprinzip der Detektion sowie erste Größen für die Komponenten im elektrischen Ersatzschaltbild. Die Hauptparameter wie Leiterbahnkapazität und Widerstand der Lösung wurden identifiziert und der Einfluss einer angehefteten Biomembrane auf dem ISFET wurde in erster Näherung simuliert.

Table of Contents

Acknowledgements

I would like to thank everyone who supported me and my work, and I would especially thank:

Dr. Sven Ingebrandt for his supervision, support and encouragement in the past three years. He taught by personal example as well as verbal instruction. His instruction and scientific sprit will be a benefit to my future career and my whole life.

Prof. Dr. Andreas Offenhäusser for his support, and the opportunity to obtain a doctoral degree at the RWTH Aachen in Germany. He was always patient to any question, and directed the process of the experiments pivotally. From him I gained not only the academic knowledge but also insight into the art of scientific management.

Prof. Dr. Christoph Buchal who introduced me to this group IBN2-BE and brought me a new life in Germany.

The whole DNA-FET group: Dr. Fumio Nakamura and my co-working students, Manu Mathew-Kottupallil, Malla Reddy Sakkari, Maryam Hadji Abouzar. I appreciated the moments we were working together.

Dr. Dirk Mayer and Frank Amberger for the AFM measurements.

Dirk Borstlap, Regina Stockmann, and Michael Prömpers for fabrication of the FET chips.

Rita Helpenstein and Stephan Schaal for routine working help in the laboratory.

Dr. Simone Böcker-Meffert for the discussions about biology in general.

R. Otto, N. Wolters, D. Lomparski (IBN2-Electronic Workshop) and D. Strobl and Dr. Herbert Bousack (IBN2-Mechanical Workshop).

Prof. Dr. Ulrich Simon and Eva Koplin (Department of Chemistry, RWTH Aachen) for providing the gold-nanoparticle modified DNA sequence.

Dr. Astrid Besmehn and Dr. Stephan Küppers (ZCH, Forschungszentrum Jülich) for the XPS measurements.

Bo Han and PD Thomas Wandlowski (IBN-3, Forschungszentrum Jülich) for the FT-IR measurements.

Finally, I would like to thank my husband Haoyu Wu, who quitted his fine job and cozy life, came to support me abroad. His love restores my working enthusiasm and strength every day. I am also indebted to my parents for their inspiration and constant support.

Chapter I Introduction

The last two decades witness an extraordinary growth in research on sensors especially chemical and biochemical sensors. In its classical definition, a biosensor is an analytical device containing an immobilized biological sensitive material (enzyme, antibody, antigen, organelles, DNA, cells, tissues or organic molecules) integrated within a transducer. It ultimately converts the biological information into a quantitatively measurable signal usually in the form of optical, acoustic, electrical or magnetic responses. The biosensor technology involves the disciplines of physics, chemistry, biochemistry and electronics. Highly multidisciplinary research work is needed for the development of up-to-date biosensors. This includes the life science side such as pharmacology, protein chemistry, immunology, genetic engineering and biochemistry, and the physical science side, such as material science, nanotechnology, electronics, surface chemistry or more succinctly, physics (Collings et al. 1997).

Biosensors, especially DNA-biosensors are utilized to study the DNA-related phenomena. Since the discovery of the double-helix structure of Deoxyribose Nucleic Acid (DNA) by Waston and Crick (Watson et al. 1953), the research on DNA sensors has grown drastically. DNA as the basis of life can be transcribed to RNA, which is further translated to the protein structure. In nature, the proteins are involved in many functions from enzymatic catalysts, storage molecules, to mechanical support. For DNA biosensors, most detections employ the concept of DNA hybridization. Here single stranded DNA (ssDNA) molecules of known sequence (probe DNA) are immobilized on a surface in a microarray. The analyte ssDNA molecules (target DNA) perform a hybridization reaction based on the highly specific molecular recognition of the bases A and T (adenine/thymine), G and C (guanine/cytosine) via multiple hydrogen bonds. The hybridization plays an important role in transferring genetic information inside living systems. The hybridization reaction occurs perfectly if all bases along two ssDNA molecules are fully matching. The affinity of the two-ssDNA molecules is strongly decreasing when single nucleotide polymorphisms (SNP) or more base pairs along a DNA molecule are not matching.

DNA hybridization and detection of SNPs are important in genetic diseases, forensic investigation, medical diagnostics, clinical research, gene expression, and for the post-gene study. Conventional DNA detections are based on labelling methods (e.g. fluorescence-, radioactive- or enzymatic-labels) for either the probe or the target DNA such as the dominant commercial products from Affymetrix Inc., USA. The DNA hybridization results in the form of fluorescent microarray images are scanned and quantified with the Confocal Laser Scanning Microscopy technique.

In recent years, many new approaches for detection systems without any labelling have been reported. Optical biosensors such as surface plasmon resonance spectroscopy (SPR) (Flanagan et al. 1984) and Ellipometry (Defeijter et al. 1978) measure refractive index changes close to the interface caused by the interaction between the biomolecules and the biosensor surface. Microgravimetric sensors such as Quartz Crystal Microbalances (QCM) (Roederer et al. 1983) and cantilever based biosensors (Manalis et al. 2000) relate the mass change to the surface reaction.

An efficient DNA detection would be based on a fast, cheap, highly sensitive, label-free and ideally direct electronic readout. Various electroanalytical methods are sorted into potentiometry (Krull et al. 1986), amperometry (Loffler et al. 1991), voltammetry (Ford et

al. 1982) and impedimetric biosensors (Katz et al. 2003) to perform quantitative and qualitative bioanalysis.

Field-effect transistor (FET) devices (Bergveld 1996) are a promising approach for potentiometric or impedimetric biosensors to detect all kinds of biomolecules. The ion-selective FET (ISFET) structure is derived from the design of the metal-oxide-semiconductor FET (MOSFET). Various research groups are utilizing the ISFET biosensor with a potentiometric readout to perform the DNA detection. Different gate materials such as SiO_2, Si_3N_4 (Sakata et al. 2004; Sakata et al. 2005a; Sakata et al. 2005b), Au (Kim et al. 2004a; Kim et al. 2004b; Shin et al. 2004), Ta_2O_5 (Ohtake et al. 2004a; Uno et al. 2004) are used.

As potentiometric biosensors, ISFETs monitor the change of the solid/liquid interface potential caused by the DNA hybridization process. During the DNA hybridization process, charges accumulate at the FET gates, because the DNA molecule is intrinsically negative charged. This charge accumulation shifts the flatband voltage of the transistors and hence the drain-source current, which can be recorded by a direct current (DC) readout. On the other hand, ISFETs can be utilized as impedimetric biosensors, which measure the impedance change at the gate input caused by the biomolecules. These impedance changes can be recorded in an alternating current (AC) mode, usually in the form of transfer function curves. In this work, ISFET biosensors with custom-made amplifiers, encapsulated chips, and a fully electronic readout system operated by a PC were developed, bio-functionalized and exploited as biomolecular sensors. Especially for the SNP detection during DNA hybridization, 8- or 16-channel ISFET arrays were fabricated with different gate sizes and pitches to optimize the sensitivity and selectivity. The system is capable of a synchronical and differential readout of all the channels.

The works in this thesis were divided into four parts. For the ISFETs used in this thesis, exclusively SiO_2 was used as gate material.

Firstly, a series of surface modification processes were applied to the fully encapsulated sensors leading to a covalent binding of the probe molecules. The surface modification includes cleaning/activation, silanization, crosslinking and covalent immobilization of the probes to the microarray chips. This step-by-step protocol was optimized and characterized with a variety of analysis methods including Contact Angle measurements (CA), Atomic

Force Microscopy (AFM), Fourier Transform Infrared Spectroscopy (FT-IR), Imaging Ellipsometry (IE), and X-ray Photoelectron Spectroscopy (XPS).

Secondly, based on this surface modification process, the DNA hybridization and SNP detection were performed in two different modes. In the DC mode, the surface potential changes related to the changes in surface charge were monitored. The hybridization process was detected as a function of the gate voltage. Multiple detections on eight channels were carried out simultaneously to distinguish between different probe sequences. The hybridization reaction at the modified sensor surfaces was optimized with fluorescently labeled target DNA. This protocol was adapted to the label-free assays with the ISFET chips.

Thirdly, to investigate the detection principle of the ISFETs, polyelectrolyte multilayers (PEMs) were used as a model system. During the layer-by-layer builtup, the thickness of the PEMs and the outer charge of the layer system are changing, which can be recorded by the ISFETs. Signal simulation with an equivalent electronic circuit model was done to interpreter the recordings.

At the end of this thesis, the binding reaction of biotin and streptavidin was also measured. For a correct interpretation of the signals, these systems are more complicated than PEMs or DNA. Biotin and streptavidin are more variable with pH, ionic strength, and temperature of the buffer solution. A more detailed study of these protein systems is needed to establish the fully electronic, label-free readout principle also for these bioassays.

Chapter II Bioelectronic sensor principles

Firstly invented by Bergveld et al (1970), the ion-sensitive field-effect transistor is derived from the metal-oxide-semiconductor field-effect transistor structure.

2.1 ISFET structure and field-effect principle

To understand the device characteristics of the ISFET biosensors, which were used in this work, a basic knowledge of the energy band diagram of solids is necessary.

2.1.1 Fermi level

Following the Pauli Exclusion Principle, electrons in solids are only present in energy bands. The difference between conductor, insulator and semiconductor materials can be explained with different energy band diagrams. Crucial for the conduction process of any material is whether there are electrons present in the conduction band. Seen from Fig 2.1,

in insulators, the electrons in the valence band are separated by a large energy gap from the conduction band and the conduction band is empty. In conductors like metals, the valence band overlaps the conduction band. In semiconductors, the energy gap between the valence and the conduction band is small enough to allow electrons by thermal or other excitations to enter the conduction band.

An important parameter in the band theory is the Fermi level, which is the highest occupied electron energy level at absolute zero degree Kelvin. The position of the Fermi level is located between the valence and conduction bands. Its position relative to the conduction band is a crucial factor in determining the electrical properties of a material. The Fermi distribution *W(E)* describes the occupation of the energy levels:

$$W(E) = \frac{1}{\exp(\frac{E - E_F}{kT}) + 1} \tag{1}$$

E is the energy level, which is occupied by electrons in thermal equilibrium at the temperature T. E_F is the Fermi level energy.

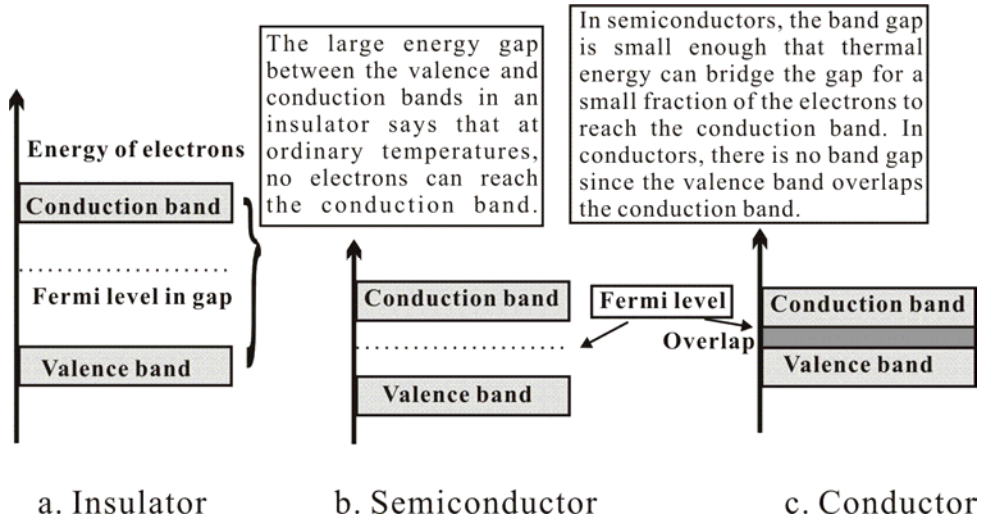

Fig 2.1 Schematic energy band distribution of electrons in three kinds of materials. The figure was adapted from (Sproull et al. 1990)

For the semiconductor materials, the Fermi energy can be modified by the doping concentration and other conditions. Doping of silicon can be realized by introducing a small percentage of impurity atoms into the silicon lattice. The introduction of atoms with five valence electrons (As, P) acts as electron donor and leads to n-type silicon. Materials with three valence electrons (B) are acting as electron vacancies and the silicon becomes

p-doped. Band diagrams for n- and p-doped semiconductors are shown in Fig 2.2.

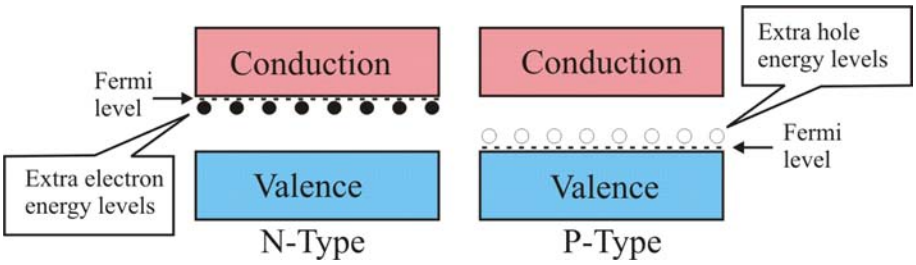

Fig 2.2 Fermi level and energy band diagram for n- and p-doped semiconductors. The figure was adapted from (Sproull et al. 1990)

In an n-type semiconductor, the highest occupied energy levels are near the top of the band gap. Therefore, electrons can easily be excited into the conduction band. In p-type semiconductors, extra energy levels in the band gap allow excitation of valence band electrons, leaving mobile holes in the valence band.

2.1.2 The metal-semiconductor structure

Based on the special properties of semiconductors, a FET with silicon was firstly designed as an amplifier by JE Lilienfeld (1930) and O. Heil (1939). The first application of a MOSFET was developed in 1950 (Shockley 1950).

In Fig 2.3 the schematics of a MOS structure is shown. In the MOS structure, the gate is comprised of a thin oxide layer and a top metal. An Ohmic contact is formed between the semiconductor and back contact allowing the application of bias voltage V_{GB} to the structure.

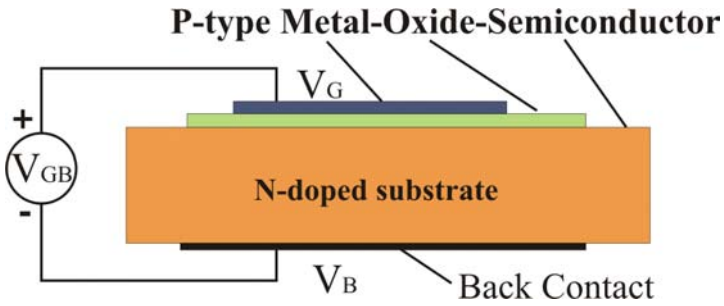

Fig 2.3 Cross section of a metal-oxide-semiconductor (MOS) structure

The metal-to-semiconductor contacts (MS junctions) are one of the most important components of a MOSFET. If the metal and the semiconductor are not in contact, the metal

workfunction Φ_M is equivalent to the energy difference between the vacuum energy and the Fermi level energy. The silicon workfunction Φ_s is variable depending on the doping of the silicon material. In contrast to this, the electron affinity is derived from the difference between the conduction band energy and vacuum energy, because the semiconductor conduction band energy is constant. The terms in Fig 2.4 are explained in Table 2.1.

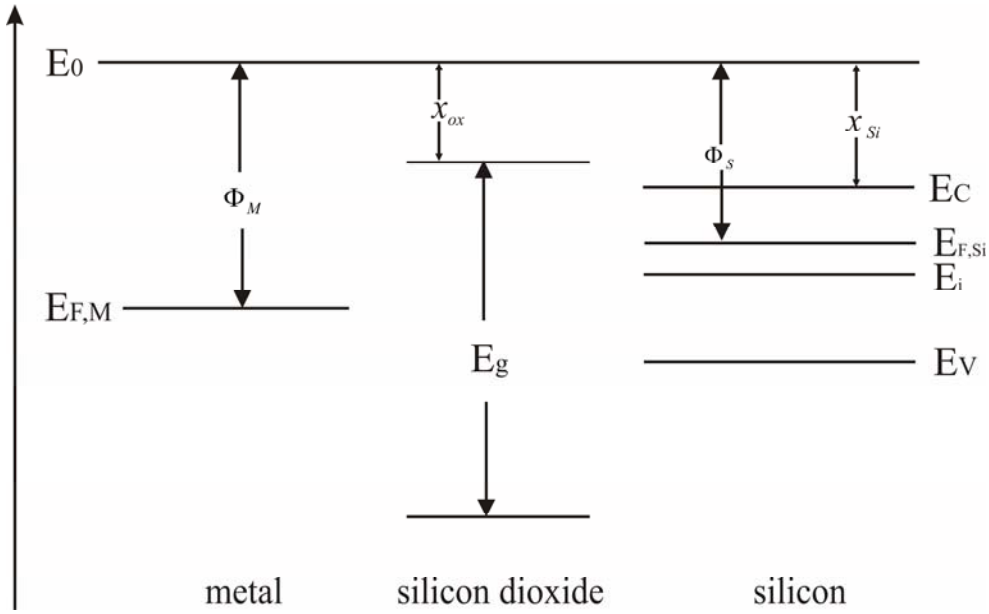

Fig 2.4 Flatband Energy diagram at thermal equilibrium for the ideal metal, the silicon dioxide and the silicon (Muller et al. 2003)

Table 2.1 Names and explanation of the terms in Fig 2.4

E_o	Vacuum energy	E_C	Conduction band energy
$E_{F,M}$	Fermi energy of metal	E_i	Intrinsic energy
Φ_M	Metal workfunction	$E_{F,Si}$	Fermi energy of semiconductor
Φ_S	Semiconductor workfunction	E_V	Valence band energy
E_g	gap energy	x	Electron affinity

Upon contact, the semiconductor and the metal act as plates of a capacitor. The electrons shift between the two materials to keep the Fermi levels at the same energy level. In reality, the flatband voltage of real structures is further affected by the fixed charge in the oxide Q_{ox} and at the oxide-semiconductor interface Q_{ss}.

The semiconductor workfunction is

$$\Phi_S = \chi + \frac{E_g}{2q} + \phi_B, \quad \frac{E_g}{2q} = E_V - E_C \tag{2}$$

The flatband voltage of the MOS structure is:

$$V_{FB} = \Phi_{MS} - \frac{Q_{ox} + Q_{SS}}{C_I} = \Phi_M - (\chi + \frac{E_g}{2q} + \phi_B) - \frac{Q_{ox} + Q_{SS}}{C_I} \tag{3}$$

with C_I being the interface capacitance. By convention, the silicon is held at ground potential.

Upon variation of the external voltage at the gate contact (V_G), the distribution of charge in the MOS capacitor shows the different situations of accumulation, depletion and inversion. Changing the voltage at the gate causes the voltage to reach the flatband voltage (V_{FB}), the threshold (V_T), and finally beyond the threshold voltage. The threshold voltage is reached, when the number of minority carriers exceeds the number of majority carriers (accumulation). Fig 2.5 displays the energy band diagram and charge situations for the three regimes of n-doped silicon.

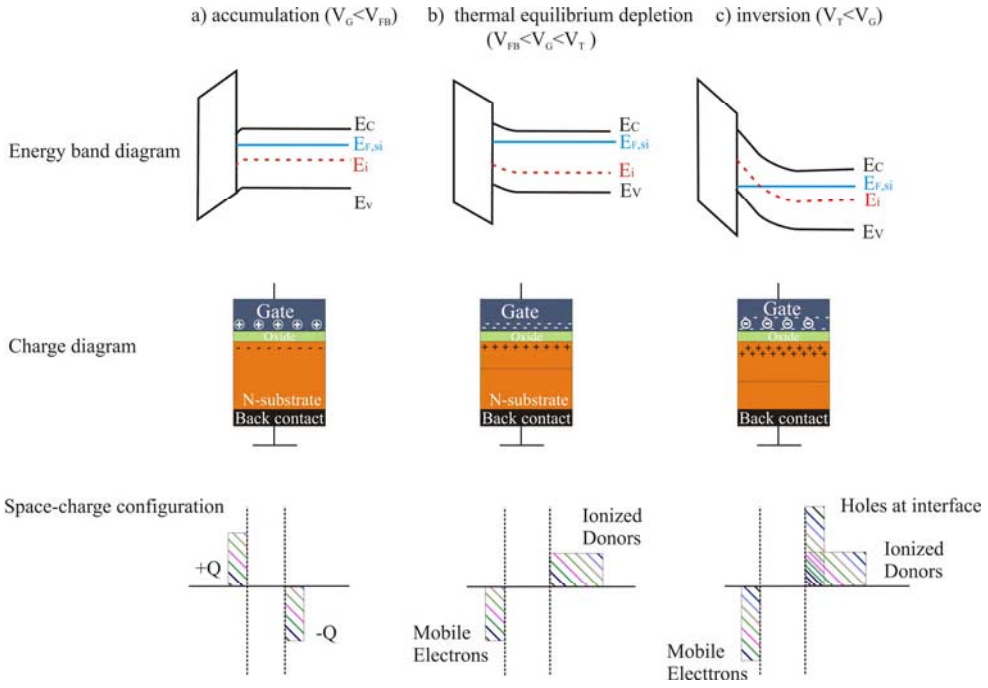

Fig 2.5 Band diagram of a MOS structure in the three different possible regimes (a) shows the accumulation case of positive gate voltage, where (b) shows the depletion for small negative gate voltages and (c) the inversion for higher negative gate voltages and their charge diagrams (Neamen 2003)

When the gate voltage is smaller than the flatband voltage ($V_G<V_{FB}$), the positive charge on the gate attracts the electrons from the substrate to the oxide-semiconductor interface. To a certain extent a band bending is needed to build up the accumulation charge so that almost all the potential variation occur within the oxide. Under this condition, a MOS structure acts still as a parallel plate capacitor structure (Fig 2.5a accumulation).

The voltage separating the accumulation and depletion regime is referred to as the flatband voltage V_{FB} (Eq. 3). When the bias voltage (V_G) is increased till the threshold voltage ($V_{FB}<V_G<V_T$), depletion occurs. The semiconductor is depleted of electrons at the interface, and a positive space charge region is induced. The interface region becomes resistive however electrons are still the majority carrier (Fig 2.5b depletion).

Finally, when the voltage exceeds the threshold voltage ($V_G>V_T$), more holes (minority carriers) are attracted to the surface, and the bands at the semiconductor bend more strongly. An inversion layer of holes forms when the voltage reaches the threshold voltage, (Fig 2.5c inversion). The threshold voltage (V_T) is reached, when the depletion region has reached the maximum thickness $x_{d,max}$ and the inversion starts. It is given by the flatband voltage subtracted by the build-in potential ϕ_B and the voltage across the oxide depending on the depletion layer charge:

$$V_T = V_{FB} - 2\phi_B - \frac{Q_{d,\max}}{C_{ox}} \tag{4}$$

in capacitance-voltage (CV) characterization measurements, the energy band and charged situations diagrams show the different regimes of accumulation, depletion and inversion. At the same time, the capacitances of in these three stages also change accordingly (Fig 2.6).

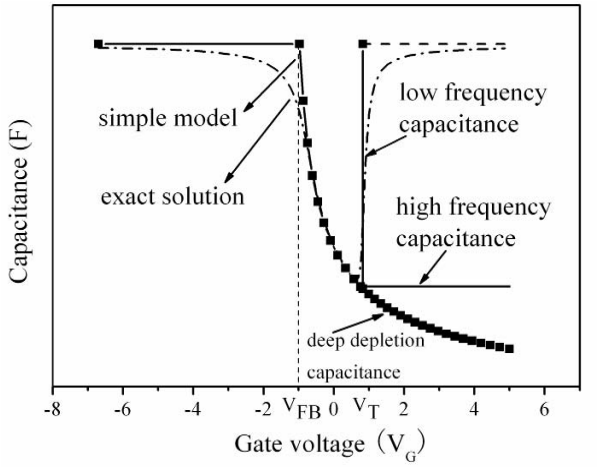

Fig 2.6 The capacitance of an nMOS capacitor changes with applied gate voltage. The exact solution (solid line) and the simple model (dotted lines) are reflecting the low and high frequency capacitance (2006a)

In the accumulation stage, there is no depletion layer present. The total capacitance of the MOS structure is then equal to the oxide capacitance

$$C = C_{ox} \tag{5}$$

In depletion, the capacitance of the MOS structure per unit area is determined by the series connection of oxide capacitance and the capacitance of the depletion layer,

$$C = \frac{1}{\frac{1}{C_{ox}} + \frac{x_d}{\varepsilon_s}} \tag{6}$$

x_d being the thickness of the variable depletion layer, and ε_s dielectric constant of the semiconductor. In the inversion stage, the total capacitance is dependent on the frequency. In the low frequency region, it equals the capacitance in the accumulation stage. In the high frequency regime, the capacitance is reduced. The capacitance is given by following Eqs., where the thickness of the variable depletion layer reaches the maximum $x_{d,max}$.

$$C_{LF} = C_{ox} \tag{7}$$

$$C_{HF} = \frac{1}{\frac{1}{C_{ox}} + \frac{x_{d,\max}}{\varepsilon_s}} \tag{8}$$

2.1.3 MOSFET structure and field-effect

The structure of an enhancement p-channel MOSFET is shown in Fig 2.7. In the pMOSFET structure, there are three terminals: gate (G), source (S) and drain (D). Two separated, p-doped regions form drain (D) and source (S). A channel of regular n-doped silicon is defined by diffusion between source and drain. The channel is covered by a thin metal layer, and the channel width (W) and length (L) are referred to width and length of the metal layer. When the inversion occurs, the charge carriers accumulate in a sufficient concentration under the gate oxide. The type of charge carriers responsible for the conduction of the channel is opposite to the substrate. The n-type substrate inverts into p-type and an inversion layer is formed. If a negative voltage is applied to the drain, a voltage drop occurs between drain and source, and current flows through the p-channel.

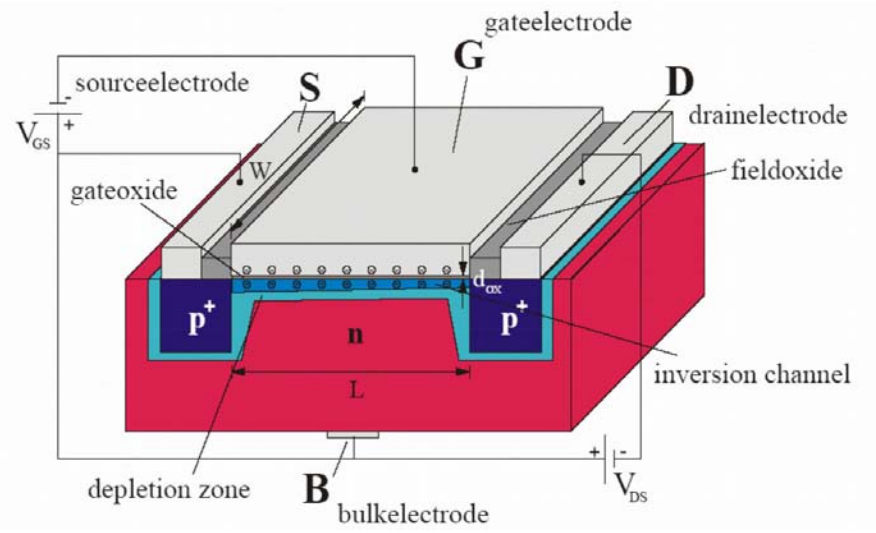

Fig 2.7 Schematical view of the structure and electrical contacts of the p-channel FET. The metal gate is isolated from the channel by a thin silicon dioxide layer (Ingebrandt 2001)

The MOSFET output signal, the drain current (I_D) is dependent on both the drain voltage (V_D) and the gate voltage (V_G). The operation of a MOSFET is characterized with I_D-V_D curves (output characteristics) (Fig 2.8). One of the most important parameter is the threshold voltage (V_T), which is the minimum gate voltage required to open the channel. When the gate voltage is more negative than V_T, positive charge is induced in the channel.

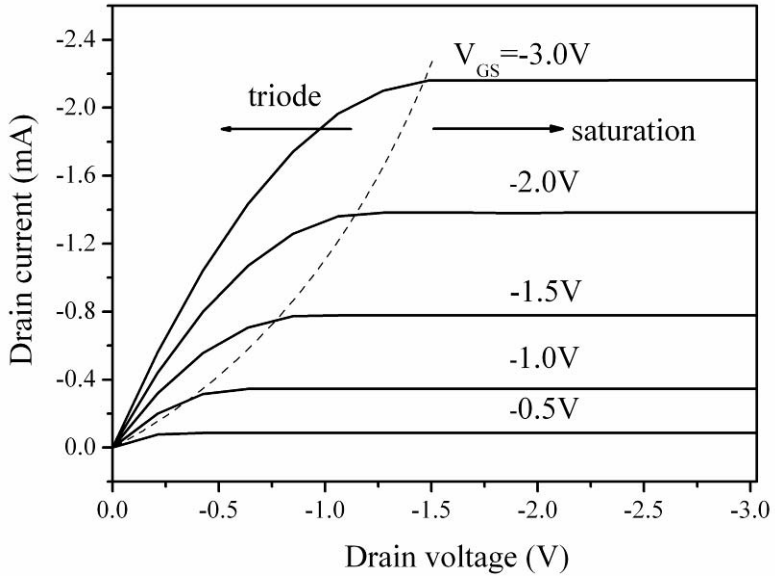

Fig 2.8 I_D-V_D characteristics of a pMOSFET. The dotted line separates the triode region of operation on the left from the saturation region on the right (2006a)

In the I_D-V_D curve (Fig 2.8), two regions of operation are formed, the triode region and the saturation region at each fixed gate voltage. When $V_{DS}<V_{DS,\,sat}$, the device is in the triode region of operation. The drain current increases linearly with increasing V_{DS}. A slight change of the drain voltage causes a significant variation of the drain current. In the saturation region, $V_{DS}>V_{DS,sat}$, the current is less dependent on V_{DS}, but is still dependent on V_{GS}, since the inversion layer density increases with V_{GS}.

Therefore, the Eqs. for I_{DS} are different in two regions:

In the linear region: $$I_{DS} = \frac{\nu C_{ox} W}{L}[(V_{GS} - V_T)V_{DS} - \frac{1}{2}V_{DS}^2] \quad (8)$$

In the saturation region: $$I_{DS} = \frac{\nu C_{ox} W}{2L}(V_{GS} - V_T)^2 \quad (9)$$

Where ν is the carrier mobility, W/L the width/length of the channel. The transconductance (g_m) shows the relationship between I_D and V_{GS}, which is given by:

In the linear region: $$g_m = \frac{W}{L}\nu C_{ox} V_{DS} \quad (10)$$

In the saturation region: $$g_m = \frac{W}{L}\nu C_{ox}(V_{GS} - V_T) \quad (11)$$

2.1.4 Ion-sensitive field-effect transistor (ISFET)

Since its introduction 30 years ago, there are about 700 papers devoted to ISFETs and 150 dealing with related devices, such as EnzymeFETs (ENFETs), ImmunoFETs (IMFET), Insulated gate FETs (IGFETs), Chemical-sensitive FETs (ChemFETs) (Inczedy et al. 1998).

The ISFET concept originates from the MOSFET structure, but differs in many aspects. In the ISFET structure, the metal gate is replaced by a reference electrode, which is exposed to aqueous electrolyte electronically contacted via a reference electrode. The readout signal of the ISFET is a relative potential difference at the gate input and the magnitude of this potential varies with the ion concentration against a corresponding reference electrode according to the Nernst equation.

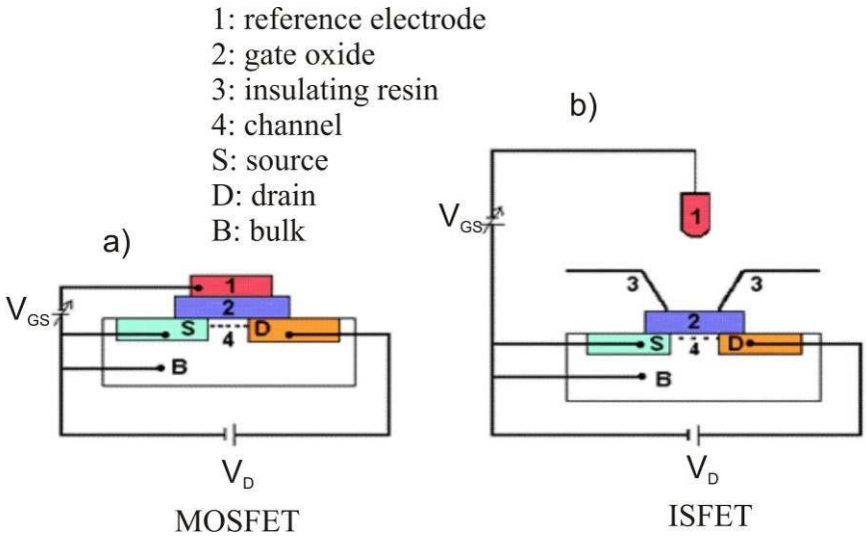

Fig 2.9 Schematic figure of a field-effect transistor MOFET (a) and an ISFET (b) (Wroblewski et al. 1996)

The equation for the flatband voltage of an ISFET is derived from that of a MOSFET (Eq. 3). For the ISFET, two additional interfaces of electrolyte/reference electrode and electrolyte/gate oxide influence the flatband voltage. The metal workfunction is replaced with the relative potential of the reference electrode to vacuum level E_{ref}, which is the main determining parameter of the interface between the electrolyte and the reference electrode. The electrolyte/gate oxide interface is determined by the surface dipole potential of the electrolyte x_{sol}, which is constant, and the variable surface potential Ψ_0. Therefore, the flatband voltage for an ISFET is given by (Bergveld 2003):

$$V_{FB} = E_{ref} - \Psi_0 + \chi_{sol} - \frac{\Phi_{Si}}{q} - \frac{Q_{SS} + Q_{ox}}{C_{ox}} \qquad (12)$$

The reference electrode potential E_{ref} is taken relative to the vacuum level, which can be calculated using the electrode potential relative to the normal hydrogen electrode (NHE) plus the value of the Fermi level relative to the vacuum state (Bousse et al. 1983). However, the absolute value of the surface potential Ψ_0 cannot be directly measured, but relative changes can be recorded in the ISFET bioassays. The surface potential is responsible for the pH sensitivity of ISFETs and controls the dissociation of the oxide surface groups.

Although the equations for the flatband voltage differ for ISFET and MOSFET, the equations of the *I-V* curves (Eqs. 8-11) for a MOSFET are also suitable for an ISFET in a first approximation.

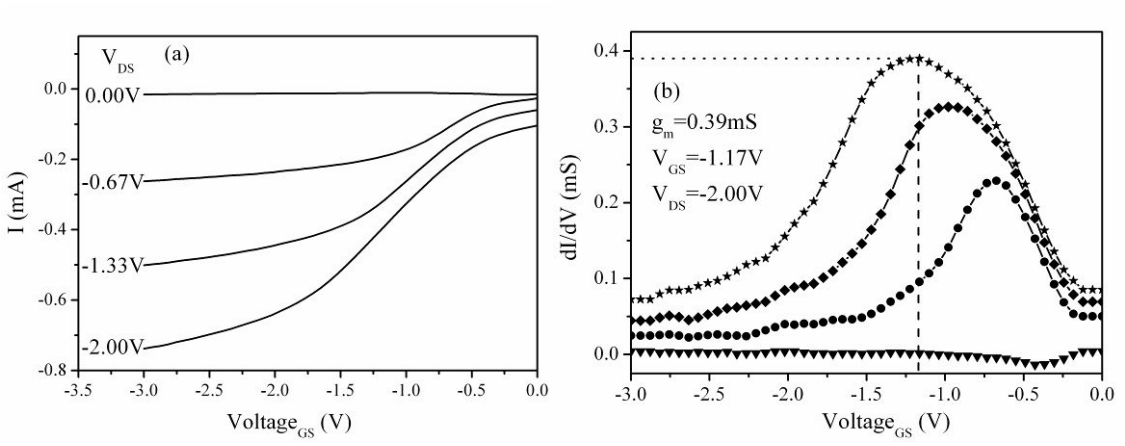

Fig 2.10 I_D-V_{GS} transfer characteristics of pISFET (a) and electrical characterization of the gate transconductance (b). Real measurement data from an ISFET used in this work are shown.

Besides the output characteristics (Fig 2.8), transfer characteristics (Fig 2.10) is important for the practical use of an ISFET. The reference voltage (V_{ref}) is applied by means of an Ag/AgCl reference electrode acting as gate voltage (V_G). The typical operation point of an ISFET is in the saturation region ($V_D > V_{D,sat}$, $V_{D,sat}=V_{FB}-V_{ref}$), where the inversion channel becomes shorter than the channel length. With increasing reference voltage, the drain current increases correspondingly. In this thesis, each ISFET biosensor was electronically characterized before each experiment. A working point was set, which was defined by applying a constant drain-source voltage (V_{DS}) and a constant gate-source voltage (V_{GS}). The highest sensitivity regime of the ISFET biosensors was extracted for the electronic detection measurements at the maximum transconductance g_m:

$$g_m = \frac{\partial I_{DS}}{\partial V_{GS}}\Big|_{V_{DS}=const} \tag{13}$$

The pH sensitivity of the ISFET devices used in this work was 34±2mV/pH compared to the literature value of 30-40 mV/pH (Bataillard et al. 1987; Bergveld et al. 1997; Fung et al. 1986). The pH sensitivity as well as the sensitivity to potassium and sodium concentration changes was intensively studied in related works of our group (Borstlap 2006; Sakkari 2005).

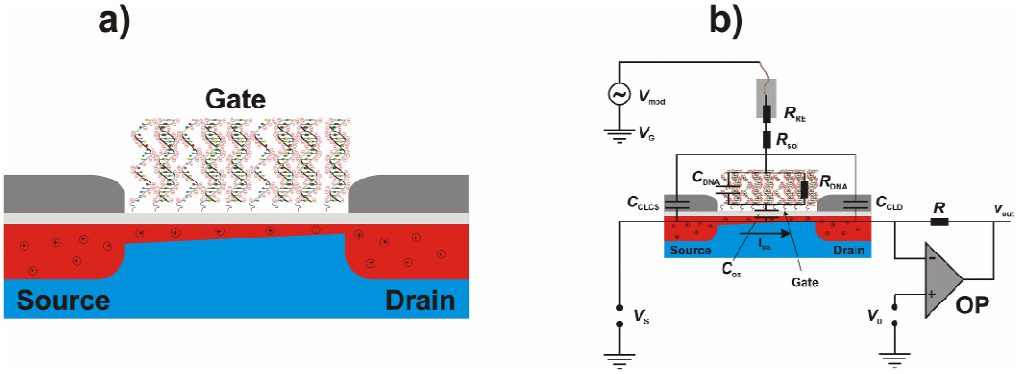

Fig 2.11 Schematic drawing for the label-free DNA detection using a FET

The ISFET setup used in this work for the detection of biological reactions is shown in Fig 2.11. The (bio)molecular layers at the gate structure influence the surface potential, which can be monitored by the shift of the gate voltage in a potentiometric way. The ISFET as a potentiometric biosensor records the reactions by a direct current (DC) readout system. The biomolecular layer might also form additional impedance on top of the gate structure, which can be monitored by an alternating current (AC) readout of the transistor transfer function. The ISFET detection principles in both modes and the amplifier equivalent circuit will be discussed in paragraph 3.3.

2.2 SiO_2/electrolyte interface

The chemical sensitivity and selectivity of an ISFET completely depend on the properties of the electrolyte/insulator interface. When silanols come into contact with an electrolyte solution, pH-dependent electrochemical equilibrium is established. The hydroxyl groups at the gate oxide surface can be protonated and deprotonated and thus, when the gate oxide contacts an aqueous solution, a change of pH will change the SiO_2 surface potential. The point of zero charge is 2-2.5 for the SiO_2 surface (Bousse 1982), at which pH value the surface is neutral. In lower pH, the net surface charge is positive, for higher pH negative. Theoretically, the site-binding model (Yates et al. 1974) applies to thermal oxidized silicon as shown in Eqs. 14-15.

$$\equiv SiO^- + H^+ \Leftrightarrow \equiv SiOH \tag{14}$$

$$\equiv SiOH + H^+ \Leftrightarrow \equiv SiOH_2^+ \tag{15}$$

In reality, different kinds of silanols exist, some silanol groups are hydrogen bonded to neighboring silanols, while other silanols are only hydrogen bonded to water molecules. Different schemes of hydrogen bonding are believed to have a considerable impact on the reactivity of these groups. However, the total number of surface functional groups, the distribution of different types of groups and the reactivity of different groups are still not clear.

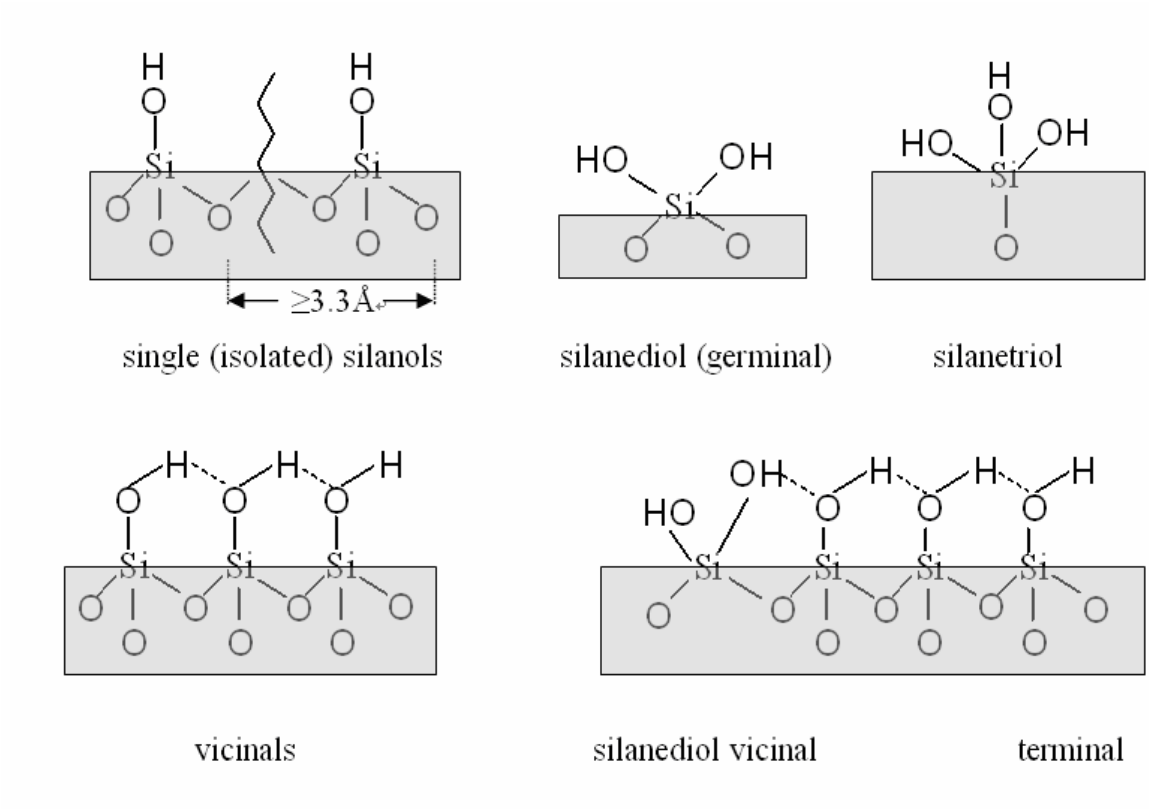

Fig 2.12 Different types of silanol groups (Bergna 1990)

Since only the free hydrogen can respond to the surface potential change, silanols in three configurations: single silanols, silanediol, and silanetriol are affected. In the site-binding model, the signal transduction is describd as a function of the state of ionization of the surface SiOH groups.

2.2.1 Electrical double layer at the solid-liquid interface

At the SiO_2/electrolyte interface, the surface charge σ_0 is balanced by an equal but opposite charge, σ_{dl} in the electrolyte to neutralize the surface. The charge density σ_{dl} defines the so-called double layer and the two opposite charges, σ_0 and σ_{dl}, parallel to each other form the integral double-layer capacitance $C_{dl,i}$. The charges are not uniformly distributed

throughout the liquid phase, however concentrated near the charged surface. Thus, a small but finite volume of the liquid phase is different from the extended bulk solution.

There are three theoretical treatments of the double layer on the interface, Helmholtz Plane Theory, Gouy-Chapman Theory and Gouy-Chapman Stern Models.

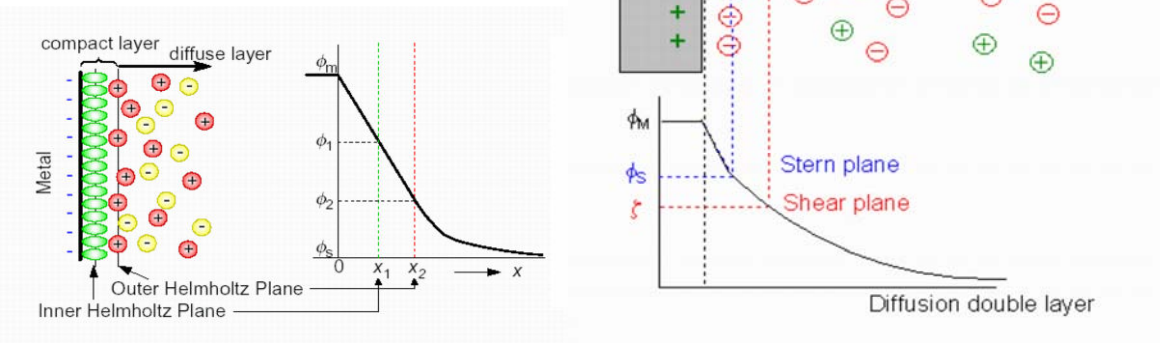

Fig 2.13 Theory models of the solid/liquid interface, Helmholz double layer (left) and Gouy-Chapman Models (right)

The Helmholtz Double Layer theory (1879) is a simple approximation in which the surface charge is neutralized by counterions of opposite sign. The surface potential is linearly dissipated from the surface, and counter charged, opposite polarity ions resides at the surface by a distance of their radius. The charge in the solution is essentially 2-dimensional and located at the outer Helmholtz Plane (OHP). The surface is treated as parallel plate capacitor following $C=\varepsilon_0\varepsilon_r A/d$, ($\varepsilon_0$ dielectric constant of the vacuum, ε_r relative dielectric constant of the medium between the plates, A denotes the surface area of the plates, and d is the distance of the plates). However, the Helmholtz model does not adequately explain all the features, since it hypothesizes rigid layers of opposite charges. This does not occur in nature.

The Gouy-Chapman double layer (diffuse double layer) theory (1910-1913) introduces an additional diffuse double layer to the Helmholtz Model in which counter ions are not rigidly held, but tend to diffuse into the liquid phase until a counter potential restricts this tendency. The diffuse charges in the Gouy-Chapman Model are assumed neither a layer of hydrated ions stuck at the OHP nor a linear voltage drop across the dielectric layer. The ion

distribution in the charged surface region is determined by temperature and the energy to bring the ion away to an infinite distance. The ion concentration distribution in the diffusion layer is given by a Boltzmann equation:

$$n_i = n_i^0 \exp(-\frac{ze\psi_i}{k_B T}) \tag{16}$$

With n_i^0 the number of ions of type *i* per unit volume of bulk solution and *z* valence of ion i. The term $ze\psi_i$ in the numerator of the exponent is the energy to bring an ion from an infinite distance to a point where the potential is ψ_i, and k_B Boltzmann constant and *T* the absolute temperature. Combining the Boltzmann distribution with the Poisson equation and integrating with appropriate limits, the description of the electric potential as a function of distance from the surface is given:

$$\lambda_{dl} = \sqrt{\frac{\varepsilon_0 \varepsilon_r KT}{2n_0^i z^2 q^2}} \tag{17}$$

The Debye length is the reciprocal of the Debye-Hückel parameter. The thickness of the double layer decreases with increasing valence and concentration of ions. The electric potential is a function of the distance from the surface. The thickness of the diffuse double layer decreases with increasing ion valence and concentration of the buffer electrolyte. The charge in the diffuse layer is given by the Grahame equation:

$$\sigma_{dl} = \sqrt{8\varepsilon_0 \varepsilon_r kTn_0} \sinh\left(\frac{ze\Psi_0}{2kT}\right) \tag{18}$$

Therefore, the diffusion capacitance is derived from

$$C_{dif} = \frac{d\sigma_{dl}}{d\psi_0} = \sqrt{8\varepsilon_0 \varepsilon_r kTn_0} \cosh\left(\frac{ze\psi_0}{2kT}\right) \tag{19}$$

Experimentally, the double layer thickness is generally found to be somewhat larger than calculated, owing to the assumption that activity equals molar concentration when using the desired form of the Boltzman distribution. In fact, not only the oppositely charged ions diffuse into the bulk solution, the same sign as the surface charge will also be found within the double layer.

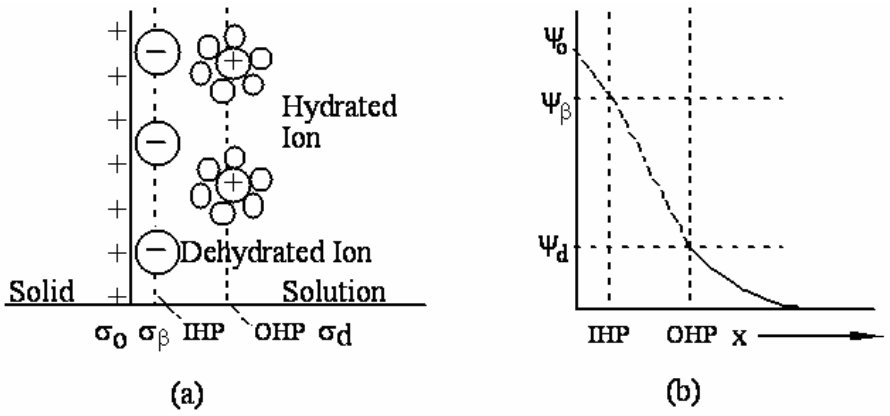

Fig 2.14 Gouy-Chapman Stern Theory of the solid/liquid interface

The Stern Mode of the diffuse double layer has been developed, combining the Helmholtz and the Gouy-Chapman Model. It assumes a "plane of closest approach", which is based on the fact that ions have finite size, so they cannot approach the surface closer than a few nm. Besides the diffusion layer in the Gouy-Chapman Model, a Stern layer is formed and subdivided into two regions of inner and outer Helmholtz plane (IHP and OHP). The IHP is defined by the plane of the center of the dehydrated ions. The excess ions are adsorbed to form the OHP. This layer is located at the distance X_H, at the center of the hydrated ions in the solution. The diffuse layer, starting from X_H, contains the same amount of charge (of opposite sign) as the oxide surface charge. The potential between the electrolyte and the surface consists of two parts, a potential drop across the diffuse layer and across the charge-free layer (Stern Layer). The difference between the potential in the diffusion layer and the surface potential is the potential difference across the Stern capacitance. Consequently, the double layer capacitance consists of a series network of a Helmholtz-layer capacitance (the Stern capacitance) and a diffuse-layer capacitance.

$$\frac{1}{C_{dl}} = \frac{1}{C_{Stern}} + \frac{1}{C_{dif}} = \frac{X_H}{\varepsilon_0 \varepsilon_r} + \frac{1}{\sqrt{8\varepsilon_0 \varepsilon_r kTn_0}\cosh\left(\frac{ze\psi_0}{2kT}\right)} \tag{20}$$

2.2.2 pH sensitivity of ISFETs

When the SiO_2/electrolyte interface is protonated or deprotonated, the equilibrium is established (Eq. 14, 15), and the dimensionless intrinsic dissociation constants (K_a, K_b) are

$$\frac{C_{SiO^-} \cdot a_{H_S^+}}{C_{SiOH}} = K_a \quad \text{and} \quad \frac{C_{SiOH} \cdot a_{H_S^+}}{C_{SiOH_2^+}} = K_b \tag{21}$$

with C the concentration for the ions. H_s^+ donates the activity of the protons in the vicinity of the oxide surface. $a_{H_S^+}$ is the activity of protons at the surface.

On the oxide surface, there is a fixed number of surface sites per unit area present, N_s:

$$N_S = C_{SiOH} + C_{SiO^-} + C_{SiOH_2^+} \tag{22}$$

Depending on the chemical equilibrium of the surface sites, a surface charge density σ_0 [C/m^2] exists:

$$\sigma_0 = q(C_{SiOH_2^+} - C_{SiO^-}) = -qB \tag{23}$$

Where B is the number of negatively charged groups minus the number of positively charged groups in moles per unit area. So, the relation between the activity of the protons at the oxide surface $a_{H_S^+}$ and the surface charge density σ_0 in terms of the total number of available sites N_s and the intrinsic dissociation constants K_a and K_b is given by:

$$\sigma_0 = qN_S\left(\frac{a_{H_S^+}^2 - K_aK_b}{K_aK_b + K_b a_{H_S^+} + a_{H_S^+}^2}\right) \tag{24}$$

The effect of the surface protons activity $a_{H_S^+}$ on the surface charge density σ_0 can be found from Eq. 24:

$$\frac{\partial \sigma_0}{\partial pH_S} = -q\frac{\partial B}{\partial pH_S} = -q\beta_{\text{int}} \tag{25}$$

The change in $a_{H_S^+}$ is expressed by its corresponding surface pH value (pH_S). The change of pH results in the change of σ_0 and a change in the net number B of the basic groups. By definition, $\partial B / \partial pH_S$ represents the buffer capacity β_{int} of the oxide surface. Combining with the Eq. 19, the effect of a small change in the surface pH (pH_s) on the change in the surface potential ψ_0 is described by:

$$\frac{\partial \psi_0}{\partial pH_S} = \frac{\partial \psi_0}{\partial \sigma_0} \cdot \frac{\partial \sigma_0}{\partial pH_S} = \frac{-q\beta_{\text{int}}}{C_{dif}} \tag{26}$$

Expressed with the Boltzmann equation:

$$a_{H_S^+} = a_{H_B^+} \cdot \exp(-q\psi_0 / kT) \quad \text{or} \quad (pH_S - pH_B) = q\psi_0 / kT \tag{27}$$

results in the general expression for the pH sensitivity of an ISFET:

$$\frac{\partial \psi_0}{\partial pH_B} = -2.3\frac{kT}{q} \cdot \alpha \quad \text{with} \quad \alpha = \frac{1}{\frac{2.3kTC_{dif}}{q^2\beta_{\text{int}}} + 1} \tag{28}$$

The parameter α is a dimensionless sensitivity parameter that varies between 0 and 1, which depends on the oxide surface intrinsic buffer capacity β_{int} and the differential double-layer capacitance C_{dif}. If α=1, the ISFET has a so-called Nernstian sensitivity of 59.2mV/pH at 298K, which is also the maximum achievable pH sensitivity.

It appears that the usual SiO_2 from the MOSFET process does not fulfill the requirements of a high value of β_{int}. The pH sensitivity is only about 30mV/dec depending also on the electrolyte concentration via C_{dif} and on the cleaning status of the SiO_2 surface. A freshly cleaned SiO_2 surface can have a higher α value, which is reduced when contaminations are present at the surface. Other layers have been introduced to ISFET fabrication such as Si_3N_4, Al_2O_3 and Ta_2O_5 with increased values of β_{int}. The intrinsic buffer capacity of Ta_2O_5 is even so high that the value of C_{dif} becomes less important, which is independent of the electrolyte concentration, while a pH sensitivity of 58mV/dec can be achieved over a pH range from 1 to 12 (Bergveld 2003).

2.2.3 Attachment of biomolecules to the gate surface of ISFETs

When biomolecules attach the SiO_2/electrolyte interface, an ion-permable layer is formed between the surface and the electrolyte. The accumulation of the DNA negative charges at the gate oxide surface can generate a change of the surface potential according to the Grahame equation (Eq. 18) (Israelachvili et al. 1999). The maximum surface charge density σ_0 of silicon oxide is 0.8 C/m^2 (Dong et al. 1998). The gate potential can be derived by:

$$\Delta\Psi_{Gate} = \frac{2kT}{ze}\left(ar\sinh\left(\frac{\sigma_0 + \sigma_{DNA}}{\sqrt{8\varepsilon_{elect+DNA}\varepsilon_0 kTn_{0+DNA}}} \right) - ar\sinh\left(\frac{\sigma_0}{\sqrt{8\varepsilon_{elect}\varepsilon_0 kTn_0}} \right) \right) \quad (29)$$

It is has been reported that the surface potential change caused by immobilization of 20 bases ssDNA ($4\times10^{15}/m^2$) in a low ionic strength electrolyte (eg. 6mM) results in potential changes of about 3 mV (Fritz et al. 2002; Han et al. 2006c; Han et al. 2006b; Uslu et al. 2004).

Concerning the detection of the attachment of DNA onto the gate surface, two basic effects are usually considered, the capacitance effect and the charge effect (Landheer et al. 2005; Poghossian et al. 2005). The capacitance and related impedance effect will be discussed in the next paragraph. Firstly, the charge effect is described. Three parameters influence the surface potential, when biomolecules attach the solid/liquid interfaces: a distribution in the double layer, conformation related dipole moment of the biomolecules and the Donnan potential.

When the DNA molecules attach the gate surface by non-covalent binding, they lie flatly on the surface. In this case, higher DNA-DNA hybridization signal compared to the covalent immobilization assay is expected (Chapter IV). The charge density change within the order of the Debye length can be detected, which increases with decreasing valence and concentration of ions in the electrolyte (Eq. 17). Therefore, a low ionic strength buffer electrolyte is a prerequisite to enable the detections (Poghossian et al. 2005).

With the change of biomolecule conformation, a ionic redistribution effect near the ISFET sensor surface can be occurring. The DNA molecules are modelled as an ion-permeable circular cylinder with a diameter of 1.5-2 nm. The space between the cylinder-like biomolecules is full of small counter ions. When the hybridization reaction occurs on the sensor surface, the intermolecular spaces are reduced, which results in a depletion of counterions at the solid/liquid interface.

Apart from the surface potential, the Donnan potential originates from fixed charges inside a molecular layer, the Donnan potential is the potential in the bulk of a sufficiently thick membrane, where charge neutrality prevails (Landheer et al. 2005; Ohshima et al. 1988). A charge in an attached molecular layer might vary the Donnan potential, which add finally to the recorded surface potential charge.

potential drop between the centres of the closest hydrated ions in the membrane and the insulator, according to (Landheer et al. 2005):

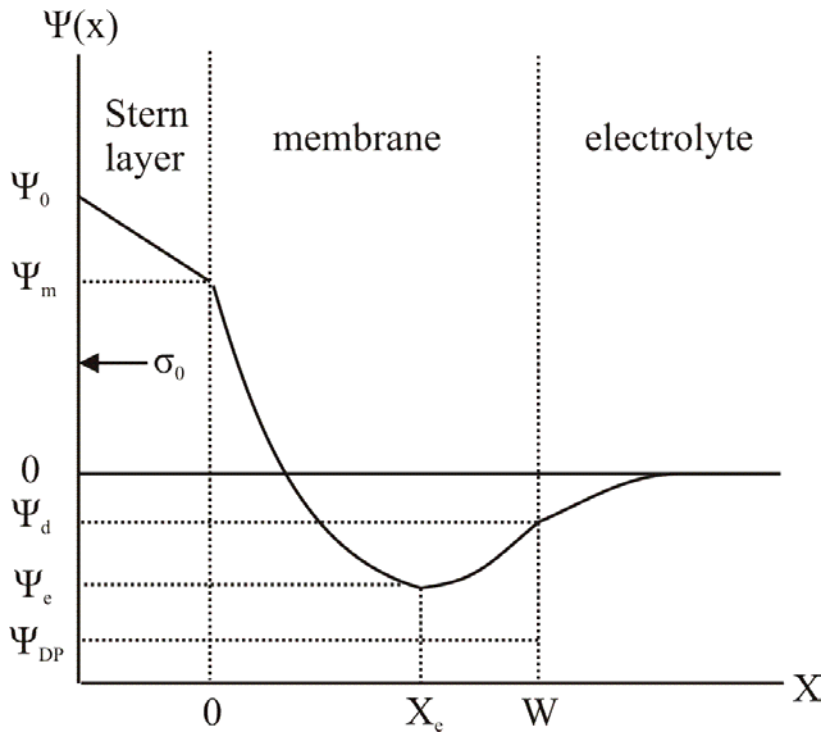

Fig 2.15 Details for the potential distribution from the insulator surface through the Stern layer and the biomembrane into the electrolyte. The figure was adapted from (Landheer et al. 2005)

Ψ_0, Ψ_m, Ψ_d, Ψ_e, Ψ_{DP} are potentials for surface, membrane, double layer, electrolyte and Donnan potential, respectively. The X-axis is the perpendicular distance away from the surface, and $X=0$ and $X=W$ are located at the OHP and the membrane. In the range of $X>W$, the potential gradient and charge in an electrolyte can be described with Eq. 18. When $0<X<W$, the Donnan potential must be considered for the total surface potential.

2.3 Transistor transfer function

Most ISFETs use a direct current (DC) readout system. They are potentiometric biosensors detecting biomolecular reactions through their ion-selective solid-liquid interface or an artificial molecular membrane, which is attached to the gate of an ISFET device. The label-free detection of DNA is based on its intrinsic charge causing potential change at the solid-liquid interface (Barbaro et al. 2006; Kim et al. 2004c; Pouthas et al. 2004a; Pouthas et al. 2004b; Sakata et al. 2005b; Souteyrand et al. 1997; Tsuruta et al. 1994). Generally, effects like drift, temperature, electrolyte composition, pH of the buffer solution and the

type of the reference electrode influence the measurements. During this thesis, the ISFET detection in AC mode for the attachment of PEMs and DNA on the optimized surfaces was established in our group. The attachment of biomolecules to the gate surface alters the capacitance and resistance properties of the interface. Impedance measurements can detect these changes. ISFETs as impedimetric biosensors with AC readout allow the sensing of the biomolecular attachment and membrane properties change at a very small lateral resolution (Antonisse et al. 2000; Bataillard et al. 1987; Demoz et al. 1995; Diot et al. 1985; Katz et al. 2003; Kharitonov et al. 2000; Kharitonov et al. 2001; Kruise et al. 1992; Lahav et al. 2001; Lugtenberg et al. 1998; Pogorelova et al. 2002; Pogorelova et al. 2004; Sallacan et al. 2002; Souteyrand et al. 1994; Souteyrand et al. 1997; Zayats et al. 2002b).

A first electrical and mathematical description of the ISFET transfer function was provided (Bergveld et al. 1989; Schasfoort et al. 1989). In general, the ISFETs AC readout systems are described by an electrical equivalent circuit. Usually an electrical equivalent circuit consists of three types of basic elements resistor, inductor and capacitor of which all are a function of the frequency. Table 2.2 shows the basic equations for resistor, capacitor and inductor as the function of voltage and current as well as their impedance.

Table 2.2 Common electrical elements in the AC equivalent circuit of an impedimetric biosensor

Components	**Current vs. Voltage**	**Impedance**
Resistor	V=IR	Z=R
Capacitor	I=CdV/dt	Z=1/jωC
Inductor	V=LdI/dt	Z=jωL

For the impedance measurements with ISFET in this thesis, the inductor can be neglected because in the frequency range of 1Hz-100 kHz, the inductance (L) of our system is too low to contribute to the impedance. The resistor follows Ohm's law ($R = \frac{V}{I}$, V voltage, I current) at all current and voltage levels, and it is independent of frequency. The complete AC equivalent circuit of an ISFET with attached biomembrane is shown in Fig 2.16.

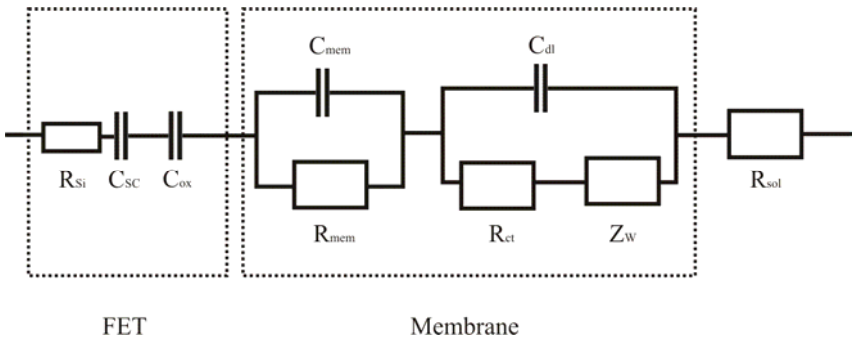

Fig 2.16 Complete equivalent circuit of a membrane-gate modified ISFET (Armstrong et al. 1990). The figure was adapted from (Kharitonov et al. 2001).

When biomembrane attaches the gate surface, the complete equivalent circuit is composed of three parts, FET input, membrane element and resistor of the solution (R_{sol}), which is connected in series.

The FET input consists of the silicon-electrode resistance (R_{si}), the space-charge capacitance (C_{sc}) and the oxide-insulator capacitance (C_{ox}). The membrane element has two major parts, a membrane and a double layer. The membrane can be described by its bulk capacitance (C_{mem}), in parallel with its bulk resistance (R_{mem}). The double layer part of the membrane element includes the double-layer capacitance at the membrane interface (C_{dl}), the charge-transfer resistance at the membrane interface (R_{ct}), and the input of the Warburg impedance Z_w originating from the diffusion of ions to the membrane interface (Katz et al. 2003).

For the ISFETs used in this work, an additional component needed to be considered. When there are no biomolecules attach to the FET surface, the two dominant components in the equivalent circuit are the contact lane capacitance (C_{CL}) and the solution resistance (R_{sol}) because of the large contact lane areas of our ISFET. The impedance of the reference electrode can be neglected in most cases, as it is smaller than the solution resistance in our experiment. The overall time constant (τ) of the systems is then:

$$\tau = 1/f = C_{CL} \cdot R_{sol} \qquad (30)$$

Typical values for the recordings presented in this work were 1nF for C_{CL} for the 8-channel chips, 100 pF for the 16-channle chips and 50-400 kΩ for R_{sol}. Therefore, the typical cut-off frequencies of our ISFET devices were in the range of 2.5-20 kHz for the 8-channel chips and 20-200 kHz for the 16-channel chips, respectively.

The equivalent gate input circuit can be characterized by the transfer function. The transfer function is the mathematical representation of the relation between the input and the output signals of a frequency-dependent system. A superimposed sine wave voltage of variable frequency δV_{GS} is leading to a drain current variation δI_d. Therefore, the transconductance g_m is frequency-dependent $g_m = \delta I_d / \delta V_{GS}$ (Bergveld et al. 1989). The voltage related to I_d, V_{GS} and g_m is given by:

$$V_{out} = -RI_d = -Rg_m V_{GS} \tag{31}$$

R is the electrical feedback resistance of the first amplifier stage. The voltage applied to the gate partly drops over the oxide and partly over the membrane layers, thus the effective potential difference between gate and source is smaller than the applied voltage. Therefore, the transfer function $H(j\omega)$ is introduced as a multiplication factor of V_{GS}.

$$H(j\varpi) = \frac{1 + j\varpi R_{mem} C_{mem}}{1 + j\varpi R_{mem}(C_{meme} + C_{ox})} \tag{32}$$

So, $$g_m = -\frac{V_{out}}{RH(j\varpi)V_{gs}} \tag{33}$$

g_m becomes frequency dependent. A theoretical plot of the transfer function versus the frequency is shown in Fig 2.17. Two time constants τ_1, τ_2 can be graphically determined out of the graph. They are given as the intersection of the linear segments in the high and low frequency ranges (Kharitonov et al. 2001; Zayats et al. 2002b).

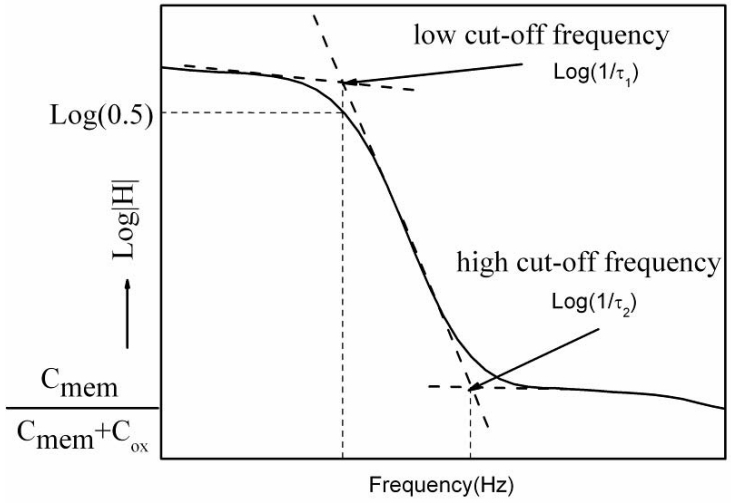

Fig 2.17 Theoretical transfer function and graphical extraction of the time constants. The figure was adapted from (Antonisse et al. 2000)

The time constants τ_1 and τ_2 are extracted as

$$\tau_1 = R_{mem}(C_{mem} + C_{ox}) \approx R_{mem}C_{ox} \tag{34}$$

$$\tau_2 = R_{mem}C_{mem} \tag{35}$$

At the low cut-off frequency, the oxide layer capacitance is bigger than that of the membrane. Consequently, the term C_{mem} can be consequently neglected. On the other hand, the high cut-off frequency is dominated by the membrane capacitance and membrane resistance, which is related to the attached biomolecules.

Chapter III Materials and Methods

In this chapter, the properties of polyelectrolyte (PE) and biomolecules related to the surface modification protocol and to the ISFET detections are elaborated. Several characterization methods used to analyze the surface condition after each modification step are described.

3.1 Properties of polyelectrolytes & biomolecules

PEs can be utilized as a model for the biomolecules assays since their similar influence to the ISFET signal. Possible effects during ISFET detection might be originated from the PE conformation and charge distribution. For the bioassays presented in this thesis, three biomolecues are involved in the detection including DNA, biotin and streptavidin. Their correlative properties are also described in this chapter.

3.1.1 Polyelectrolyte properties

To date it is well accepted that for the ISFET detection, the charge distributions of PE are mainly responsible for the recorded signal changes. However, the charges properties of PEs are mainly related to their conformation.

3.1.1.1 Conformation of polyelectrolytes in solution

Polyelectrolytes (PEs) are electrolytes of high molecular weight, and they are composed of repeating units and ionizable groups (Barrat et al. 1996; Forster et al. 1995; Oosawa 2001; Radeva 2001; Schmitz 1993; Tanford 1961). These groups dissociate in polar solvents such as water leading to a charge of the PE molecules. PE possesses properties of both electrolyte and polymer, acting as conductor like salt, having a viscosity similar to polymer.

The properties of PEs in solutions and at charged surfaces depend on many parameters such as the fraction of dissociated ionic groups, the solubility in the buffer electrolyte, solution dielectric constant, salt concentration and polymer-substrate interactions (Dobrynin et al. 2005). Commonly used PE can be “weak” or “strong” depending on the dissociating ability in the solvent. Strong PEs dissolves completely for most reasonable pH values, while weak PEs dissociate just partly.

Two types of interactions play the crucial role on the conformation of the PE in different solutions, inter- and intrachain interactions. Interchain interactions refer to repulsive electrostatic interactions, which are mainly controlled by coulomb forces. Intrachain interactions originate from the non-electrostatic attractive interactions of backbones, which are insoluble in solvent and easy to attract by the Van der Waals forces, hydrogen bonding or hydrophobic effects. Flory theory, scaling model (Kuhn et al. 1948) and Debye Hückel theories are utilized to explain and to simulate the PE chain conformation in solutions.

The semiflexible chain model elucidates in approximately “ideal” solutions that the end-to-end distance of PE increases linearly with the chain length (Barrat et al. 1996). The coulomb repulsion is excluded, and the PE is modeled like a non-charged PE. The PE chains in this condition expand randomly to reach the lowest energy, in rigidly rod conformation (Fig 3.1a).

In good solvent such as water, the PE chains repulse each other due to the charge on the chain. The intrachain interaction dominates over the interchain one, which cause the PE to expand more rigidly (Fig 3.1b). In finite concentration of counterions solutions such as salt solutions, the PE chain coils. With the increase of the counterions concentration, the PE chain condenses and collapses.

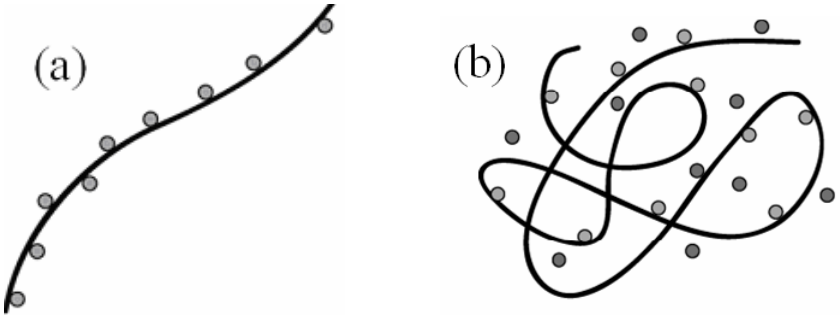

Fig 3.1 Charged PE chains (a) stretched in solutions without counterions (b) can be assumed as a more random-walk-like conformation in the solution present of counterions.

When the PE is diluted in poor solvents, its backbone is insoluble in the solvent and the backbone monomers strongly interact through non-electrostatic attractive interactions owing to Van der Waals forces, hydrogen bonding or any hydrophobic effect (Holm et al. 2004). Intra- and interactions compete each other and dominate in short-distance and long-distance, respectively. Although the PE stretches in the macrostructure, in the fine region, it collapses to a pearl-necklace conformation, and even to a globular conformation (Fig 3.2).

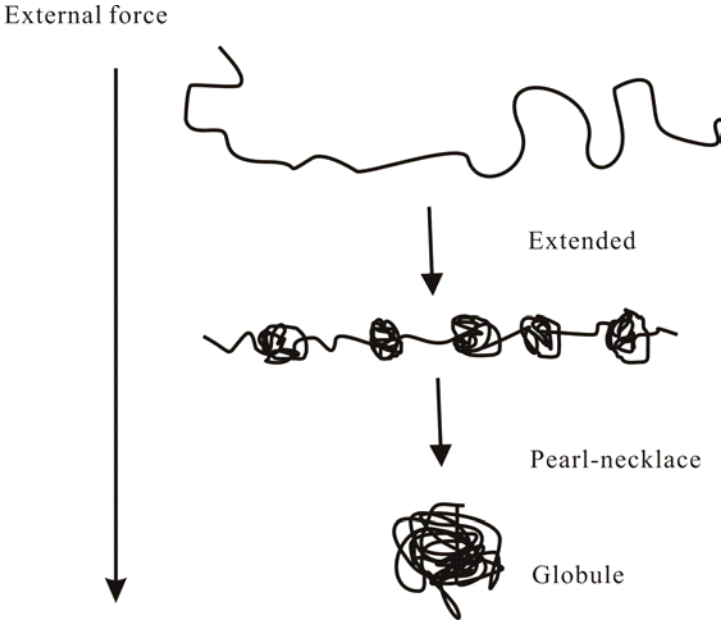

Fig 3.2 Increasing external force or decreasing of solubility of the solvent, the conformation of the PE changes from elongated via a pear-necklace to a globular structure (Chodanowski et al. 1999; Dautzenberg 1994; Dobrynin et al. 1996; Micka et al. 1999)

When solutions of two oppositely charged polymers (that is, a solution of polycation and of polyanion) are mixed, a bulk complex (precipitate) is usually formed. This occurs because the oppositely charged polymers attract each other and bind together irreversibly.

3.1.1.2 Buildup of polyelectrolyte multilayers (PEMs) by layer-by-layer adsorption

Polyelectrolyte multilayers (PEMs) can be formed by alternating adsorption of polyanions and polycations in solutions. This method is the so-called layer-by-layer (LBL) self-assembly method (Decher et al. 1992). LBL methods are not limited to the polyelectrolyte mulilayer buildup, but can also be extended to a variety of charged material, such as nanoparticles, proteins, DNA, dyes, etc. (Bertrand et al. 2000; Decher 1997; Decher et al. 2003; Hammond 1999).

The first PE layer adsorbs on the oppositely charged surface, which is either a soft or a hard surface. A hard surface can be a solid support (Caruso et al. 1997), while a soft surface can be a precoated solid support. On the hard surface, the adsorption depends much on the surface charge density and ionic strength of the buffer electrolyte. In a high ionic strength solution, loops and tails of the PE increase the thickness of the layers and cause strong charge overcompensation. After the first layer, the following adsorptions of PE can be regarded as adsorption on a soft surface.

The adsorption on soft surfaces is controlled by both the charges carried by the PE layer from the solution in its 3-D structure and the flexible underlying layer. For strong PEs, one third of the charges mingle with the previous layer. The remaining 2/3 are compensated by counterions and released with the following adsorption. The strong PE has an exact stoichiometry for the distribution of charges, which is only affected by the ionic strength of the electrolyte solutions.

For the weak PE the layer thickness and surface coverage depends on the pH due to pH-dependent swelling (Kolarik et al. 1999). With the variation of pH and ionic strength, the repulsion between the chains (intra interactions), chain stiffness and surface coverage change accordingly.

During the formation of PEMs from the PE in a solvent, the conformations of PE change from 3-dimensional (3D) in solution to 2-dimensional (2D) by flattening out, and reverse

to a 3D structure when the following PE layer is adsorbed on it. In low ionic strength, the variable thickness related to the density of PEMs strongly depends on the concentration of salt, and the thickness increases linearly with the addition of salt. However, in the high salt concentration, the influence of concentration on the thickness is observed in both increasing (Steitz et al. 2000) and decreasing directions (Losche et al. 1998).

After the adsorption of the first few layers, the following buildup of PEMs is independent of the original surface. During the buildup of PEMs, the change of external condition still affects the internal structure in terms of pH, hydration condition, etc...

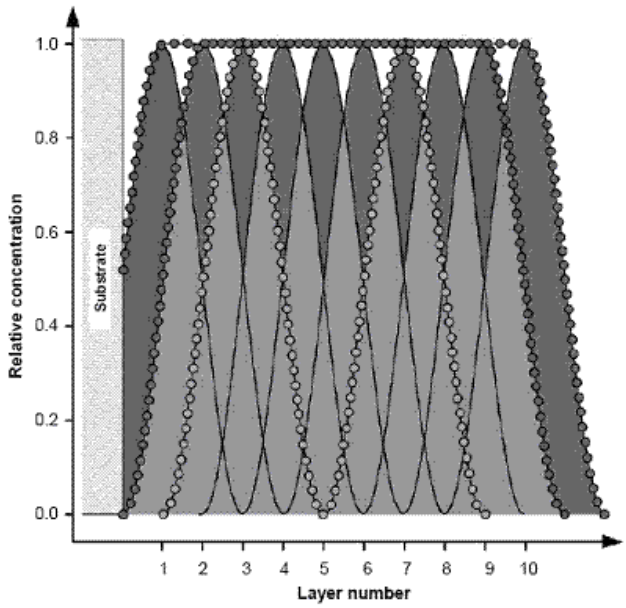

Fig 3.3 Schematics of the concentration of a PEM containing 10 layers on an initially positively charged substrate. The five dark grey layers and five shallow grey layers represent polyanion and polycation layers, respectively (Decher 1997).

The outer layer defines the properties of the total PEM after the buildup. Differently charged PEs show different characteristics according to the internal water content and the pH of the buffer solution. Even under dry conditions, the PEMs contain 10-20% water, which facilities hydration and increases the internal interaction. The strong complex PE pairs have a smaller swelling ratio than the weak complex PE ones due to the surface energy of the outer layer. Furthermore, the swelling ability increase with an increase in the concentration of salt during the assembly process (Anderson et al. 1995; Dubas et al. 2001; Sukhorukov et al. 1996).

3.1.2 DNA structure and charge

Deoxyribonucleic acid (DNA) is comparable to a charged linear PE because the DNA main chain is composed of negatively charged phosphate groups at neutral pH of the buffer electrolyte. DNA has some common properties with PE, but also some specific differences.

3.1.2.1 Structure of the DNA double helix

DNA is a polymer of nucleotides organized in a double helix (Watson et al. 1953). It contains the genetic instructions specifying the biological processes of all cellular forms of life, and some viruses.

The monomer units of DNA are nucleotides, and the polymer is known as a "polynucleotide". Each nucleotide consists of a 5-carbon sugar (deoxyribose), a nitrogen-containing base attached to the sugar, and a phosphate group. There are four different types of nucleotides found in DNA, differing only in the nitrogenous base. The four nucleotides are given one-letter abbreviations as shorthand for the four bases: adenine (A), thymine (T), cytosine (C) and guanine (G).

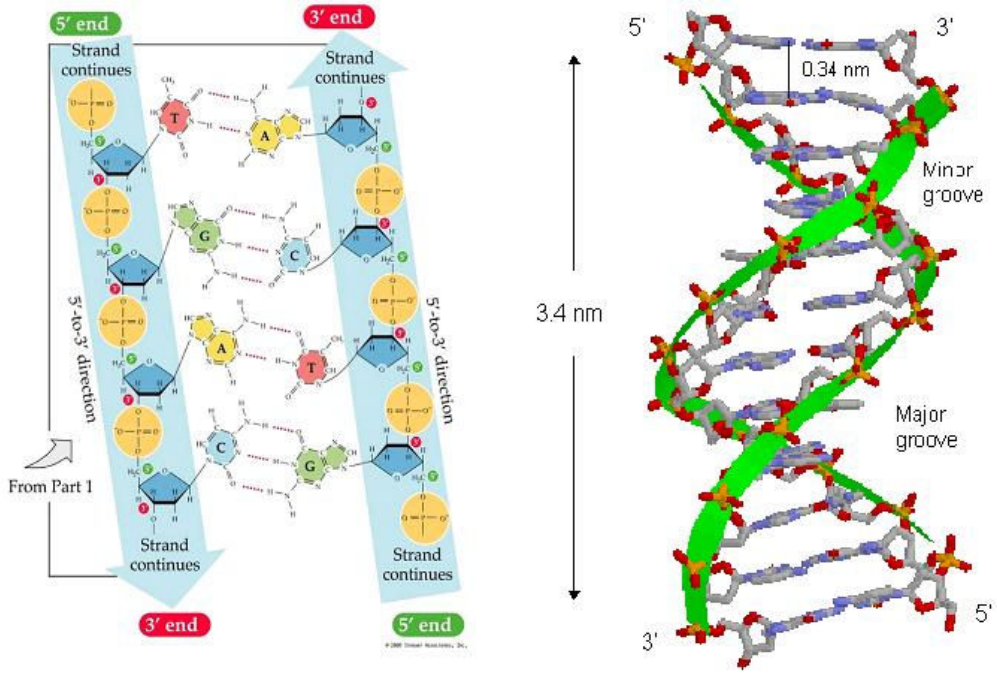

Fig 3.4 Structure of a DNA double helix (Purves 2004)

A and G are the purine bases, C and G are the pyrimidine bases. Purines consist of a six-member and a five-member nitrogen-containing ring, fused together, and pyrimidines have only a six-member nitrogen-containing ring. The process of forming a double helix from two single stranded (ss) DNA molecules is called hybridization and is achieved by complementary paring of two base pairs (bp) via hydrogen bonds (Fig 3.4). The energy of two bp is different due to the number of hydrogen bonds connecting the two base pairs. A to T are connected via two hydrogen bonds and G to C via three hydrogen bonds. Since pyrimidines and purines are not diametrically opposite, two unequal grooves come into being. Major grooves are deeper and wider than minor grooves (Fig 3.4). The different position and the energy of the two grooves offer different recognition sites and functions for DNA-binding proteins. Each strand of the double helix has a certain orientation, for reasons of chemical nomenclature one strand is called 3′ and the other 5′.

3.1.2.2 Thermal stability of the DNA duplex

The parameters influencing the conformation of PEs are also valid for the DNA sequence, as both macromolecules consist of repeated units. PE has unique units, and DNA has four different units (nucleotides). The hybridization process of DNA-DNA polynucleotides is stoichiometric and strongly affected by the pH value and ionic strength of the solution. In addition, this process involves the formation of hydrogen bonds. Parameters like probe length, DNA concentration and especially the order of nucleotide sequence also affect the association.

Addition of salt, which adsorbs to the phosphate backbone, decreases the electrostatic repulsion of the two ssDNA. Hence, the higher the salt concentration is, the more stable the double helix is. On the other hand, a low salt concentration lowers the reaction rate of the hybridization.

The melting temperature (T_m), one of most important parameters of the hybridization, is the temperature point in a hybridization reaction at which 50% of the nucleotides are annealed in the form of double stranded (ds) DNA and 50% are denatured (ssDNA). The stability of the DNA is directly dependent on the GC content. The higher the portion of GC pairs is, the higher the T_m, because the GC pair is more stable because of three hydrogen bonds, compared to only two for AT pair. With increasing GC portion, the hybridization energy also increases leading to a higher T_m. For the oligonucleotides longer than 50 bases from pH 5-9 (Bolton et al. 1962),

If the salt concentration is from 0.01M to 0.2M, T_m can be calculated from Eq. 36:

$$T_m\,(^oF)=81.5+0.41(G+C)+16.6\ \log M-500/L \quad (36)$$

M is the salt concentration, and G+C is the molar percentage of guanine plus cytosine. L is the length of oligonucleotides. For salt concentration above 0.4M, the T_m is calculated following Eq. 37:

$$T_m\,(^oF)=81.5+0.41(G+C) \quad (37)$$

While for the short oligonucleotides of 14-20 b.p. in 0.9M NaCl, the melting temperature is simplified (Rychlik et al. 1989):

$$T_m\,(^oC)=2^oC\times (A+T)+ 4\,^oC\times (G+C) \quad (38)$$

The nature of the probe DNA immobilized on the solid support provides a decrease in the melting temperature observed when both target and probe DNA are free in solution. The magnitude of the decrease is approximately 7-8 ^oC. The most reliable and accurate determination of melting temperature is determined empirically.

3.1.2.3 DNA immobilization on solid substrates

DNA immobilization on a solid support substrate plays a pivotal role in DNA biosensor research. Via crosslinker reactions, the DNA is bound covalently on the modified substrates eg. gold (Bain et al. 1988; Bain et al. 1989b; Bain et al. 1989a; Balachander et al. 1990), SiO_2, Si_3N_4 (Sakata et al. 2004), Ta_2O_5 (Ohtake et al. 2004b), and Al_2O_3 (Xu et al. 1994; Xu et al. 1995). Non-covalent DNA immobilization utilizes the electrostatic attraction to adsorb on poly-L-lysine, PEMs or various polymers (Fritz et al. 2002).

The covalent binding is preferred compared to the non-covalent binding for DNA immobilization because of the surface coverage, the orientation of the probe molecules and the stability of the probe interface.

For the covalent binding of DNA on different solid substrates, various silane and crosslinkers are employed. Commonly used silanes are mercaptosilane, aminosilane, epoxysilane and trichlorosilane.

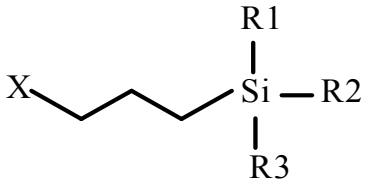

R_1, R_2, R_3=H, OCH_3, OC_2H_5, CH_3, CH_2CH_3, Cl (trichlorosilane only)

Mercaptosilane X=-SH

Aminosilane X=-NH_2

Cholorosilane X=-Cl

Epoxysilane X=

Fig 3.5 General structure of various silanes

Prior to the silanization, the solid support surface needs to be cleaned and activated to form one of the following three kinds of silanols: single (isolated) silanols, silanediol (germinal) and silanetriol (see Fig 2.11). A proper cleaning and activation method should lead to as many as possible free hydroxyl bonds on the surface for the binding of silanes. This supports the formation of a highly uniform silane layer. The silane molecule binds with the R end to the activated solid surface, and the X end is the liquid exposed group to react with the molecules of interest.

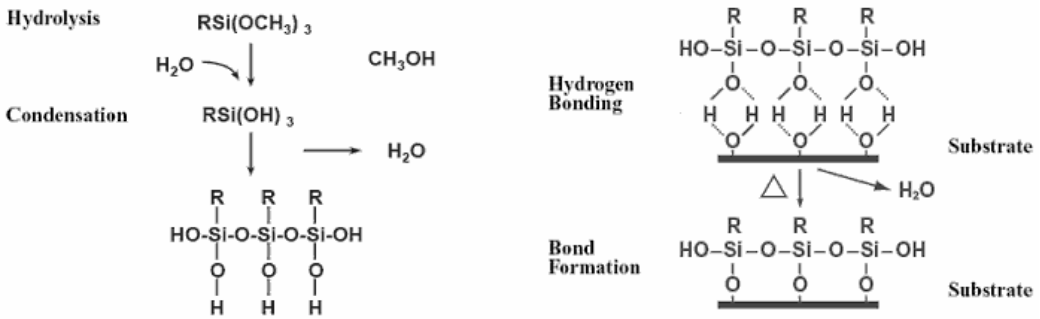

Fig 3.6 Hydrolysis of alkoxysilanes (left) and bonding to a solid surface (right) (Witucki 1993)

Hydroxylation and condensation control the silanization process. On the solid support surface, alkoxy groups of the silane firstly react with free hydroxyl groups via hydrogen bonds. Furthermore, if conditions are permissive, silanol groups condense to siloxane bonds by formation of Si-O-Si bonds. In this way, the silane forms a lattice on the solid support surface.

For DNA immobilization, usually crosslinkers are employed to connect the silane and the end-functionalized DNA. Over 300 different crosslinkers are currently available. They can be homobifunctional or heterobifunctional. Homobifunctional crosslinkers have two

identical reactive groups, which lack specificity and tend to self-aggregation. Heterobifunctional crosslinkers have two different reactive groups. Thus, these are very useful as conjugation between two different molecules. By modification of activation, silanization and crosslinking, the binding properties of the ssDNA sequence to the solid support surface and the ISFET gate are greatly enhanced.

3.1.3 Structure of streptavidin and the affinity reaction with biotin

Apart from the DNA detection, the biological affinity reaction between biotin and streptavidin was chosen to demonstrate the versatility of the ISFET biosensor. The biotin and streptavidin binding is one of the strongest affinity reactions in nature (Chaiet et al. 1964). This binding serves as a mode system for protein interactions, it has been extensively studied, and the binding process is well understood (Miyamoto et al. 1993; Star et al. 2003).

3.1.3.1 Protein structure

In nature, proteins are made from 20 different amino acids. Each protein has its own unique amino acid sequence. The protein has a primary (sequence), secondary (local folding), tertiary (long-range folding), quaternary (multimeric organization) and supramolecular (larges-scale assemblies) structure. Based on the primary structure, other noncovalent bonds also exist, like hydrogen bonding within the peptide backbone, hydrophobic effects, Van der Waals force and ionic bonds. Proteins show different properties and conformations due to these bonds.

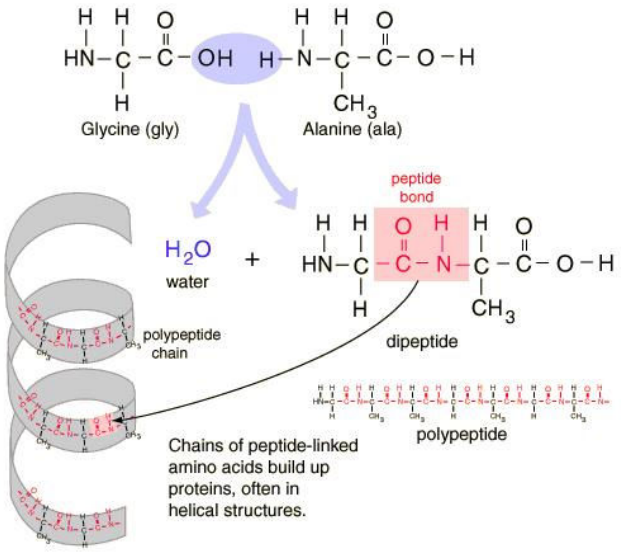

Fig 3.7 Formation of protein peptide from amino acids (Audesirk et al. 2005)

Proteins are very sensitive to the environment (pH, ionic strength). The isoelectric point (IEP) is defined as the pH at which the net charge of a protein is zero. Below the IEP, the protein bears a net positive charge, above it bears a net negative charge. Owing to a preponderance of weakly acid residues in almost all proteins, they are nearly all negatively charged at neutral pH.

3.1.3.2 Reaction of biotin with streptavidin

Streptavidin is a tetrameric protein purified from the bacteria streptomyces avidinii. Streptavidin binds strongly with biotin via a very strong, non-covalent reaction. The reaction of biotin and streptavidin is useful in affinity separations (Bayer et al. 1990), diagnostic assays, and delivery of therapeutics (Hnatowich et al. 1987; Kalofonos et al. 1990; Oehr et al. 1988).

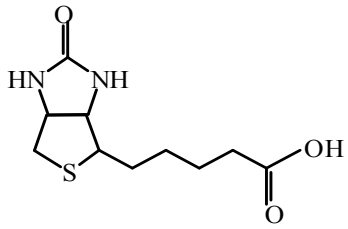

Biotin (vitamin H or B_7) (Fig 3.8) is soluble in water. Biotin assists cell growth and various metabolism chemical transfers, and maintains steady blood sugar level.

Fig 3.8 Structure of biotin

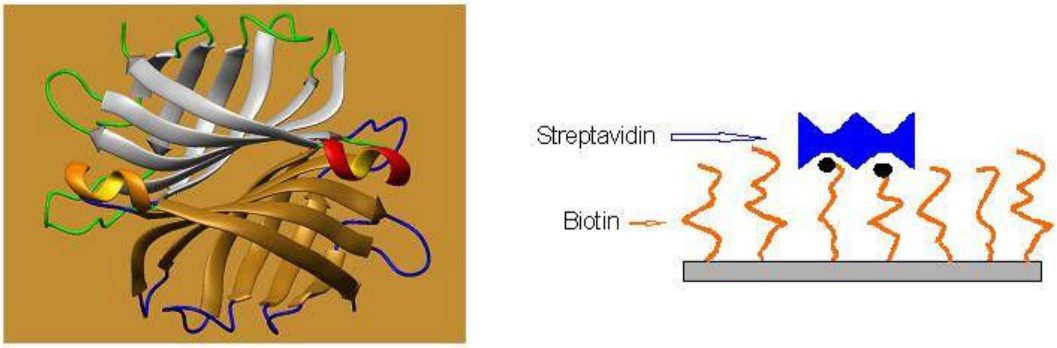

Fig 3.9 Space structures of streptavidin and the reaction with biotin, the reaction points of biotin with streptavidin are marked in black

In the symmetric structure of streptavidin, dimmers interdigitate coincidently with their dyad axes to form the naturally occurring tetramer. Four subunits are symmetrically located on the opposite faces, which are positioned in pairs. Each subunit contains a single biotin-binding site and has six tyrosine residues. The isoelectric point of streptavidin is pH=6.4 (Bullock et al. 1983) or 5-6 (Diamandis et al. 1991).

Multiple hydrogen bonds and Van der Waals interactions are associated with the biotin-streptavidin complex (Weber et al. 1989). The reaction is rapid and essentially non-reversible, and the complexes are extremely stable over a wide range of temperature, pH, organic solvents and denaturing reagents.

3.2 Characterization methods

The biosensing sensitivity and stability depend strongly on the surface modification leading to a covalent binding of probe biomolecules. The surface modification and the further biological reactions were characterized, analyzed and optimized with different surface analytical methods in this thesis. In the following the different methods are riefly described.

3.2.1 Contact Angle (CA) measurements

The contact angle was measured with an OCA20 system (Dataphysics, Germany) utilizing the Sessile Drop method with ultrapure water. Each substrate was dried with argon (Ar) before the measurements.

The CA measurement is a rapid, sensitive and simple method to characterize a solid surface. It offers surface energy related analysis of the activated surfaces and the silanized surfaces. When a liquid surface force is smaller than the contact force of liquid and solid, the liquid drop expands on the surface. This process is called wetting, on the other hand, nonwetting. The surface is then called hydrophilic or hydrophobic. Its condition is characterized with the degree value of the contact angle θ. Three characteristic diagrams for different contact angles are shown in Fig 3.10. The related explanations are provided in Table 3.1.

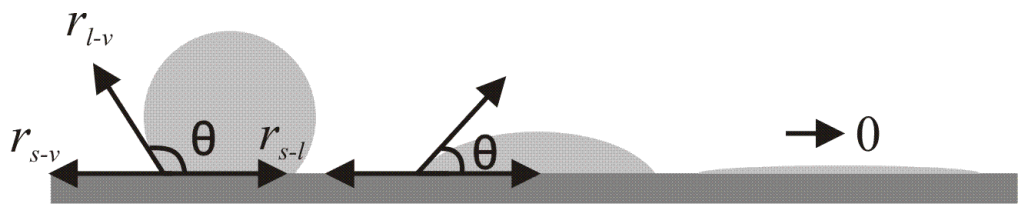

Fig 3.10 Different contact angles of liquid on solid support, the contact angle is $\theta>90^o$, $0^o<\theta<90^o$, and $\theta\rightarrow 0^o$, respectively

The Young's equation relates the contact angle with the different surface tensions:

$$\cos\theta = \frac{\gamma_{s-v} - \gamma_{s-l}}{\gamma_{l-v}} \tag{39}$$

With γ being surface tension, s stands for solid, v for vapor and l for liquid.

Table 3.1 Different contact angles and wetting conditions according to the Eq. 39:

Surface intention	Cosine CA	Contact angle	Wetting condition	Shape of liquid
$\gamma_{s-v} < \gamma_{s-l}$	$\cos\theta < 0$	$\theta > 90^o$	Completely not wetting	Sphere
$\gamma_{l-v} = \gamma_{s-l} - \gamma_{s-v}$	$\cos\theta = -1$	$\theta = 180^o$	Completely wetting	globular
$\gamma_{l-v} > \gamma_{s-l} - \gamma_{s-v} > 0$	$1 > \cos\theta > 0$	$0 < \theta < 90^o$	Can wet	lens shape
$\gamma_{l-v} = \gamma_{s-l} - \gamma_{s-v}$	$\cos\theta = 1$	$\theta = 0^o$	Completely wetting	no
$\gamma_{s-l} - \gamma_{s-v} > \gamma_{l-v}$	Not applicable			

The contact angle is related to the surface tension and other parameters, which determine the surface hydrophilicity and hydrophobicity. The substrate chemical groups making the water tend to wet or nonwet are distinguished into hydrophilic or hydrophobic groups. With surface groups like -OH, -NH_2 etc., the surface free energy is relatively high, and water droplets form low values of contact angle. With a higher density of the hydrophilic groups on the surface, the free energy is higher resulting in a lower CA. Several methods are utilized to measure the contact angles (Fig 3.11).

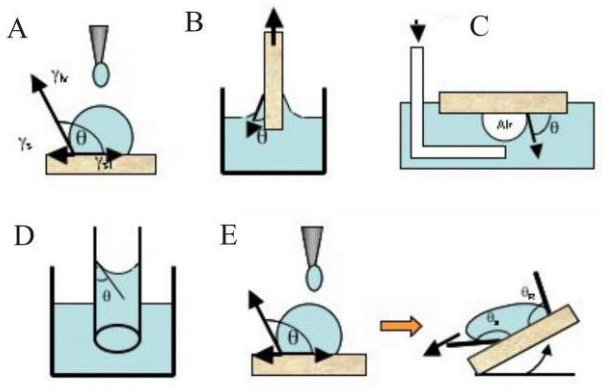

Fig 3.11 Five different methods to measure the contact angle. A. Sessile or Static drop method. B. Wilhelmy plate method, C. Captive air bubble method, D. Capillary rise method, E. Tilting substrate method (2006b).

Five commonly used CA measurement methods are shown in Fig 3.11. Among all the methods, the sessile drop method was used in this thesis with 1-3 µl Milli-Q water on the

differently treated surfaces.

3.2.2 Atomic Force Microscopy (AFM)

Topological images of the bare silicon and the modified surface were taken by a multimode AFM with Nanoscope IV controller and multimode base (Veeco Instruments, USA). The images were taken in air in the intermediate mode, which is combination of the usually applied contact mode and tapping mode. In this thesis, the surface topology of activated, silanized and bio-functionalized surfaces were monitored and compared to provide details on the surface modification efficiency.

The AFM (Binnig et al. 1986) utilizes a cantilever with a sharp tip to scan the material surface. The Van der Waals and other forces between the tip and the sample lead to the cantilever deflection, and this deflection is fed back to the detection system and analyzed.

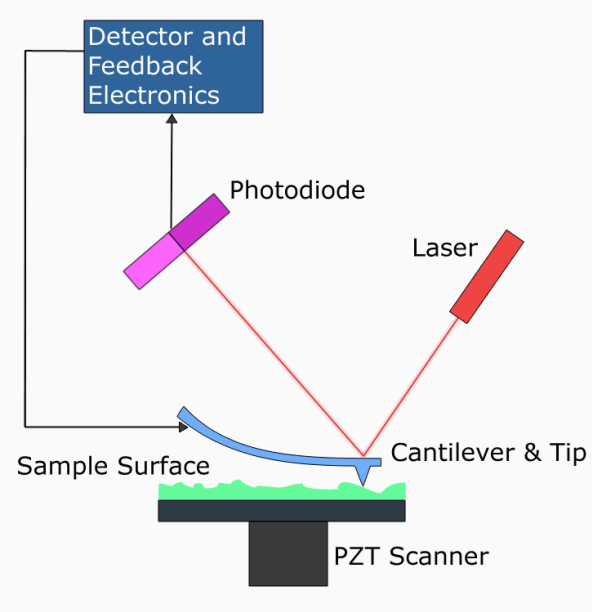

Fig 3.12 The block diagram for the Atomic force microscope. The deflection is measured using a laser spot reflected from the top of the cantilever into an array of photodiodes. The sample is mounted on a piezoelectric tube, that can move the sample in the z direction to maintain a constant force (Wikipedia)

The roughness of the surface is quantified by the root mean square (RMS) value R_q and the surface area difference (SAD). R_q represents the root mean square average of height deviations (Z_i) taken from the mean data plane $R_q = \sqrt{\frac{\sum Z_i^2}{n}}$. The SAD is defined as difference between the three-dimensional surface area (A_{3D}) and its two-dimensional surface area (A_{2D}) projection SAD = A_{3D}/A_{2D}. Surface roughness gives exact and detailed information about the topography of the surface.

3.2.3 Imaging Ellipsometry (IE)

Thickness and homogeneity of the samples in a larger image area compared to the AFM method were characterized by imaging ellipsometry (IE) (EP3, Nanofilm Germany, lateral resolution 2μm) equipped with a frequency doubled Nd: YAG laser (532 nm) and variable incident angle. The main usage of ellipsometry in this work was to measure the thickness of SiO_2 on silicon and the biomolecular layers on modified SiO_2.

The electromagnetic wave of light is composed of an electric component and a magnetic component, which are propagating sinusoidally. The electric part of the wave is polarized when touching a surface, with E_x and E_y (Fig 3.13). If the E_x (p) and E_y (s) components are having a arbitrary phase and amplitude, the light is called elliptically polarized. P and s polarizations are referred to as direction of parallel and perpendicular, respectively (Fig 3.13).

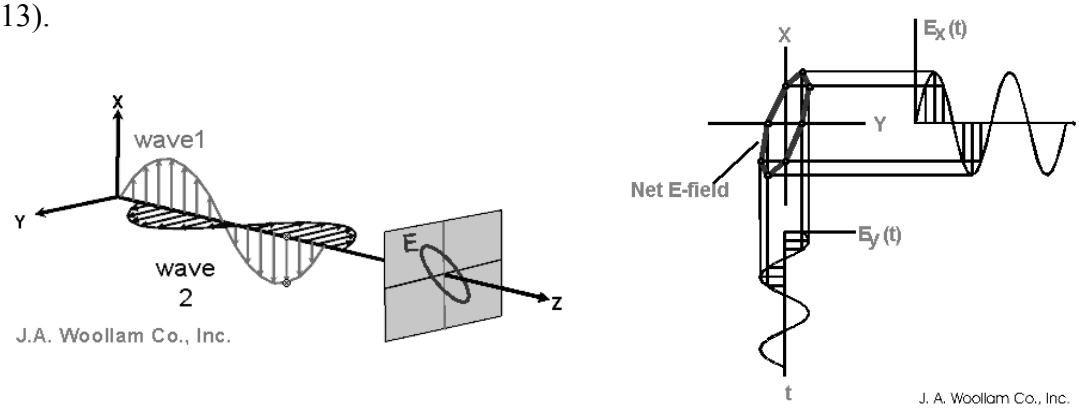

Fig 3.13 Electric wave at x and y axis. The depicted light wave is polarized elliptically (J. A. Woollam Co., Inc. USA) (2006c)

In an ellipsometry, the light passes through the polarizer (P) and the compensator (C) leading to a defined polarization of the incoming beam. The analyzer (A) is turned into an angle, where no light can pass to the photodetector. This condition is called “nulling”.

Ellipsometry uses polarized light, deriving its sensitivity from determining the relative phase change in a beam of reflected polarized light and greatly exceeds the sensitivity of an intensity reflectance measurement. The measured values are Δ and Ψ, related to the complex Fresnel reflection coefficients $\widetilde{R}_P$, $\widetilde{R}_S$ of p and s polarized light, respectively (Buzea et al. 2005).

$$\rho = \tan(\Psi)e^{i\Delta} = \frac{\widetilde{R}_P}{\widetilde{R}_S} \qquad (40)$$

The ratio is a complex number containing"phase" information. When a source of light is reflected from the surface, the polarization of the light wave is changing from linear to elliptical polarization. The change of polarization is characterized by the changes in the Δ and Ψ values. Δ is defined as a change in phase or phase difference, and Ψ is factor of amplitude ratio change.

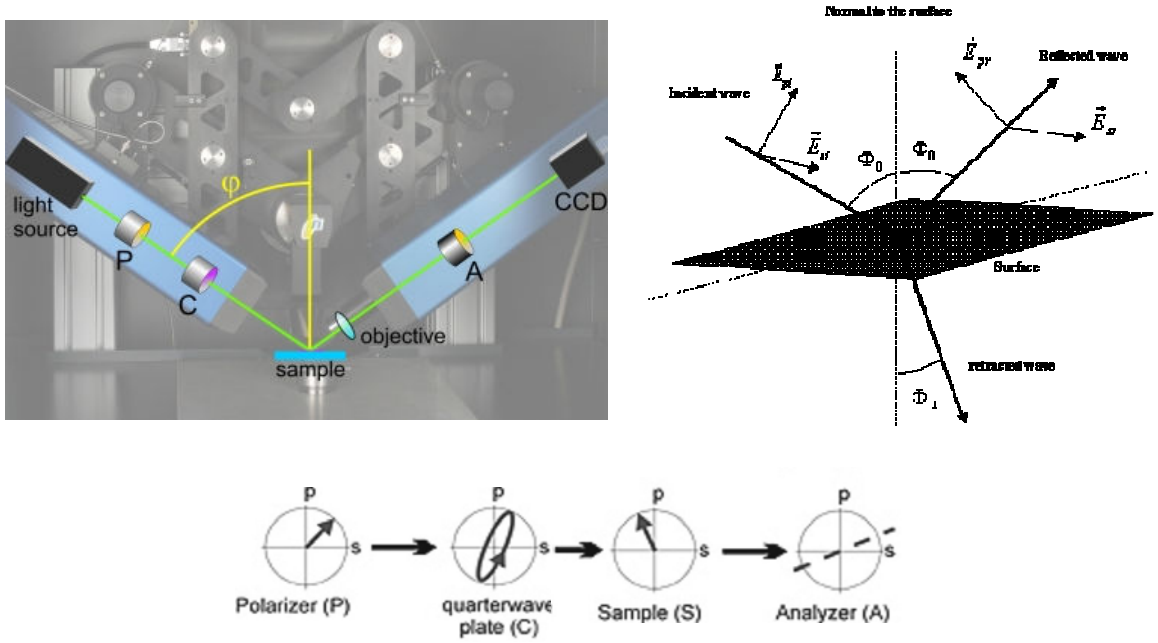

Fig 3.14 Principle of Image Ellipsometry (Nanofilm, Germany): upon the reflection on the sample surface, a linearly polarized light is generally elliptically polarized. The reflected light experiences a phase change, which is different for the electric field components p and s to the plane of incidence.

The sample surface is described by its refractive index (n) and extinction coefficient (k) depending on wavelength and temperature. The refractive index is related to the optical way of the wave through the sample and direction of propagation, and extinction coefficient to how much of the energy of the wave is absorbed in a material.

$$\Delta = \frac{2\pi}{\lambda} d(n_1^2 - n_0^2 \sin^2 \phi)^{1/2} \tag{41}$$

n_0, n_1 refractive index of medium and film, d thickness of film, λ wavelength of light, and ϕ angle of incidence.

Table 3.2 The refractive indices used in this thesis were as following:

Material	Refractive index	Literature
Si	4.1562	Nanofilm standard value
SiO_2	1.4605	Nanofilm standard value
APTES	1.4225	(Lide et al. 1994)
GPTES	1.46	(Lide 2004)
PSS/PAH	1.5228	(Gong et al. 2005)
PEI	1.4799	(2006d)
DNA	1.46	(Moiseev et al. 2006)
Biotin	1.5	(Haussling et al. 1991)
Air	1.003	Nanofilm standard value

3.2.4 Fourier Transform Infra-Red (FT-IR) Spectroscopy

FT-IR spectra were measured with a Fourier Transform Infrared (FT-IR) spectrometer (vector 22 and IFS 66v/s Bruker, Germany) with a reflection-absorption setup in dry air. The scanning range was 4000-500 cm^{-1} with a resolution of 4 cm^{-1}.

In general, the vibrations of atom-atom bonds are divided into three kinds, stretching vibration (symmetrical stretching vibration and asymmetrical stretching vibration), bending vibration (in plane bend and out of plane bend) and deformation vibration. These chemical bonds have specific frequencies at which they vibrate corresponding to their energy levels. This is often termed its “fingerprint”. During the FT-IR measurement, a source of light passes through a Michelson interferometer. If the frequency of the source radiation matched the frequency of the vibration of the molecules, radiation is adsorbed or transmitted. In this way, the bonds of the materials are presented in the FT-IR spectra.

In this work, FT-IE was utilized to analyze the bond formation to confirm the chemical reaction at the surface and to distinguish it from the possible physical force between the atoms.

3.2.5 Fluorescence microscopy

The fluorescence images were taken with a Zeiss Axioplan microscope (Axioplan 2 imaging). Derived from a conventional microscope, the fluorescence microscope introduces a higher intensity light to excite the sample.

According to the Jablonski diagram (Fig 3.15), when a molecule absorbs energy in the form of electromagnetic radiation, the electron jumps to a higher energy level because of this excitation. When the electron drops back to the ground state, it emits a photon. If the photon emission occurs between the same spin state (S→S), this is termed fluorescence. If the spin states of the initial and final energy levels are different (S→T), the emission is called phosphorescence. When the fluorescent species is excited, the emission peak makes a Stokes' shift to longer wavelengths because of the energy loss.

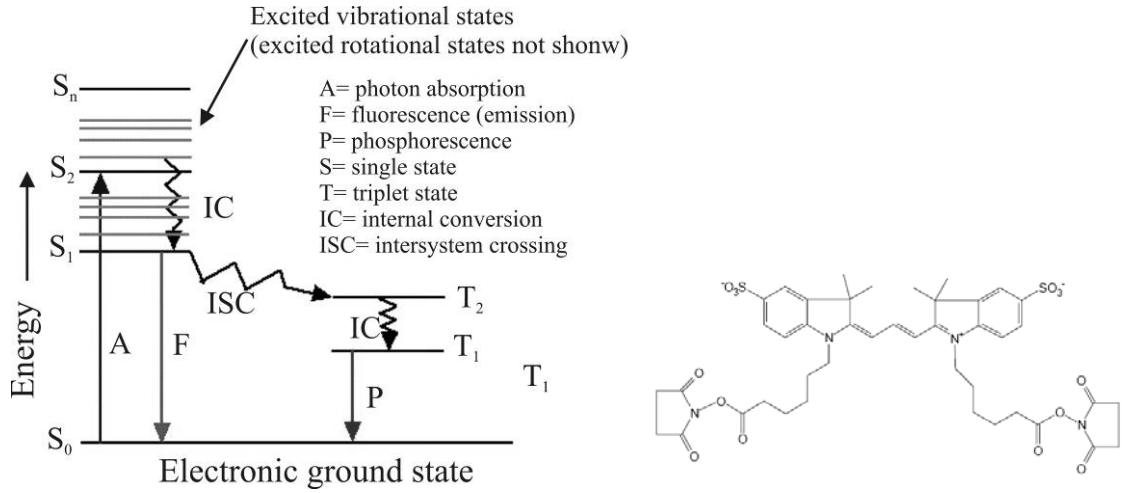

Fig3.15 Jablonski diagram (left) and structure of the Cy3 bifunctional fluorescence dye (right)

Cy3 is a widely used label agent in microarray detections and the only dye in this work to label the oligonucleotide. With the labeled DNA, the immobilization and hybridization reactions on the modified solid support were proved. The emission corresponded to the Cy3 dyes were detected at 570nm while it was excited at 550 nm. The fluorescence images were saved in JPG or BMP files. The images were further analyzed with the software ImageJ (2006e). The measure area was fixed for each sample and the mean intensity values for the pixel analysis were collected and compared.

3.2.5.1 Surface interference

When the source light passes through the samples surface, interference between incoming and reflected beam takes place.

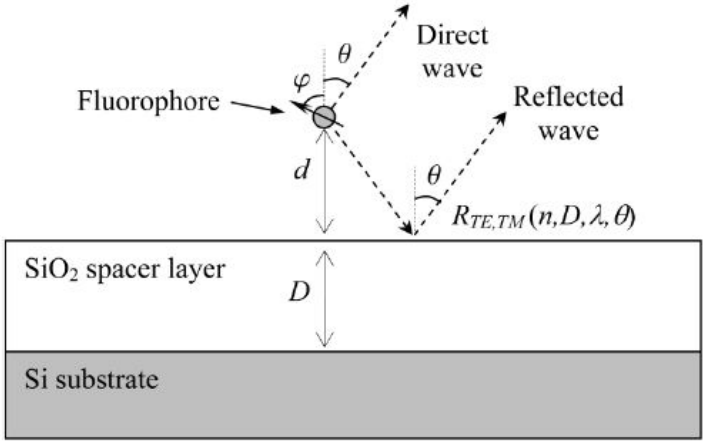

Fig 3.16 Schematic drawing of the geometrical arrangement of the fluorophore and the reflective substrate. The complex reflection coefficient R_{TE}, T_M contains the effect of the multiple reflections from the top and bottom of the SiO_2 interfaces. D is the thickness of SiO_2 layer, and d the thickness of surface modification (Swan et al. 2003).

Constructive and destructive interference were for enhancement or quenching of the chromophore emission which depend on the vertical distance. Destructive interference would occur at 1/2, 1, and 3/2 wavelength, every half wavelength, while constructive interference take place at 1/4, 3/4, 5/4 wavelength. Interference take place among three beams, the first is from the emission of the chromophore, the second is from the interface of the surface modification surface and air, and the third is from the interface of SiO_2 and Si. More simple calculations lead to the boundary condition that modification and SiO_2 must be around 1/4 of the wavelength, i.e. 138.5nm. The surface modification for covalent binding of DNA includes silanization, crosslinking and ssDNA immobilization. The whole thickness of the biomolecular layer is calculated to be about 8-10 nm (20b.p. DNA is 6.8 nm length). Therefore, the ideal thickness of SiO_2 is about 128.5-130.5 nm. For our experiments, we took 120nm SiO_2 on Si to perform the fluorescence experiments.

3.2.6 X-Ray Photoelectron Spectroscopy (XPS)

X-ray Photoelectron Spectroscopy (XPS) was used in this thesis to determine effectively

the composition of the modified thin films. XPS is a surface sensitive and widely used technique to obtain chemical information of various material surfaces. In this work, XPS analysis was performed with a XPS/AES spectrometer based on Physical Electronics components with a hemispherical analyzer. The X-ray source was monochromatic Al K_α radiation (hν=1486.6 eV) with an energy resolution of 1eV.

When the X-ray beam irradiates the surface, electrons in the core-level are emitted from the surface. The photoelectons are collected and analysed to produce a spectrum of emission intensity versus electron binding energy. In general, the binding energies of the photoelectrons are characteristic for the element from which they are emanated so that the spectra can be used for surface elemental analysis. Small shifts in the elemental binding energies provide additional information about the chemical state of the elements on the surface (Fig 3.17).

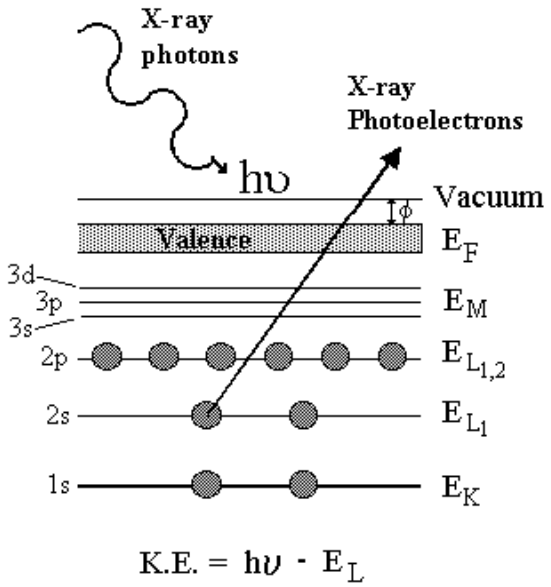

Fig 3.17 Schematics of the XPS process

The XPS data were analyzed with the UNIFIT software package (2006f), using Shirley background and fitting with Gaussian.

When analyzing the XPS data, the background was subtracted and the maximum intensity of each peak was set to 1. The atomic percentage of the elements concerned was calculated by dividing the peak area by the sensitivity factor and expressed as a fraction of the summation of all normalized intensities (Watts et al. 2003):

$$[\mathrm{A}]\,\text{atomic}\,\% = \left\{(I_A / F_A) / \Sigma(I / F)\right\} \times 100\% \qquad (42)$$

With I being intensity and F sensitivity factors. Binding energies (energy resolution ± 0.5 eV) were related to the binding energy of 285.0 eV of the CH_2 contamination and the quantification of the different compounds (rel-err. <15%). The proposed compounds were compared to the binding energies from the NIST database (2006g).

3.2.7 Aligned microspotting of biomolecules

A customer-made micro-spotting system with aiming option was developed in related projects (Kottuppallil 2006). It mainly comprised a XY table (BASALT UMT100 TETRA, Germany), a micro pipette and a dispenser unit (MicroDrop, Germany) mounted on a mini motor for Z axis motion (BASALT UMT100 TETRA, Germany) of the micro pipette and a CCD camera to view transistor XY position. The software for operation of the system was implemented in Labview 7.0 (Kottuppallil 2006).

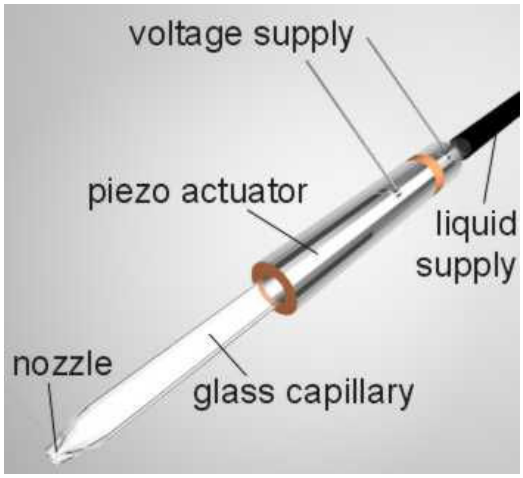

Fig 3.18 The core microdispenser systems of microdrop consists of a glass capillary, which is surrounded by a piezo actuator. Applying a voltage pulse to the piezo releases a small droplet of the spotting solution (2006h).

The insides structure of the microdrop dispenser is shown in Fig 3.18. At the nozzle, the pressure is transduced into a highly accelerated motion, which expels a small droplet with velocity of 1.5-3m/s. The droplet diameters are 30-100µm depending on the nozzle diameter. The resulting droplet diameter on the surface mainly depends on the hydrophilicity of the surface and was about 100nm in our experiments.

This unit allowed precise spotting of biomolecular samples to the individual channels of the chip without overlapping (Fig 3.19, gate pitch 200µm). The system offered an alignment accuracy of approximately 5µm.

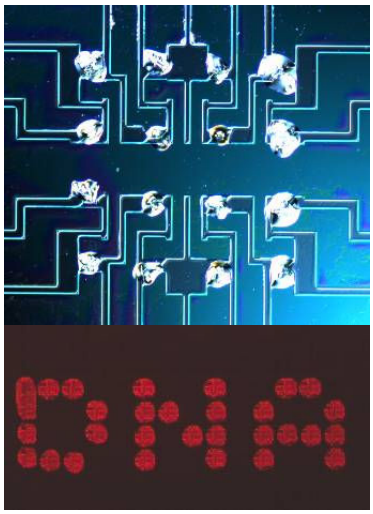

Fig 3.19 Image of Cy3-labelled ssDNA spotted on the transistor gates with the aligned microspotting system. The volume of the droplets was calculated to approximately 65pl

3.3 ISFET amplifier system

The p-channel ISFET chips and the basic low-noise amplifier system, which were used in this thesis were developed in previous works (Ingebrandt et al. 2001; Offenhausser et al. 1997b). The amplifier circuit for potentiometric readout was originally designed for extracellular recordings from neuronal and cardiac cells (Krause et al. 2000; Offenhausser et al. 1997a; Sprossler et al. 1998). The ISFET amplifier system was composed of a 16-channel amplifier circuit operated by a microprocessor, offered data transfer via an USB connection to the PC, and was fully operated by a readout software programmed in Delphi 5.0. All measurements were carried out with a small electrochemical reference electrode (Dri-RefTM, SDR2, World Precision Instruments, Germany) as ground contact to the electrolyte. For the measurements in the present work a flow-through cell for liquid handling was developed.

3.3.1 ISFET amplifier setup

The ISFET amplifier system went through three stages of developments in the time frame of this thesis.

The basic DC ISFET 16-channel amplifier was described in (Uslu 2003; Uslu et al. 2004). In short, the FET chips were operated in the constant voltage mode, where a constant drain-source voltage V_{DS} and a constant gate-source voltage V_{GS} defined the working point of the device. Changes in the drain-source current I_{DS} were converted by the first amplification unit into voltages by a factor of (V_{out}=-R×$I_{DS,}$ R=*3.3, 5, 10 kΩ*). The signals were further amplified by a second stage in the main amplifier, which can be operated in 1× or 100× amplification, respectively. At the beginning of the time-dependent potentiometric readout, the constant currents I_{DS} of the 16 transistors in the working point were compensated to zero by applying an individual voltage V_{comp} for each channel. Schematics of the potentiometric signal readout circuitry is shown in Fig 3.20. With a small heating plate, which is in thermal contact with the Si-chip, a constant temperature during the experiment can be maintained.

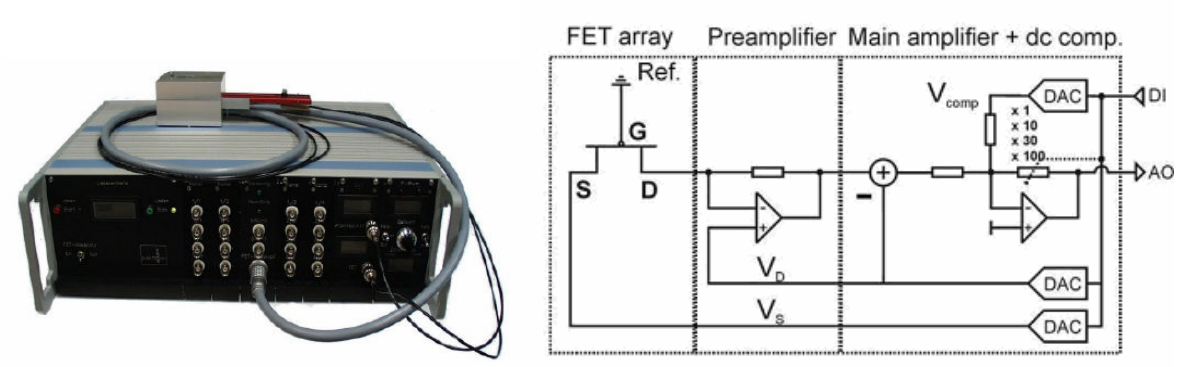

Fig 3.20 Photograph of the amplifier system and the schematics of the amplifier circuitry for potentiometric dc readout. Only the circuitry for a single channel is shown. In the schematics, digital to analog converters (DAC) are providing the source voltage V_S, the drain voltage V_D and the compensation voltage V_{comp}. The electrolyte solution is set to ground potential via a reference electrode.

The miniature amplifier which was mainly used in this work, was further modified for detection of biomolecules (Han et al. 2006b; Sakkari 2005). The whole amplifier system was mounted inside aluminum housing and the upper cover had a rectangular hole for chip mounting (Fig 3.21).

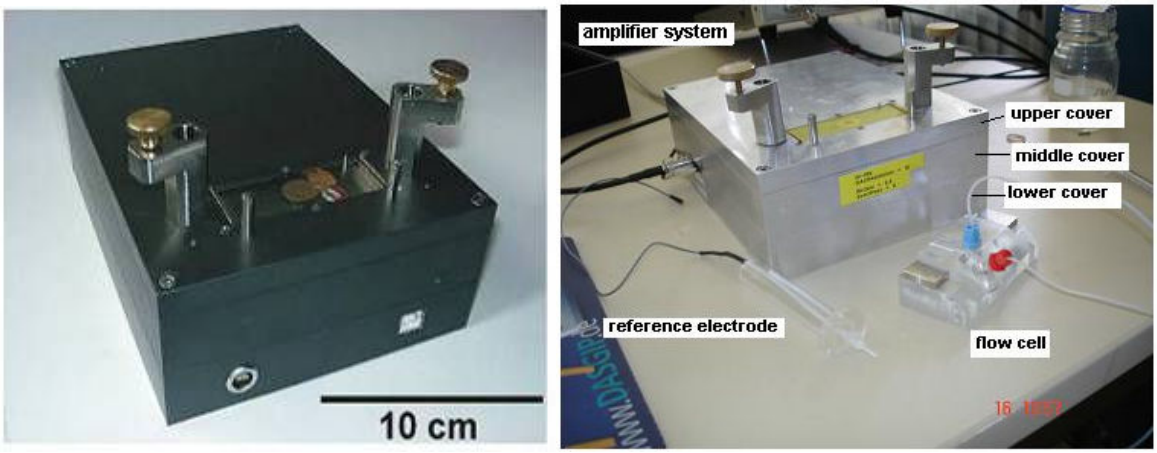

Fig 3.21 The amplifier system with reference electrode and flow cell. Two different amplifier generations are shown.

A flow cell provided in and out flow of liquid and held the Ag/AgCl reference electrode. The individual drain contacts of the FETs were connected to the inputs of the operational amplifiers. The current inputs (I_{DS}) were converted to voltage signals and amplified. The upper part of the systems was occupies by the head stage preamplifier with a heating plate. The middle cover consisted of the main amplifier unit. In the lower part, a microcontroller was used to sample the signals. The boxes contains the voltage supply and a COM/USB

converter. The systems read out the signals from 16 channels simultaneously. Furthermore, one channel was used as the reference channel.

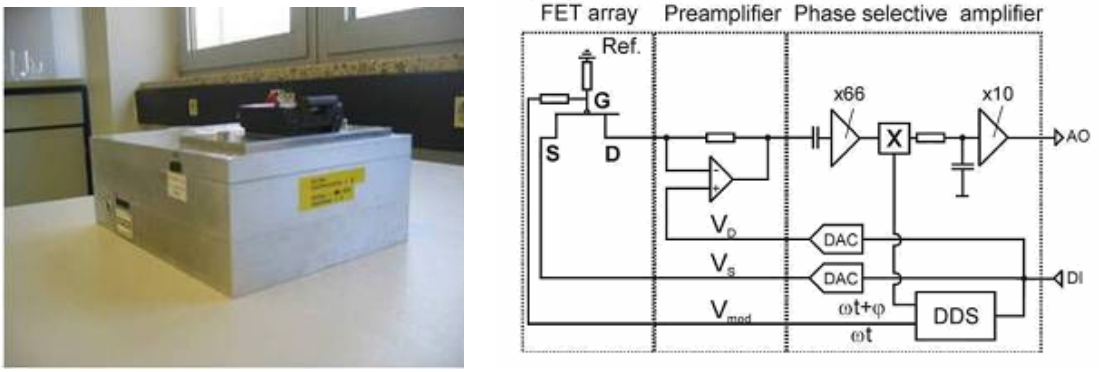

Fig 3.22 Photograph of the amplifier system and schematics of the amplifier circuitry for impedimetric readout of the transistor transfer function in AC mode. For the phase selective amplification, a direct-digital-synthesis device (DDS) provided the modulation voltage V_{mod}, which was fed in via the reference electrode. The phase selective amplification was confirmed by a frequency multiplier device (box marked with an X).

The schematics of the AC readout system for transfer function scan with different functional subunits is shown in Fig 3.22. For the impedimetric signal readout, independent frequency-selective amplifiers were built into the system. It contained 16 readout channels in total providing parallel operation of two 8-channel chips. The scan of the transfer function was done by feeding a sinusoidal test signal V_{mod} with 20 mV amplitude and varying frequency from 1 Hz – 100 kHz to the reference electrode. For this purpose, the chips were operated in the same working point of highest transconductance as in the DC readout mode. A direct-digital-synthesis (DDS) device provided test signals of exact amplitude, frequency and phase. Frequency-selective amplification was confirmed via a frequency multiplier device, which was built into a capacitive de-coupled amplification cascade. A summary of the different amplifier system used in this thesis is provided in the appendix.

3.3.2 Equivalent circuits for signal interpretation

To explain the effects for transfer function detection, equivalent circuits are used to simulate the recordings. A circuit simulation software (PSpice, Cadence Design systems, Inc.) was used to model the basic cut-off frequency of the system upon changes in ionic

strengths of the solution (Sakkari 2005). Modification of the gate input impedance in the circuit can also model the attachment of biomolecules to the ISFETs.

In Fig 3.23, the basic equivalent circuit for the ISFET plus first amplifier stage including the double layer on the SiO_2 surface is depicted. The signs of components and explanations are shown in Table 3.3.

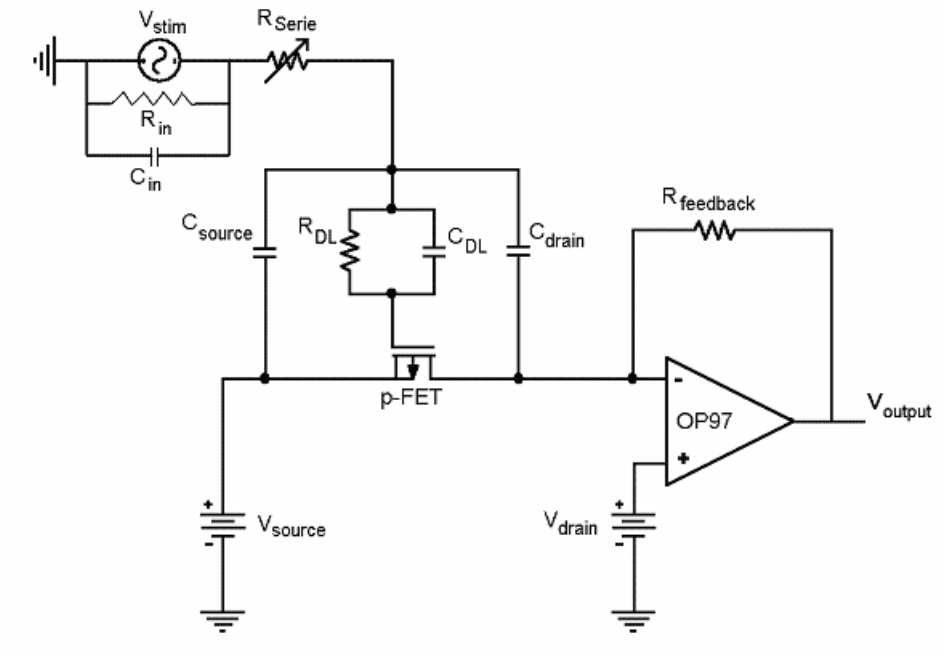

Fig. 3.23 The equivalent circuit model of the electrolyte/conductivity measurement setup.

In the equivalent circuit, the electrolyte resistance (R_{serie}) as one of determination factor can be extracted from the measurements. The input DC voltages were applied at the source and drain, while an ac signal with amplitude of 20mV and variable frequency was imposed. In addition, a low-pass circuit (R_{in}, C_{in}), which corresponds to the input of the amplifier system, needs to be inserted into the circuit to account for the imperfect input signal source. This low-pass filter at the input stage has a major influence on the overall cut-off frequency of the amplifier system in the higher frequency regime (>100kHz). The double-layer capacitance, which was calculated from the literature (Morrison 1980), is also included in series to the gate capacitance. However, the influence of the double-layer capacitance can be neglected in our simulations.

Table 3.3 Full description for the components of the equivalent circuit in Fig 3.22

V_{stim}	Sinusoidal signal source of amplitude 20 mV and variable frequency
R_{in}	Input resistance of the signal input
C_{in}	Input capacitance of the signal input
R_{Serie}	Electrolyte resistance plus reference electrode resistance
C_{source}	Common source capacitance
C_{drain}	Combined capacitance of the working drain contacts
C_{DL}	Double-layer capacitance at the gate surface
R_{DL}	Double-layer resistance at the gate surface
p-FET	Standard Berkeley FET model (berkeley.olb)
$R_{feedback}$	Feed-back resistance at the first amplifier stage
OP97	Standard Lineartech amplifier model (op97.olb)
V_{source}	Voltage supply to the source contacts
V_{drain}	Voltage supply to the drain contacts

The first amplification stage of the FET amplifier setup (OP97), which was used as voltage converter was included in the equivalent circuit. In our model circuit, a standard Berkeley p-FET model (berkeley.olb) and a Lineartech OP-97 model (op97.olb) were used. All the influential simulation parameters with their simulation values are listed in Table 3.4.

Table 3.4 Simulation parameter values

Simulation parameters	Simulation values
V_{stim}	Sinusoid 20 mV, variable frequency
R_{in}	10 kΩ
C_{in}	1 pF
R_{Serie}	370, 210, 64, 20.5, 4.8, 0.43 kΩ
C_{source}	97 pF
C_{drain}	372 pF
C_{DL}	2.4 pF
R_{DL}	3 GΩ
$R_{feedback}$	10 kΩ
V_{source}	2 V
V_{drain}	1 V

This basic circuit needed to be adapted for the respective measurement boxes (see Appendix) and the different experiments. Varying C_{source} and C_{drain} can model different chip designs. For the amplifier generations, the OP model needed to be changed and the influence of the respective reference electrode needed to be considered. As a first order approximation, the influence of a biomembrane can be included by adding an RC circuit composed of C_{mem} and R_{mem} (or C_{DNA} and R_{DNA}) between the double layer components and the FET model. In summary, the PSpice simulation can provide qualitative information about the influence of the different components to the circuit and the recorded signals. For the deeper understanding of the biomolecules detection experiments, a more elaborated interpretation is needed.

Chapter IV Results and Discussions

In this chapter the step-by-step optimized surface modification including a series of reactions on control substrates and on fully encapsulated ISFET devices gate surfaces is presented. The optimization was done for each reaction step leading to the covalent binding of the biomolecules. Based on this surface modification, PEMs, DNA hybridization and biotin/streptavidin binding were monitored by the ISFET devices as function of potential and/or impedance change at the gate surfaces.

4.1 Surface modification

Surface modification is vital to ISFET selectivity and sensitivity of measurements. During this work a “mild” standard protocol for the covalent attachment of probe biomolecules was developed. This multi-step protocol was tested on silicon dioxide control substrates. Care was taken for a “mild” protocol to be compatible with the fully encapsulated ISFET devices for the further electrical detections, which are presented in the paragraphs 4.2 and 4.3.

4.1.1 Defined interface architecture for the ISFET sensor

Surface modification based on cleaning and silanization of glass slides and silicon oxide surfaces is a basic requirement to build up biocompatible layers for the attachment of biomolecules (e.g. DNA, proteins, tethered lipid membranes,…) on solid surfaces (Balladur et al. 1997; Haller 1978; Maskos et al. 1992; Shirai et al. 2000). A wide variety of wet cleaning and silanization protocols including different crosslinkers for the further attachment of biomolecules were described in related publications (Chrisey et al. 1996; Duman et al. 2003; Kurth et al. 1993; Strother et al. 2000; Wang et al. 2001).

In an 'ideal' protocol, the cleaning does not affect the topology of the surfaces, contaminations are completely removed and the surfaces are activated to expose a high density of hydroxyl groups to the electrolyte. In this thesis, we were additionally aiming at a surface modification method, which can be applied to our fully encapsulated, non-metallised field-effect-transistor (FET) arrays. The protocol should not harm the thin gate oxides (9 nm SiO_2) and the encapsulation, thus enabling multiple re-use of the sensors. Surface modification should lead to a monolayer, because the sensitivity of our FET sensors to charged macromolecules in weak electrolyte solutions was found to decrease with vertical distance from the gate surface (Uslu et al. 2004).

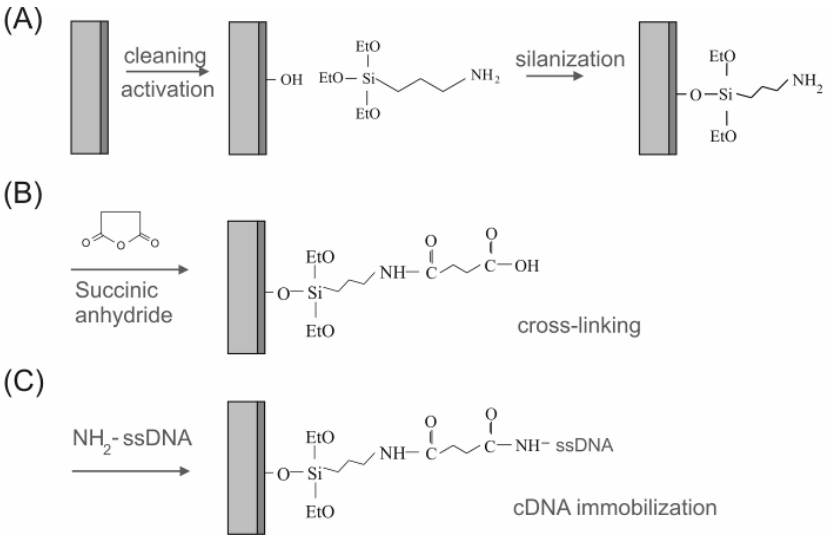

Fig 4.1 Step-by-step scheme of the surface modification. (A) The surface was cleaned and activated by formation of -OH groups and further functionalized by silanization with APTES. (B) Succinic anhydride was used as cross-linker molecule for the further covalent attachment of amino-terminated ss DNA (C)

In Fig. 4.1 the whole step-by-step surface modification process are depicted. Firstly, the

SiO_2 surface was cleaned to generate a maximum density of -OH groups on the surface. Next the -OH groups react with 3-aminopropyltriethoxysilane (APTES) either in gas phase or in liquid phase (Fig. 4.1A). The silanization process left the amino groups exposed for the further reaction with succinic anhydride, which acted as crosslinker to connect the silane and the biomolecules (Fig. 4.1B). Amino-terminated probe ssDNA can then be covalently attached to the chip surface. Biotin will immobilize directly on the silanized surface without crosslinking. In the following, all the subsequent steps of the surface modification are optimized and characterized with the different surface analysis methods.

4.1.1.1 Effect of the cleaning and activation procedure on the surface topology and contact angle

Common cleaning methods for glass and SiO_2 surfaces include wet chemical (Cras et al. 1999; Kern et al. 1970; Lim 2003), UV-ozone (Zazzera et al. 1993), or plasma cleaning procedures (Kim et al. 1996). We intended to use a wet cleaning method, which effectively cleans the surface and leads to a highly hydrophilic interface, without harming the thin gate oxides and encapsulation of the FET devices. It is to be noted, that in any case a cleaning step is necessary after fabrication and encapsulation of the FET devices, because the FET surfaces are covered with photoresist during fabrication.

The original oxide surfaces may contain different kinds of contaminations such as organic or metal impurities and various particles, which are fixed to the surface by weak electrostatic forces or by the Van der Waals force. After the different cleaning steps the particles should be removed resulting in a change in surface roughness. In general, the activation solutions should minimize the water contact angle on the surface indicating a formation of a hydrophilic surface with a high number of -OH groups. Usually, contact angle analysis provides a quick and simple means of assessing the reactivity of the surface and allows for general comparisons providing a qualitative test. However changes in surface topology might additionally influence the CA results (Zisman et al. 1964). Therefore we monitored the contact angle and the topology changes by AFM at the same set of samples.

Silicon wafers (p-doped, 5 Ohm cm) were cleaned according to the RCA method (Kern et al. 1970), thermally oxidized (dry oxidation at 820°C) and cut into 10x10 mm^2 pieces. These chips were used as test devices for the different surface modification methods. In

addition, fully encapsulated FET devices were immersed into the solutions to test the stability of the encapsulation. The thermal oxidation protocol for the control substrates was identical to the gate oxide formation step during fabrication of the FET devices (Ingebrandt et al. 2001; Ingebrandt et al. 2003). Oxide thicknesses of 8.7±0.2 nm and uniformity of the samples were confirmed by IE. For initial cleaning, the surfaces were rinsed with ethanol, ultrasonicated for 5 min in 2% Hellmanex (Hellma, Germany), rinsed with ultrapure water (Milli-Q, Gradient A10 18.2 MΩ, Millipore Inc., Germany) and finally sonicated for 3 min in ultrapure water. After these steps, the samples were immersed for 30 min in the different activation solutions and finally dried under argon (Ar). The activation solutions were containing various inorganic acids or bases. (A. MeOH/HCl [V:V=1:1]; B. Method A+conc. H_2SO_4; C. Piranha [30% H_2O_2: conc. H_2SO_4=1:3]; D. Conc. H_2SO_4; E. $K_2Cr_2O_7$+H_2SO_4; F. 1 M NaOH). APTES was diluted in ethanol to be 5 % (V/V) and the silanization was carried out overnight. Post-treatment of the silanized chips was done by rinsing with dilute anhydrous acetic acid (1 mM AcOH).

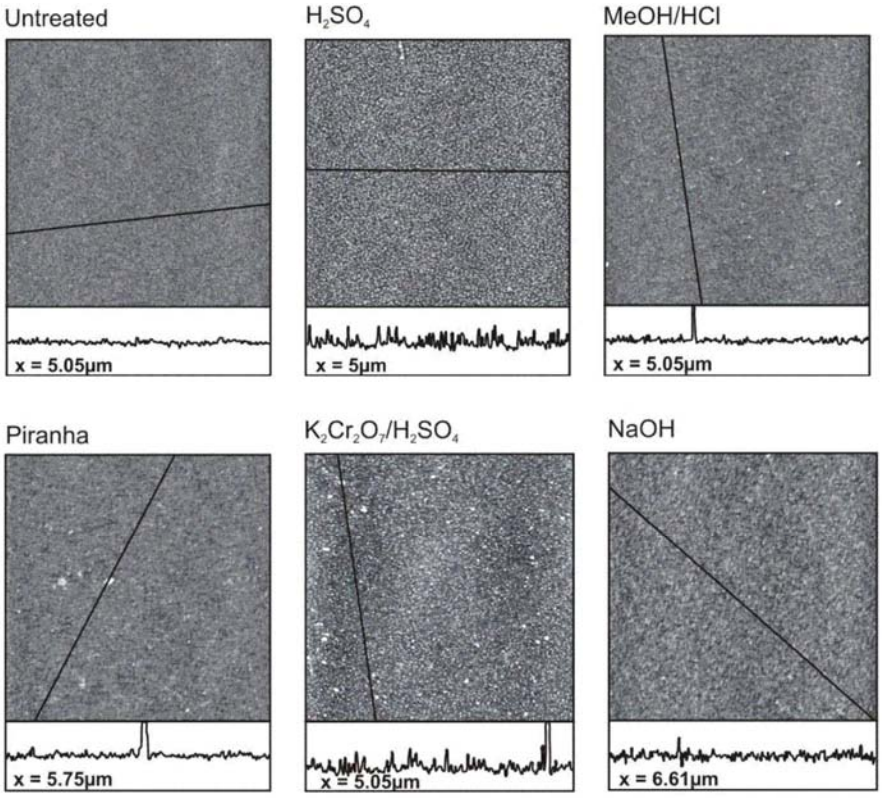

Fig 4.2 AFM images of the surfaces, which were treated with the different activation solutions. The area size is 5×5 µm^2. Line scans are provided with which the surface roughness can be compared. The lines are indicated in the respective AFM image. The line scans were scaled to the same z-axis (z=4nm) to aid better comparison between the samples (Han et al. 2006a)

Table 4.1 Contact angles, roughness values measured by AFM and etching rates measured by IE for the different wet activation produces. In the last column, the contact angles for the differently treated surfaces after silanization with APTES (contact angle value is the average of n=20 measurements) are shown. The values for roughness are given as RMS roughness Rq in nm and as surface area difference (SAD) in percent. Only two out of the six different methods were compatible with out standard encapsulation material for the FET chips (Han et al. 2006a).

	CA (n=20)	R_q (nm)	SAD (%)	Thickness loss (nm)	Harmful to encapsulation	CA (n=20) APTES
Original SiO_2 surface	47.7°	0.12	0.01	---	---	---
A MeOH/HCl	24.6°	**0.11**	**0.01**	**0.4**	**no**	**37.1°**
B A+conc. H_2SO_4	**16.9°**	1.66	0.18	0.8	yes	**38.9°**
C Piranha	24.2°	**0.11**	**0.01**	**0.6**	yes	54.9°
D Conc. H_2SO_4	**16.9°**	0.29	0.08	0.8	yes	64.6°
E $K_2Cr_2O_7$+H_2SO_4	**11.7°**	0.24	0.06	**0.7**	yes	54.2°
F 1 M NaOH	37.6°	**0.16**	**0.02**	0.9	**no**	66.3°

In Table 4.1, the different acid and base cleaning methods are compared with respect to the resulting contact angles (n=20, 1µl ultrapure water). The contact angles were taken within 20 s after formation of the sessile drop. After each cleaning step, the roughness of the surfaces was detected by AFM and compared with the values before activation. The SAD provides a measure for the effective surface area of the solid-liquid contact. This aspect is of particular interest for the electrical characterisation especially for the calculation of the interface capacitance of the sensor chips. In addition, Table 4.1 includes the etching rates (for 30 min each) for the different activation solutions measured by IE.

The initial CA for the untreated samples was 47.7°, and after ultrasonification in Hellmanex, the CA was decreased by 4°. Following this pre-cleaning step, the different activation solutions were applied. Method A resulted in a CA of 24.6°, and did not increase the surface roughness. In the case of method B, the mean roughness of the surface increased from 0.12 nm to 1.66 nm, whereas the CA was further decreased. The similar CA values for methods A and B can be caused by the strong increase in surface roughness for sample B. Such a topology effect to the contact angle values should be even more pronounced at low CA values (Zisman et al. 1964). Method C utilizing hydrogen peroxide is part of a standard method to clean semiconductor wafers (Kern et al. 1970). In our study,

this method showed comparable values to method A in terms of contact angle, roughness values and thickness loss. It would be an effective cleaning method, but the aggressive procedure is so far not compatible with our device encapsulation. Method D and E are both utilizing strong oxidants, which are known to oxidize most organic and inorganic compounds. In our study, both methods increased the surface roughness significantly. In contrast to the other methods, method F uses a strong basic solution, which caused the highest thickness loss and was incompatible with our encapsulation, too.

In summary of all values given in Table 4.1, method A was the most suitable for our further studies. It showed the lowest roughness increase of the surface, and had the least etching rate and was compatible with our encapsulation material. The RCA cleaning method (Kern et al. 1970) showed similar performance, but so far it cannot be applied to the encapsulated FET devices.

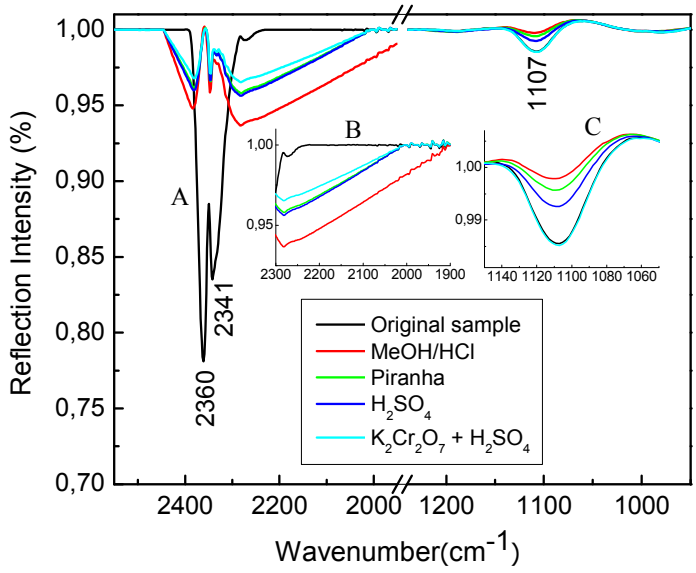

Fig 4.3 A) FT-IR reflection spectra for the activated silicon oxide surface. The two pronounced peaks at 2360 and 2341 cm^{-1} of the original sample are caused by free CO_2 in the sampling area and are not related to the sample surface. B) In the detailed view of the spectrum an increase of the signal around 2100 cm^{-1} can be seen, which is related to the formation of Si-H_n and SiO-H groups at the surface and which is strongest for the MeOH/HCl solution. C) the treatment with MeOH/HCl shows the largest decrease of the 1107 cm^{-1} signal (Si-O stretching vibration) indicating the opening of Si-O bonds at the surface. Here the MeOH/HCl was the most potent activation solutions, too (Han et al. 2006a).

We confirmed the activation effect of the different solutions by FT-IR. In Fig 4.3, FT-IR differential spectra before and after activation with the different solutions are shown. The two prominent peaks of the untreated sample at 2360 and 2341 cm^{-1} are attributed to free CO_2 and are not related to the sample surface (Barres et al. 1987). The peak at 1107cm^{-1} is known from routine measurement of interstitial oxygen in silicon wafers. This absorption band is associated with the Si-O stretching vibration in the silicon lattice (Sun et al. 1992), and is mainly originating from oxygen precipitates inside of the silicon wafers. However, it is possible to relate a change in this peak intensity to surface reactions (Lu et al. 2005). The broad adsorption band, which is occurring at around 2100cm^{-1}, is related to the formation of Si-H_n (n=1, 2, 3) (Makino et al. 2005) and SiO-H groups (Aydil et al. 1994) on the surface of the sample. The increase in this intensity (Fig 4.3B) and the decrease in the peak frequency of the Si-O stretching vibration at 1107cm^{-1} (Fig 4.3C) supports that silicon-oxygen bonds are opened and silicon-hydrogen bonds are formed at the surface during the treatment with the activation solution. Compared with the different cleaning solutions, the MeOH/HCl solution was the most potent in terms of Si-O bond opening and Si-H_n and SiO-H group formation.

4.1.1.2 Dependence of the silane thickness on silanization time and posttreatment

In general, the silanization process can be performed with various silanes and under different conditions. Generally, silanization procedures change the free energy of the surface by conversion of the surface groups. Especially during the silanization with APTES, the reaction mechanism is assumed to pass three distinct phases (Silberzan et al. 1991), resulting in the exposure of amino groups to the electrolyte. Therefore, the amino-surface is prone to react with water resulting in a hydrophilic surface. In Table 4.1 it can be seen that the contact angles after wet cleaning of the surfaces ranged from 37.1^o to 68.9^o depending on the different activation solutions. Of all the procedures, method A and B, which both employed the MeOH/HCl mixture, resulted in CAs below 40^o. Taking roughness and thickness of the thin oxides after the cleaning step into account, we conclude that Method A is the best wet cleaning procedure for our purposes.

Generally, CA measurements provide just a macroscopic characteristic of the surface and cannot distinguish between monolayer and multilayer coverage. The APTES silanization

process was compared with (3-glycidyloxypropyl) trimethoxysilane (GPTES) silanization under different atmospheres (gas and liquid).

To estimate the thickness of the resulting silane layers with increasing silanization time, the substrates were immersed in the APTES solution and stored in an oven at 50°C for 20 min, 1 hour, 3 hours, and overnight (22 hours), respectively. The GPTES solution in room temperature was applied inside a glove box with the same time intervals. APTES was diluted 5% (V/V) in ethanol, while GPTES was in the solution of GPTES: oxylene: N,N-Diisopropylethylamine (DPEA) with 25: 222: 3 (V: V: V).

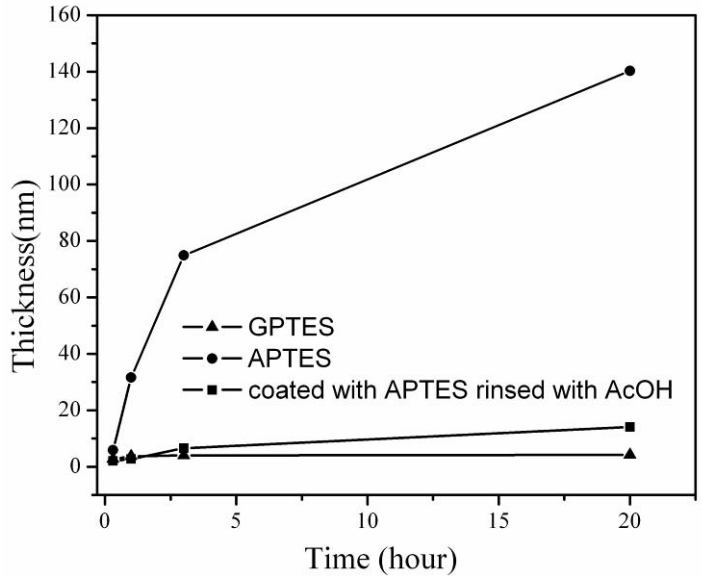

Fig 4.4 Thickness values (ellipsometry) for the different silanes with APTES or GPTES as the function of silanization time from 20 minutes, 1 hour, 3 hours to 22 hours

In Fig 4.4 the thickness change of the APTES and GPTES layers as function of time are shown, respectively. APTES tends to accumulate on the surface, resulting in a non-uniform layer, with a thickness up to 140 nm for the overnight treatment. To obtain a homogeneous surface, the chips were treated with 1mM anhydrous acetic acid (AcOH) after the silanization with APTES. After this rinsing step, the silanes were uniform with a thickness of less than 4 nm. It is important to obtain a very thin and uniform silane layer to achieve the maximum signal readout. The interaction of APTES and AcOH can be assumed according to (Han et al. 2003). AcOH activates the silane to form a network on the surface. Silane material, which is not strongly bound to the surface, is rinsed off resulting in a thickness decrease of i.e. 140 nm to less than 4 nm for the 22h silanization (Fig. 4.4). Interaction of APTES with AcOH is well known in forming silicate gels (Bekiari et al.

1998; Green et al. 1997). In other protocols reported in literature, a post-treatment of freshly silanized surface is done by rinsing the layers with the solvent in which the silanization was carried out. In our protocol, the rinsing step with 1mM AcOH resulted in reliably thinner silane layers compared with the usual rinsing with ethanol. In Fig. 4.5, the ellipsometry images of the substrates coated with APTES overnight, and after rinsing with AcOH are shown.

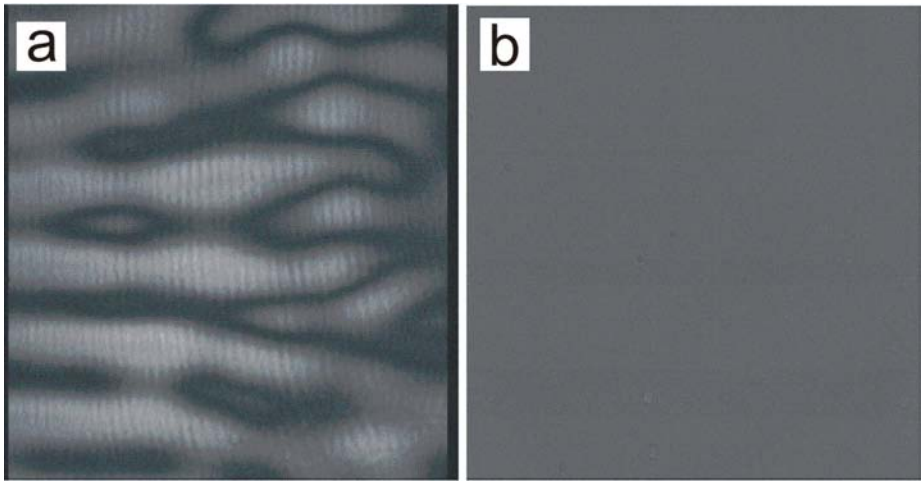

Fig 4.5 a) Imaging ellipsometry of a silicon oxide surface coated with APTES (overnight) and b) same surface area after rinsing with 0.001 M AcOH. Image size is 400×400µm^2 and the thicknesses of the APTES layers were measured to > 140 nm (non-uniform) for a) and < 4 nm (uniform) for b).

The chemical reaction on the surface can be followed by quantitative XPS measurements (Table 4.2), where the surface atomic compositions of the main elements inside the thin films were investigated.

Table 4.2 XPS quantification of elements percent for the surfaces of original sample, after activation with MeOH/HCl for 30min, after silanization in liquid phase and after the posttreated with 1mM AcOH.

	Original SiO_2 surface	30 min activation with MeOH/HCl	After silanization with APTES	After posttreatment with 1mM AcOH
C	14.5	12.0	52.2	36.6
O	65.1	51.5	26.0	40.3
Si	29.2	28.4	10.6	18.0
N	0.2	-	11.2	5.1

The pre-treatment of the surface with MeOH/HCl resulted in a clear decrease of the atomic content of carbon. This can be attributed to the removal of organic impurities, which were absorbed to the untreated surfaces before cleaning and activation. The activation led to an almost stoichiometric composition (1:2 for SiO_2) of the silicon oxide surface. The overnight silanization with APTES introduced amino groups and methylene to the surface, which can be verified by the increase of nitrogen to 11.2% and of carbon to 52.2%, which indicated a strong signal from the 140nm thick APTES layer. After rinsing with 1mM AcOH as post-treatment of the silanized surface, the carbon and nitrogen contents of the film on the surface were decreased indicating the removal of a part of the silane layer from the surface, which was consistent with the IE results, too.

4.1.1.3 Comparison of the APTES silanization in liquid and gas phase

Silanization with APTES can either be done in gas phase or in liquid phase. For the liquid phase silanization, the effect of different solvents was investiged. 1% APTES was diluted in different solvents of ethonal, tetrahydrofarum (THF), dimethyl sulfoxide (DMSO), N,N-dimethylformamide (DMF), N,N-dimethylacetamide (DMAc) and toluene and applied on the activated substrated surface for 10 minutes in 110^{o}C. After the silanization, the thicknesses were measured with IE. No significant difference among the different solvents was found. Considering the easy to control and the solubility of APTES, for liquid silanization, toluene was selected as solvent for APTES. 1% APTES in toluene was applied to the chips overnight, rinsed with 1 mM acetic acid, and dried with Ar. For the gas phase silanization, the chips were placed in a desiccator containing a few drops of silane. The desiccators was sealed and heated above 100^{o}C. The chips were left to react for 1~2 h under a low pressure (approx. 1 mbar) in the silane vapor.

Table 4.3 Quantification of C, O, Si, and N from the overview spectra (main elements) in at% (normalized to 100), for two different surfaces silanized with different methods (left). Especially, the nitrogen bond was analyzed to compare the two methods (right).

	APTES(g)	APTES(l)
C	15.8	36.6
O	53.0	40.3
Si	28.7	18.0
N	2.5	5.1

compound	Silanization(g)	Silanization(l)
NH_3	399.1 / 0.18	399.2 / 0.18
$-NH_2$, N=N	400.1 / 0.70	400.1 / 0.71
$-(NH_4)$	402.1 / 0.12	401.7 / 0.11

The silanization steps lead to NH_2 groups on the surface, which was verified by the increase of nitrogen in the form of NH_2 (Table 4.3). More than 70% of the increase of nitrogen concentration was related to NH_2 groups (binding energy 400.1 eV). Increases in the C 1s (285.0 eV) and N 1s (400.1 eV) peak intensities confirmed the formation of a thin film composed of carbon, nitrogen, hydrogen and oxygen. For the relative amount of the different binding status of nitrogen, however, we did not observe a difference between the two-silanization processes. In addition, the thickness of the silane layer was measured by IE. The thickness of the APTES layers on the Si wafer was 20±2 Å (gas phase silanization) and 40±5 Å (liquid phase silanization), respectively. However, the distance between the Si atom and a proton of the amino group in a fully extended NH_2-silane molecule can be theoretically calculated to 7 Å. This implies that several layers of silane have been formed on the surface and that no monolayer of silane was obtained for both procedures. Taking the advantage of a rapid and thinner silane layer, silanization in gas phase was further used as standard silanization method in this work.

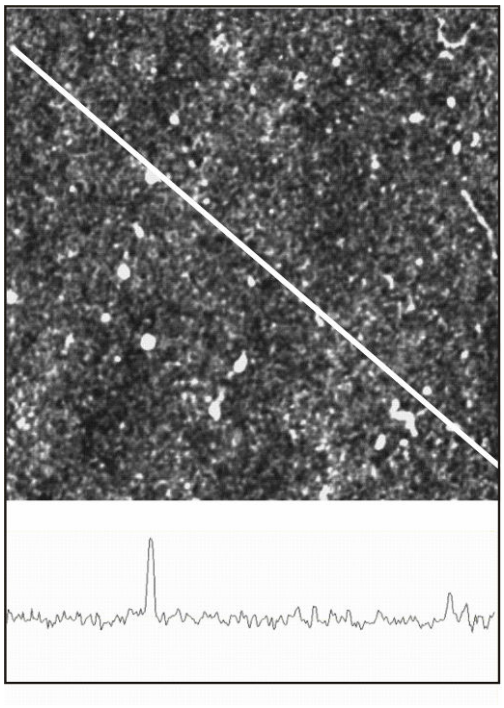

Fig 4.6 AFM image and cross section for the silanized surface in gas phase The z-axis displaying the height was scaled to 7nm for an image scale of 800nm×800nm.

From Fig 4.6, the silanized surface roughness was 0.40nm, which was much increased compared with that for silicon dioxide substrate (0.12nm Table 4.1). The silanization process left a thin and flat APTES silane layer for the further crosslinking reaction.

4.1.1.4 Crosslinking process after silanization

Cross-linking is the process of chemically joining two or more molecules by a covalent bond. With reaction-specific functional groups, crosslinker agents are useful for solid-phase immobilization, and other biomolecular reactions. Crosslinkers can be of either homobifunctional or heterobifunctional type. Commonly used homobifunctional crosslinkers and heterobifunctional crosslinkers are listed in the following

Homobifunctional crosslinker:

1. Glutaraldehyde

2. N-(γ-maleimidobutyryloxy)-succinimide ester (GMBS) (Breimer et al. 2003)

3. 4-(4-maleimidophenyl)butyric acid N-hydroxysuccinimide ester (SMPB) (Chrisey et al. 1996)

4. 3-bromopentanedione (Jal et al. 2004)

Heterobifunctional crosslinker:

1. Succinic anhydride

2. 4-(N-maleimidomethyl)cyclohexanecarboxylic acid N-hydroxysuccinimide ester (SMCC) (Cai et al. 2004)

3. 2,4-dichlorophenoxyacetic acid(2,4-D) (Jal et al. 2004)

4. N-(2-trifluoroethanesulfonatoethyl)-N-(methyl)-triethoxysilylpropyl-3-amine(NTMTA) (Kumar et al. 2004)

Homobifunctional crosslinkers have two identical reactive groups and often are used in one-step reaction procedures. In contrast to this heterobifunctional crosslinkers possess two different reactive groups that allow for sequential (two steps) conjugations. When choosing the appropriate crosslinker, the parameters of chemical specificity, spacer arm length, and water solubility are taken into account and more importantly, the selection is determined empirically.

Heterobifunctional crosslinkers have the advantage of providing better control than homobifunctional crosslinkers, because the reaction groups of the homobifunctional crossliners compete each other during the reaction with the underlying silane. In the present study, the homobifunctional crosslinker glutaraldehyde and heterobifunctional crosslinker succinic anhydride were compared. After the same activation and silanization process, either succinic anhydride (143 mM succinic anhydride, 87 % (V/V) 1-methyl-2-pyrrolidone and 13 % (V/V) sodium borate buffer) or 50% glutaraldehyde were applied for 2h at room temperature. After the reaction, the surface was rinsed with ultrapure water and dried with Ar. This reaction leads the formation of an amide group. After the crosslinking reaction, the same concentration of amino-terminated probe DNA labelled with Cy3 was offered to the surface. Finally, the DNA surface coverage was compared with fluorescence microscopy. For the glutaradehyde protocol, after rinsing with ultrapure water, no Cy3 signal was observed indicating an incomplete crosslinking step. However, for the surface crosslinked with succinic anhydride, the successful DNA immobilization process was confirmed. Furthermore, the successful crosslinking reaction with succinic anhydride was proven in FT-IR measurements.

Thick silane layers (approximately 112 nm measured by IE) on oxidized silicon control substrates were used for the characterization of the reaction between APTES and succinic anhydride. The FT-IR difference spectra of the sample after silanization and after crosslinking are shown in Fig 4.7.

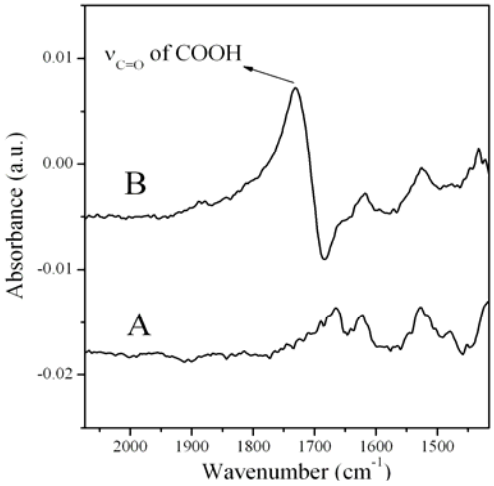

Fig 4.7 FT-IR difference spectra of the chips after silanization (A) and after further crosslinking (B). The reference spectrum was measured on the original substrate.

After the reaction of APTES and succinic anhydride, the FT-IR spectrum (Fig 4.7B) showed an absorption peak at 1729 cm^{-1}, which was absent in the spectrum after silanization (Fig 4.7A). This peak can be attributed to the C=O stretching modes of the

carboxyl group (-COOH) resulting from the ring-opening reaction of the anhydride molecules on the surface.

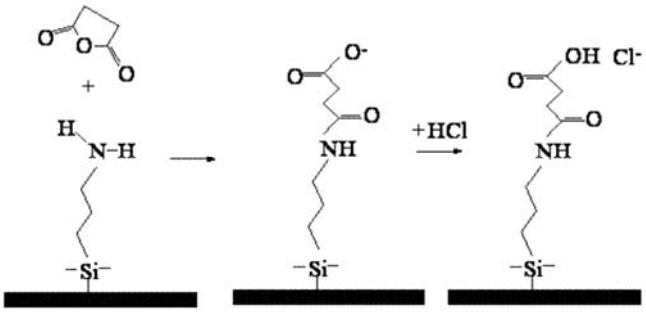

Fig 4.8 HCl protects the ending group of succinic anhydride after the reaction with silane

Since it is known that the $–COO^-$ group after crosslinking are unstable, the chips were rinsed with 0.1 mM HCl for seconds to neutralize the negative charge and to stabilize the groups. This procedure allowed for a transfer to the microspotter system, which then can be done in ambient air.

4.1.2 Covalent immobilization of oligonucleotides at the modified biosensor surface

The formation of amino binding is generally used to immobilize biomolecules on the functionalized surface due to its firm interaction (Lahiri et al. 1999; Mrksich et al. 1995; Sigal et al. 1996). Amino modified probe DNA (Fig 4.9) was immobilized on the carboxyl group after crosslinking. The structure of the immobilization process is shown in Fig 4.10.

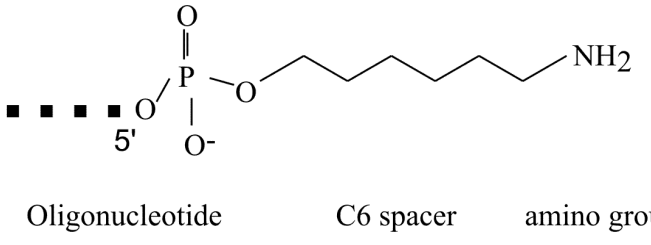

Fig 4.9 The structure of the ssDNA probe molecules is composed of oligonucleotide, C6 spacer and modified amino group. The amino group and C6 spacer are called MMT in the sequence appreviation.

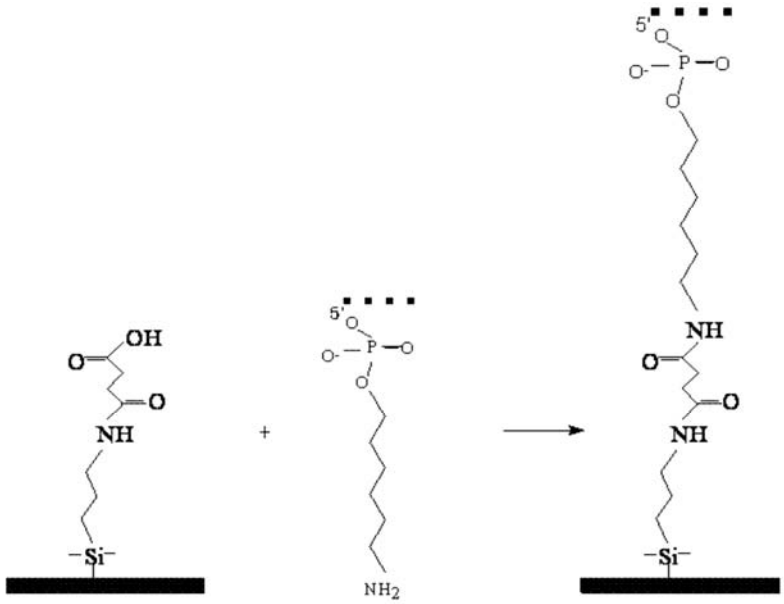

Fig 4.10 Scheme for the covalent attachment of amino-modified DNA onto the biosensor surface

The probe ssDNA was spotted onto the surface with the aligned microspotting (paragrah 3.2.7). 3μM DNA oligonucleotides 5'MMT-ATGAACACTGCATGTAGTCA-3' were dissolved in MES buffer (0.1 M MES, 0.5 M NaCl and 10 mg/ml EDC as condensing agent, pH 7.0). The immobilization process was achieved by incubation (37^{o}C) overnight, followed by a rinsing step with ultrapure water. The covalent bond was thus formed between the -NH_2 group of the probe DNA and the -COOH functional group from the succinic anhydride (Fig 4.10).

The attachment of probe DNA was confirmed by imaging ellipsometry and fluorescence microscopy (Fig 4.11).

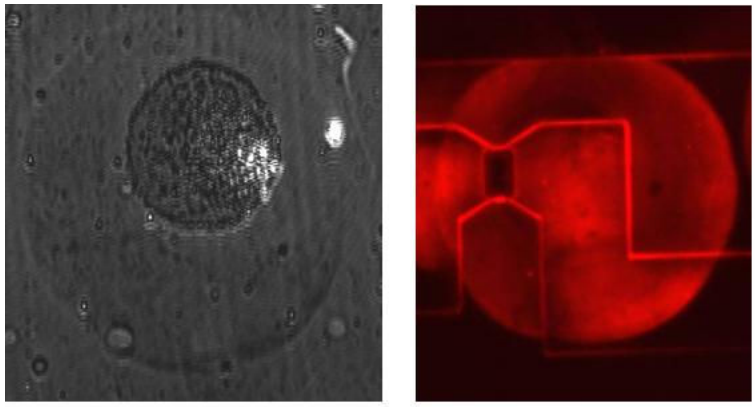

Fig 4.11 Ellipsometry image (left) of ssDNA immobilized on modified surface and fluorescence image (right) of the Cy3-ssDNA immobilization on the modified FET gate

In Fig 4.11, the ellipsometry and fluorescence images for the attached probe DNA on the control substrate and the ISFET chip gate are shown. Clear droplet appearance and fluorescence of the Cy3 dye confirmed the attachment of the probe DNA. The covalent binding of the probe DNA immobilization process was proven by N1s XPS spectra. During the covalent immobilization, the amino group of the probe DNA formed an amide bond (-CONH-) with the carboxyl group of the surface, resulting in a change of the chemical status of nitrogen.

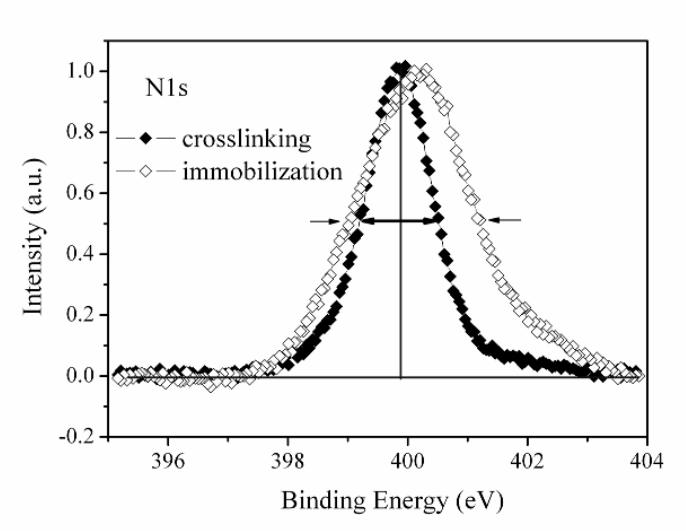

Fig 4.12 High resolution N1s XPS spectra on the surfaces after crosslinking and immobilization of probe ssDNA

In the spectrum of N1s (Fig 4.12), for the crosslinking surface, a peak at 399.8 eV was observed, with a full width at half maximum (FWHM) of 0.69 eV. The peak was attributed to an amide (-NH-) group. After the immobilization process, the position for the peak shifted to 400.2 eV, and the FWHM doubled (1.14 eV). The intensity of the N1s peak corresponds to the amount of nitrogen indicating the amount of DNA molecules adsorbed on the modified surface. The peak area for DNA immobilization was about 1.7 times larger than that of the crosslinking surface. This increase suggested an efficient immobilization reaction of probe DNA on the crosslinking surface. The reactive area and the immobilization of amino modified probe DNA is limited, since the size of the DNA molecules was large compared with that of the -COOH functional group (Ito et al. 2006). A higher density and a better-ordered structure of the crosslinker will offer a better platform for the immobilization process. Therefore, DNA immobilization was not only dependent on the -COOH density but also on the packing mode. The efficient immobilization process in our protocol was further proven by the following hybridization reactions.

4.1.3 Hybridization of oligonucleotides at the biosensor surface

In the DNA-DNA hybridization, the probe ssDNA reacts with its complementary strand forming the double helix, which in general offers a specific way to perform the gene identification. The hybridization in solution largely depends on the solution environment such as ionic strength, pH, temperature and type of solvents. In this part, the in-situ hybridization on solid support was investigated to compare the influence of these parameters between two formats of hybridization, in the free solution and on the solid support. The hybridization efficiency was analyzed by means of fluorescence microscopy in this paragraph.

4.1.3.1 The effect of salt concentration on the stability of the DNA duplex

To confirm the precise spotting and the successful hybridization reaction at the chip surface, fluorescently labeled target DNA was used. Several kinds of probe DNA: perfect match (PM), 1mismatch (1MM), 2mismatch (2MM), 3mismatch (3MM) sequences were spotted onto a control substrate to realize a multi-probe assay.

Table 4.4 DNA sequences used in this work are abbreviated by PM, 1MM, 2MM, 3MM, and FMM. These probes were covalently attached to the different transistor gates via silanization, crosslinking and microspotting. The covalent attachment was achieved via a C6 amino modifier (MMT) attached to the 5' end of the catcher DNA samples. The target DNA was labeled by Cy3 to detect the hybridization reaction.

Name	Sequence
Fluorescence target DNA	5'-Cy3-TGACTACATGCAGTGTTCAT-3'
PM	5'MMT-ATGAACACTGCATGTAGTCA-3'
1 MM	5'MMT-ATGAACACTAACATGTAGTCA-3'
2 MM	5'MMT-ATGAATACTGCATGTTGTCA-3'
3 MM	5'MMT-ATGAATACTAACATCTAGTCA-3'
FMM	5'MMT-TACTTGTGATGTACATCAGT-3'

In Table 4.4, the position of the mismatches inside the sequences is signed with black circles. The hybridization process occurs when two ssDNA react to form the dsDNA. By heating or chemical denaturantion, the dsDNA separates, which is called dehybridization.

The stability of the duplex is related to the base composition, i.e. the nucleotide sequence (Breslauer et al. 1986). When selecting the positions of the mismatches, the balance of the positions is taken into account to avoid the formation of GT wobble pairs. For 1MM probe DNA, the mismatch nucleotide was located in the middle of the sequence. For 2MM, two mismatches were chosen at the two third positions. The three mismatches were averagely distributed in the 3MM sequence.

Following immobilization, a rinsing step with ultrapure water was applied. Then the hybridizations were performed in different buffer solutions, including SSC buffer, TE buffer (10mM Tris, 1mM EDTA with various concentration of NaCl, pH≈8.0) and NaCl solutions of different concentrations (0.01, 0.1, 1, 10 and 100 mM).

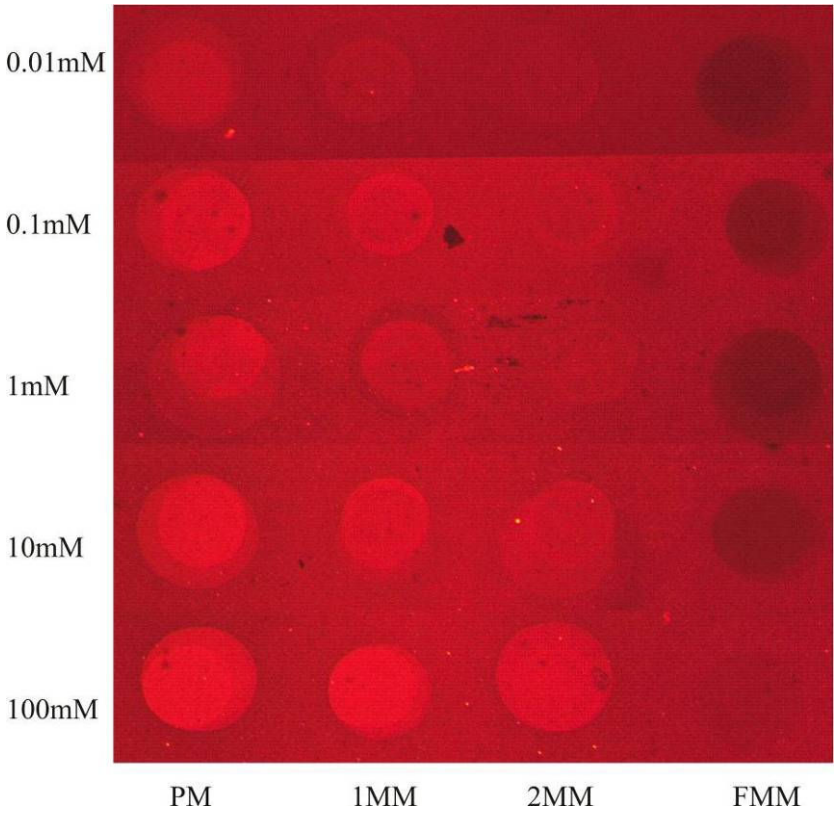

Fig 4.13 Fluorescence microscopy images of hybridization in different NaCl solutions (0.01mM, 0.1mM, 1mM, 10mM, 100mM) for different types of probe DNA (PM, 1MM, 2MM, FMM) with Cy3-labelled target DNA

The hybridization was observed by fluorescence microscopy. The fluorescence images were analyzed with the program ImageJ (paragraph 3.2.5). The hybridizations were carried out for two hours at room temperature. In order to avoid unspecific binding, a blocking step (2 h) with 1% Bovine Serum Albumin (BSA) in Phosphate Buffered Saline Buffer

(PBS) was used before the hybridization. After the hybridization, the samples were carefully rinsed in three steps (2×SSC, 0.1×SSC and ultrapure water). In general, it is known for ex-situ assays that a careful rinsing step is necessary to wash off the unspecific bound DNA and to provide a high selectivity for the SNP detection.

To compare the results for these microarrays, the hybridizations were performed on the same control substrate to guarantee an identical surface modification. For all the fluorescence images, the same exposure time (4.71s) and z-position were used to enable a comparison. No further digital image processing was applied. The signals from the same area for all the spots were analyzed with ImageJ, which offered the mean brightness value of the pixels.

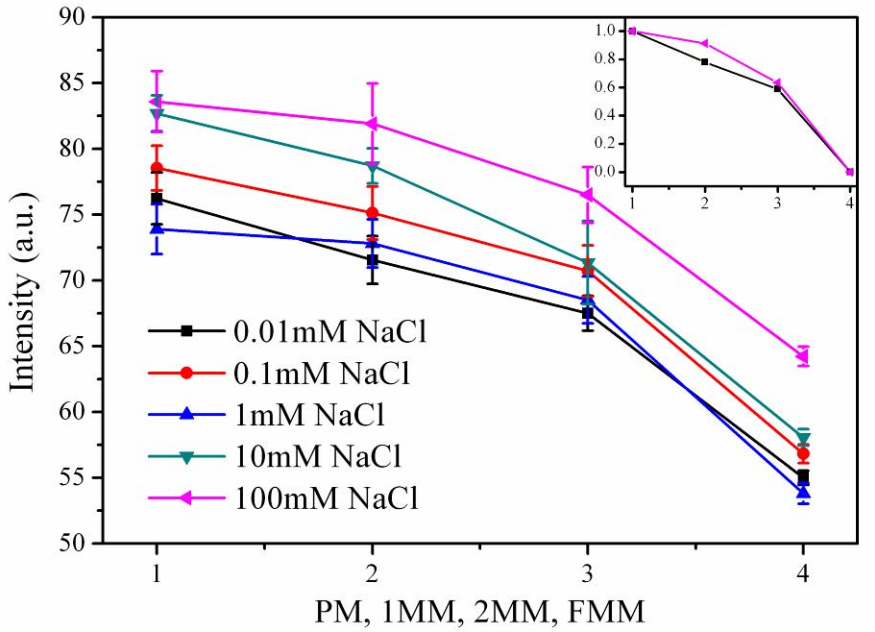

Fig 4.14 Mean values of the fluorescence intensity for the PM, 1MM, 2MM and FMM hybridization with 1µM target DNA in different concentrations of NaCl. The signals from n=20 spots per data point are summarized as average value±standard deviation. The small inset shows the baseline corrected and normalized curves for 0.01mM NaCl and 100mM NaCl.

For all the NaCl solutions, the mean intensity values increased for hybridization of different probe DNA from 1MM, 2MM to PM and reached the highest value for the hybridization with the PM probe in 100mM NaCl (Fig 4.14). At the same time, the intensity for the FMM hybridization increased with the increase of the NaCl concentration indicating that the unspecific hybridization was affected by the ionic strength accordingly. Concerning the ability to distinguish between PM and 1MM hybridization, lower ionic

strength solution revealed better results. In the inset of Fig 4.14, the hybridization signals for PM, 1MM, 2MM, and FMM for 0.01mM and 100mM NaCl solutions are shown. With increasing ionic strength, the difference between PM and 1MM hybridization (SNP detection) signals decreased. After baseline correction and normalization, the singles for the 1MM hybridization in 0.01mM NaCl was 78.0% of the PM hybridization, whereas for the 100 mM NaCl solution, the signal was still 91.3% of the PM signal. The differentiation of the 1MM hybridization from the PM hybridization is important for a reliable SNP detection. As a result, the lower ionic strength of the buffer solutions provided a higher selectivity for the SNP detection.

For the DNA-DNA hybridization in free solutions, the target DNA molecules behave more like PEs, interacting strongly with their counterions. There are two mechanisms to explain the binding of counterions to PE, which can be also applied to DNA. On the one hand, the large electrostatic potential near the polyion surface will attract many counterions through a non-specific interaction. On the other hand, the counterion is able to a more intimate association with the charged site on the polymer (Felsenfe et al. 1967). Therefore, the hybridization process in solutions strongly depends on the ionic strength. On an average, 0.5-0.6 sodium ions binds to the DNA per phosphate group (Creeth et al. 1949; Huizenga et al. 1950). With increasing NaCl concentration, more Na^+ ions adsorb on the phosphate backbone and reduce the electrostatic repulsion between the two strands of the duplex. Therefore, the stability of the double helix increases with increasing counterion concentration. Theoretical calculations indicated that a 0.01-0.012 mM NaCl coucentration is enough for the hybridization process of 20 b.p. DNA to compensate for the negative charge of the phosphate backbone of the ssDNA molecule. The in-situ hybridization on the solid support carried out in this experiment showed a similar influence of the ionic strength compared to the free solutions. More efficient hybridizations were obtained in higher ionic strength solutions due to the stability increase of the duplex with the absorption of Na^+ ions. However, a better selectivity for SNP detection was achieved in the lower ionic strength solutions.

4.1.3.2 Influence of the type of buffer solution on the hybridization efficiency

Besides the effect of salt ions, the hybridization process might also be influenced by the choice of the hybridization solvents (SSC or TE buffer). Two extremely different buffer solutions were utilized to compare the DNA hybridization process:

1. 4×SSC buffer solution (60mM sodium citrate, 600mM sodium chloride pH =7.0)

2. TE buffer (10mM Tris, 1mM EDTA pH=8.0)

with citrate and EDTA as chelating agents. EDTA is referred to ethylenediaminetetraacetic acid disodium salt dehydration, and Tris stands for tris (hydroxymethyl) aminomethane. The full chemical structures are provided in the appendix. The SSC buffer solution is one of the standard DNA-DNA hybridization buffer solutions, while TE buffer is the commonly used buffer solution for ISFET detection assays.

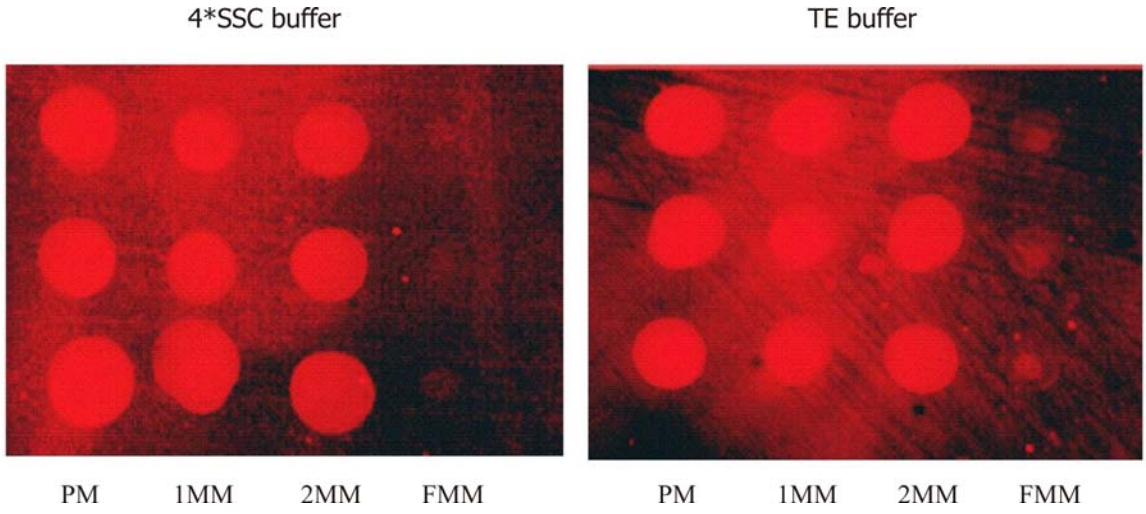

Fig 4.15 Fluorescence Microscopy images of a 3μM target DNA hybridization in different buffer solution 4×SSC (left) and TE buffer (right)

In Fig 4.15, the fluorescence microscopy images of the hybridization of target DNA with the different probe DNA sequences in dependence of different types of buffer solutions are shown. The intensities were extracted and depicted in Fig 4.16.

The ionic strengths of the two solutions were estimated to 660mM and 5mM for the SSC and the TE buffer, respectively. A similar tendency was observed compared to the hybridization in different concentrations of NaCl (Fig 4.14). For the same ionic strength solutions, PM hybridizations achieved the highest intensities among all the hybridization processes. For the same probe DNA hybridization, higher ionic strength buffer solution offered a higher efficient hybridization. The intensity value for the PM probe in the SSC buffer solution was 1.27 times more compared to the TE buffer solution. The intensity percentages of 1MM/PM were 97.7% and 65.5% for the SSC buffer and TE buffer solutions, respectively (inset in Fig 4.16).

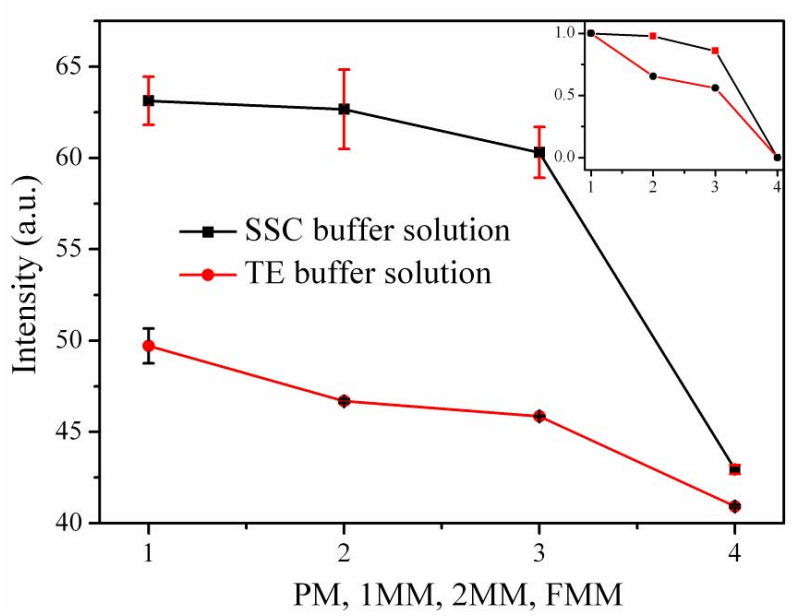

Fig 4.16 Mean value of the fluorescence intensity obtained by the hybridization process in SSC and TE buffer for the PM, 1MM, 2MM and FMM hybridization. In the inset, two curves for hybridization in two buffer solution were baseline shifted and normalized to aid a better comparison.

Although two hybridization buffer solutions were prepared in different pH, however, from pH 5-9, the rate and efficiency of hybridization is fairly independent of pH (2006i). When comparing the ionic strength of the two buffer solutions with the NaCl solution results, it can be seen that in the higher ionic strength SSC buffer solution, the 1MM/PM percentage was even higher (97.7% to 91.3%). In the TE buffer solution, which has a similar ionic strength with the 5mM NaCl solution, a even lower 1MM/PM ratio compared to the 0.01mM NaCl solution was obtained (65.5% to 78%). Besides the influence of the ionic strength on the DNA-DNA hybridization efficiency, the type of buffer solution also plays an important role.

In both buffer solutions, the chelating agents (EDTA or sodium citrate) reduce electrostatic interactions between the bases and between the base and the solvent. It also enlarges the cavity in order to accommodate the coil form (Felsenfe et al. 1967). The efficiency of this effect is mainly related to the size of chelating agents, comparing the size of EDTA and citrate, EDTA needed more energy to enter into the DNA helix structure. Therefore, in addition to the ionic strength effect in the SSC buffer solution with citrate, a higher efficiency of the hybridization can be obtained. However, the TE buffer offered a bigger selectivity than the SSC buffer to distinguish between the hybridization of PM and 1MM.

As a further test, the adaptation of this assay to the fully encapsulated ISFET chips was done and a similar efficiency of hybridization was achieved. The fluorescence images are shown in Fig 4.17 and the image analysis is provided in Fig 4.18.

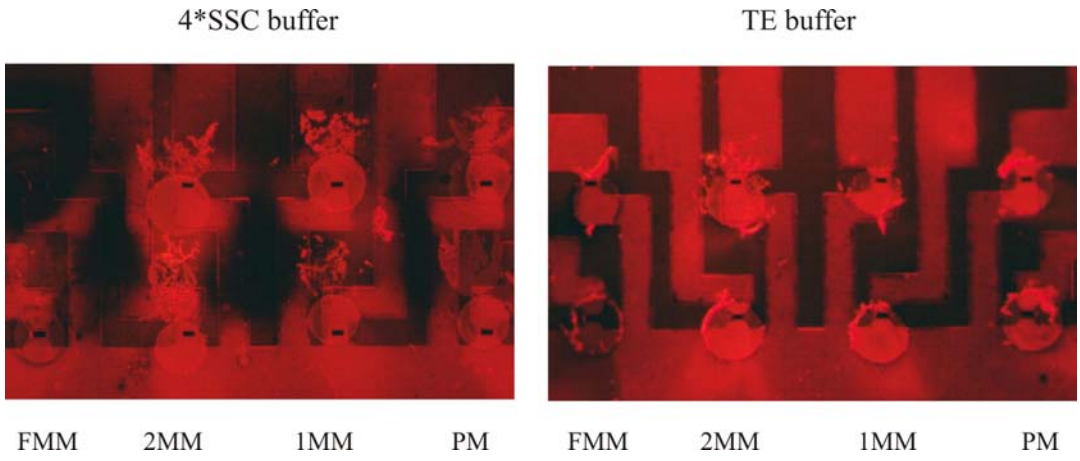

Fig 4.17 Fluorescence images of the hybridization reaction of FMM, 2MM, 1MM to PM in TE and SSC buffer solutions

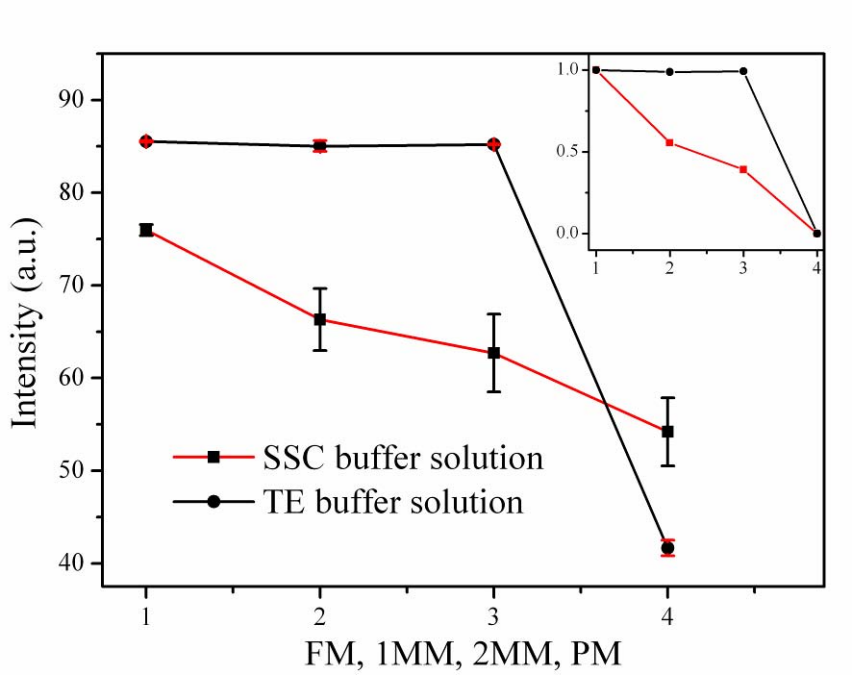

Fig 4.18 Mean value of the fluorescence intensities obtained by the hybridization process in SSC and TE buffer for PM, 1MM, 2MM, and FMM, respectively, on the modified ISFET sensors surfaces. The normalized results are provided in the inset.

The intensities for the different hybridization processes for PM, 1MM, 2MM and FMM respectively are shown in Fig 4.18. The results on the modified gate surface are similar

with these on the test substrates (Fig 4.16). The coincident results confirmed the more efficient hybridization in the SSC buffer solution but a higher selectivity for SNP detection in the TE buffers solution. Consequently, the TE buffer solution was used as hybridization buffer for the electronic SNP detection experiments in paragraph 4.3. From the results presented so far, a maximum of 70% selectivity for the 1MM/PM ratio can also be expected for the electronic assays.

4.1.3.3 Sandwich hybridization assay at the modified surfaces

As it is used in many highly selective bioassays reported in literature, a sandwich hybridization assay was used apart from the normal hybridization process. In the sandwich hybridization process illustrated in the schematics of Fig 4.19, firstly PM probe DNA was immobilized. The sequence of 50 bases target DNA (concentration 3μM) with 10T as a spacer was then introduced to hybridize with the PM probe sequence. In a second hybridization step, a 20 bases target DNA (concentration 3μM), which was labeled with the Cy3 dye at its 3′ end was hybridized with the upper part of the first target to form a so-called sandwich structure. The sequences for this assay are provided in Table 4.5. Three buffer solutions were utilized, 4×SSC with 600mM NaCl, TE buffer with 500mM NaCl and TE buffer with 250mM NaCl.

Table 4.5 DNA sequences used for the sandwich hybridization process. The 2nd target DNA was labeled with Cy3 at its 3′ end.

Name	Sequence
Probe DNA	5'MMT-ATGAACACTGCATGTAGTCA-3'
1st target DNA	5'-TGCTAGTGACGTACACTCGATTTTTTTTTT TGACTACATGCAGTGTTCAT-3'
2nd target DNA	5'- TCGAGTACGTCACTAGCA-Cy3-3'

The mean values for the sandwich hybridization process in the different buffer solutions were extracted from the fluorescence images in Fig 4.19 and are shown in Table 4.6.

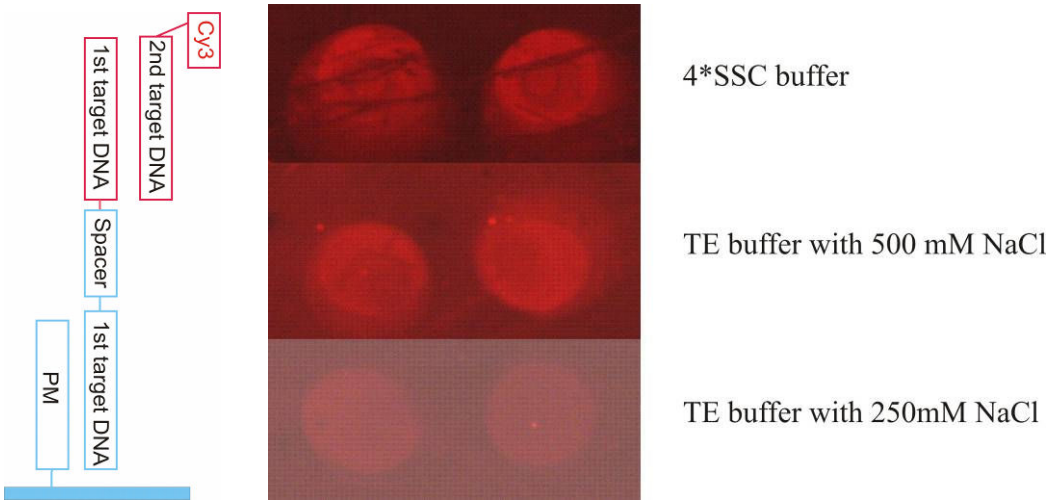

Fig 4.19 Fluorescence images of the second hybridization in the sandwich hybridization process carried out in different buffer solutions 4×SSC.

Table 4.6 Comparison of fluorescence intensities for the sandwich hybridization in three different buffer solutions

Buffer solution	Mean value for fluorescence (n=16)
4×SSC with 600mM NaCl	50.0±2.2
TE with 500 mM NaCl	55.2±3.8
TE with 250mM NaCl	28.6±2.0

From the results in Table 4.6 it can be seen that there was no significant difference between the mean fluorescence values for 4×SSC and TE buffer with 500mM NaCl. Furthermore, in the same type of buffer solution (TE), with decreased NaCl concentration the hybridization efficiency was also reduced to about 50% corresponding to the reduction rate of the NaCl concentration. This reduction is bigger compared to the hybridization efficiency in TE with 0mM NaCl to SSC with 600 mM NaCl for the direct hybridization (Fig 4.16). This demonstrated that in the sandwich hybridization process, a higher ionic strength of the hybridization buffer is necessary. The second hybridization process in the sandwich array should therefore be more dependent on the ionic strength than on the type of the hybridization buffer solution. As a result, the sandwich hybridization process can be treated similar to the hybridization process in free solutions. However, the hybridization process on a solid supports is different and needs to be optimized from assay to assy.

4.1.4 Biotin/streptavidin binding at the modified biosensor surface

The biotin/streptavidin binding system is used in many biotechnological applications such as affinity separations, diagnostic assays, “tagging” of molecules, imaging, or delivery of therapeutics (Perez-Luna et al. 1999). The binding is well studied on the solid support to provide details of the sensing principles. To realize the binding for our assays, firstly EZ-link Sulfo-NHS-biotin was exploited to bind covalently on the test substrates.

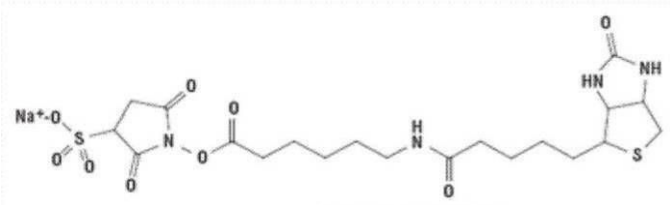

Fig 4.20 Structure of the EZ-link Sulfo-NHS-biotin. The biotin probe molecule was modified with N-hydroxysulfosuccinimide (sulfo-NHS). The spacer length is increased by adding hexanote between the NHS (left) and the biotin (right) (Pierce USA)

As shown in Fig 4.20, biotin bound to N-hydroxysulfosuccinimide (Sulfo-NHS) esters are one of the most popular types of biotinylation reagents.

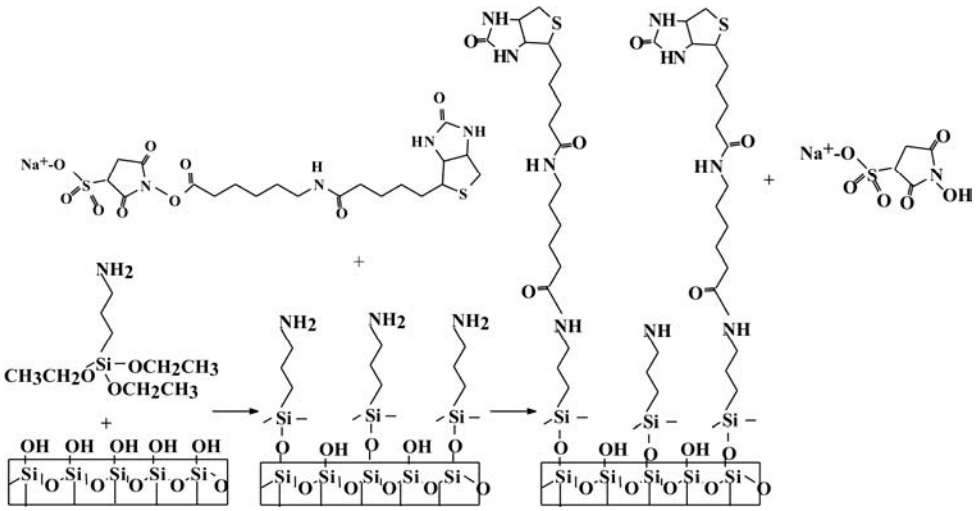

Fig 4.21 Schematics for the reaction of EZ-link sulfo-NHS-LC-Biotin with the amino-silanized surface. Upon formation of an amide, the sulfo-NHS group is stripped. The procedure results in a covalent linkage of the biotin probe molecules to the surface.

NHS-activated biotins react efficiently with primary amine groups (-NH_2) in pH 7-9 buffers to form stable amide bonds. In 10mM boric acid (pH=8.04), 0.5mg/ml biotin reacted with the NH_2 group from the APTES on the surface (Fig 4.21). The biotin reacted

with APTES via formation of an amide bond. The reaction of streptavidin and biotin was performed with 1mg/ml streptavidin in ultrapure water for 1 hour.

Ellipsometry images confirmed the formation of the biotin layer formed on the APTES-silanized surface and the thickness of the layer was measured. AFM analysis displayed the roughness of the biotin surface (Fig 4.22).

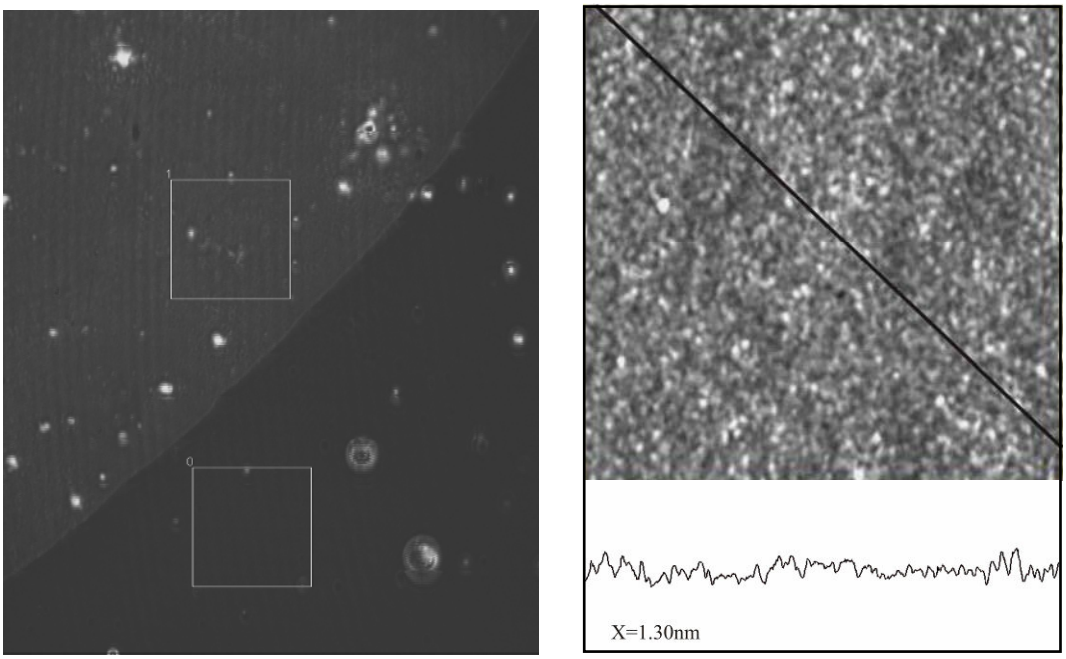

Fig 4.22 Ellipsometry image for the immobilization of a 0.5 mg/ml EZ-link sulfo-NHS-LC-biotin spot on the APTES-silanized surface. The upper area is referred to the area with biotin, the lower area without biotin. The AFM image on the right side shows an area of 1µm×1µm. The section graph is scaled with a z axis of 4.7 nm

The formation of the biotin layer on the APTES-silanized surface caused a 5 nm increase of the thickness. In the AFM image, the extracted R_q roughness value after the immobilization of biotin was 0.43 nm, which was similarly compared to that after the silanization step (Fig 4.6). Consequently, the biotin immobilization process did not change the roughness of the surface, and resulted in a smooth and flat surface for the further reaction with streptavidin. The smooth surface indicates an orderly packed biotin layer on the surface.

The biotin/streptavidin binding was analyzed with XPS, which provided direct evidence for the binding of biotin and the following biotin/streptavidin binding on the solid supports. The XPS results are summarized in Table 4.7 for the three samples surfaces, after

silanization, after biotin immobilization and after the biotin/streptavidin reaction. The relative amount of the elements C, O, Si, and N were analyzed.

Table 4.7 The quantification of the different compounds for the three sample surfaces after silanization, after biotin immobilization and after the biotin/streptavidin reaction with biotin.

	silanization	biotin immobilization	biotin/streptavidin binding
C	37.3	57.2	60.3
O	40.8	26.6	24.4
Si	17.0	13.3	7.4
N	4.9	2.9	8.0

In Table 4.7 the detailed spectra analysis is summarized. The binding energies and element contents were fitted with the software UNIFIT. After the biotin immobilization on the silanized surface, the content of carbon increased significantly. The other element contents decreased, because the optical penetration depth of the XPS source laser fell mainly in the biotin layer. After the biotin/streptavidin binding, the percentages of C and N increased since proteins have a larger amount of these two elements.

Table 4.8 Binding energies related to the binding energy of 285.0 eV of the CH_2 contamination. The quantification of the C and N for the three sample surfaces after silanization, after biotin immobilization and after the streptavidin reaction with biotin are summarized. The datas are shown in the form of binding energy (eV)/quantification (%).

	compound	silanization	biotion immobilization	biotin/streptavidin binding
C	CH_2	285.0 / 11.1	285.0 / 39.9	285.0 / 31.3
	COH/COC/C=O	286.7 / 15.0	286.2 / 11.8	286.5 / 20.1
	COOH	-	288.8 / 3.9	288.3 / 5.6
	CO_3^{2-}	289.4 / 2.4	-	289.5 / 1.7
N	NH_3	398.8 / 0.4	-	-
	$-NH_2$/NH	399.9 / 2.3	400.0 / 3.1	400.2 / 8.2
	$-(NH_4)$, N-O	401.8 / 0.3	-	-

In Table 4.8, the specific binding energies and quantifications for C and N are shown for the three different samples. Through the biotin immobilization, the dominant carbon format

was changing from C=O (286.7 eV) to CH_2 (285.0 eV). The CH_2 qualification increased 3.6 times due to the introduction of alkyl groups of the biotin. A similar increase of nitrogen can also be seen in the format of NH at 399.9 eV. The increase of the CH_2 and NH signals indicated the covalent reaction of biotin with the silane surface.

After the affinity reaction of biotin with streptavidin, the nitrogen in the form NH_2/NH further increased by 2.7 times, because of the introduction of a high amount of amino acids compared to the biotin layer. The energy band slightly shifted to a higher binding energy (400.0-400.2 eV), indicating a slight protonation of the –NH- groups. For the carbon signal, although the main attribution was still maintained at 285.0 eV for the groups CH_2, the two binding energies at 286.5 and 288.3 increased significantly and new binding energy at 289.5 eV occured. Since the streptavidin molecule has no carbohydrate group, there was no additional charge in the CH_2 signal, but in three other chemical environments of carbon. Three energy binding sites are attributed to three different carbon formats in the protein. This is a clear indication, that streptavidin reacted with the biotin modified surface.

In summary, our step-by-step optimized methods for the surface modification protocols and the covalent binding of the probe biomolecules clearly indicated the possible application to our encapsulated biosensor devices. The gate SiO_2 material of the ISFET biosensors was successfully modified to covalent binding of probe biomolecules. A series of reactions starting from cleaning/activation, silanization, crosslinking, and immobilization of ssDNA or biotin was successfully established. All protocols were successfully transferred to the fully encapsulated ISFET devices and were “mild” enough for our encapsulation materials. The optimization formed the basis for the further detection of the DNA hybridization and biotin-streptavidin reactions in the electronic assays. In our bioassays, the DNA-DNA hybridization reaction and the streptavidin binding reactions were detected with the FET biosensors in the terms of change in surface potential or input impedance of the devices.

4.2 Polyelectrolytes as model system for the electronic detection with ISFET devices

As a model system, the multilayer adsorption of oppositely charged polyelectrolytes was monitored by the ISFET devices in both potentiometric and impedimetric readout. The signals, which are recorded by the ISFET, are caused by a change of the surface potential during adsorption or a change of the input impedance of the gate electrodes. The accumulation of charges at the gate oxide causes a shift in the flatband voltage of the transistor, which results in a voltage drop of the output signal in a time-dependent potentiometric measurement. As a model for a better understanding of the adsorption and interaction of DNA and other charged biomolecules at the biosensor surface, polyelectrolyte multilayer (PEMs) can be studied. Polyelectrolytes are linear macromolecular chains bearing a large number of charged or chargeable groups, when dissolved in a suitable polar solvent, generally water. Each alternating adsorption step of these charged macromolecules leads to a charge inversion of the surface (charge

over-compensation effect) (Decher et al. 1998). Fig 4.23 depicts the strong electrostatic forces, which are acting to stabilize the polyelectrolyte multilayer on the gate surface.

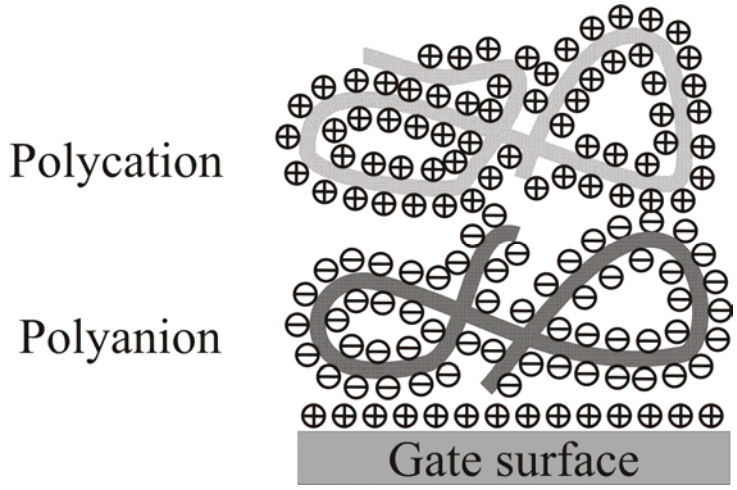

Fig 4.23 Schematics of the alternating multilayer of polyelectrolyte adsorption on the gate surface of the FETs. The multilayer is stabilized by strong electrostatic forces. A charge-over compensation effect by counterion condensation is responsible for the remaining net charge at the interface between the top PE layer and the electrolyte solution.

4.2.1 Alternating adsorption of charged polyelectrolyte multilayers (PEMs) on different surfaces

Three commonly used PEs, Poly (allylamine hydrochloride) (PAH), Polyethylenimine (PEI) and Poly (styrene sulfonic acid) (PSS) were paired in PSS/PEI and PSS/PAH for the purpose of the present study. Structures, full/short names and molecule weight (g/mole) of three PE used in this part are shown in the appendix. PSS is a strong PE, and PAH is weak PE, which disassociated in the pH 6-8 solution. PEI is a strong polyelectrolyte at low pH and behaves like a neutral polymer at high pH (Penfold et al. 2003). In the range of pH 6-8, PAH and PEI are positively charged, and PSS is negatively charged. PEMs attachment on the gate surface was stabilized by electrostatic forces between the polycation PAH/PEI and the polyanion PSS.

The primary parameter for the buildup of PEMs is its structure. The PEMs structures are affected by internal composition, i.e. the polyanion/polycation stoichiometry, salt content of the deposition solutions, the polyion concentration, the charge density of the polyions (either varied by charge dilution in copolymers or as a result of the pH in weak polyion

solutions), the polyion rigidity and the molecular weight, and the presence or absence of counterions in the layer (Schonhoff 2003b). External environments, such as pH and temperature also play an important role in the building up of PEMs. Normally, the PEMs structures are monitored as a change of thickness.

4.2.1.1 PEMs adsorption on the bare SiO_2 surface

Firstly, the thickness of adsorption of PEMs (PSS/PAH) on a bare SiO_2 substrate was investigated. The parameters of pH value, temperature and conductivity of all the PEs and buffer solutions were adjusted the same to avoid the side effects. PMEs were assembled by consecutively adsorption of PAH and PSS from the PE solutions (Decher et al. 1998; Schonhoff 2003a). PEs (50μM) were diluted in 0.1 M NaCl solution and the pH values for the PSS and PAH solutions were adjusted to 5.94. After the wet cleaning and activation (MeOH/HCl 30 minutes) of the substrate surface, the precursor layer of PEI in NaCl (pH=7.0) was adsorbed on the bare solid support, and then the $(PSS/PAH)_n$ PEMs were formed on it. After adsorption of each PE layer for 20 minutes, the substrate was rinsed with the buffer solution thoroughly and dried with Ar. For a first characterization, the adsorption of 10 layers PEMs on the bare solid support was monitored. The thickness increase was measured with ellipsometry and the roughness values of the surfaces were obtained from AFM measurements.

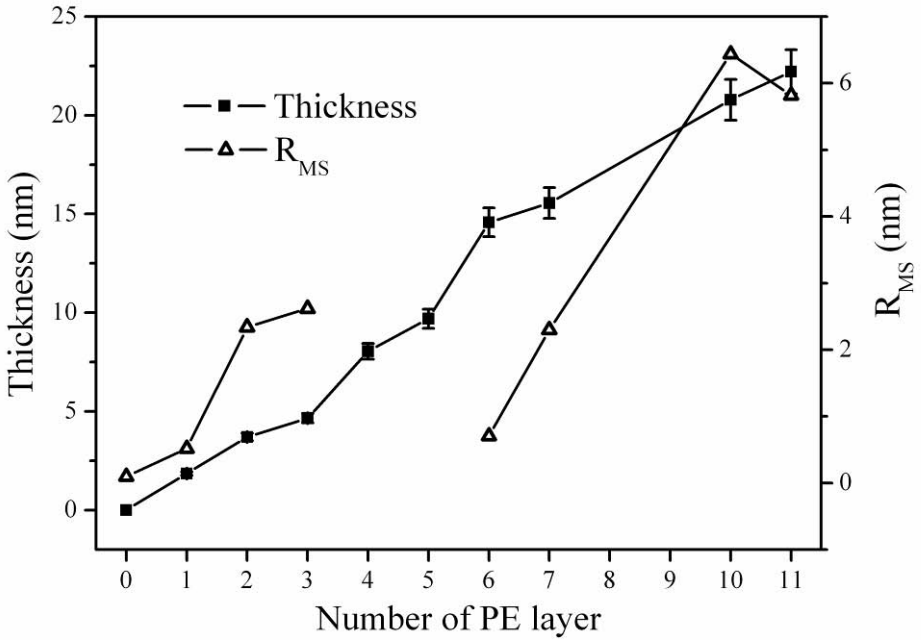

Fig 4.24 Thickness and roughness of the PEMs

Employing 0.1 M NaCl as buffer solution was to achieve a higher amount of adsorbed molecules as well as to prevent possible effects of ion-concentration and electrolyte-conductivity changes. The thickness of the total PEMs consisting of the PEI layer and PSS/PAH five double layers was ~23nm, i.e. approximately 2nm/per layer. The thickness increased linearly with the adsorption of PEs, which is in agreement with the previously reported results (Bosio et al. 2004). The surface of the bare SiO_2 and the adsorbed PEI precursor layer were smooth with average R_{ms} values of approximately 0.2nm and 0.6nm, respectively. The PEI layer was homogeneous and assumed as a flat conformation of the PEI molecules. The roughness was strongly increased after the adsorption of the second PSS layer (R_{ms}=2.4nm) and increased up to the value of R_{ms}=6nm after the adsorption of the (PSS/PEI) 5 double layers.

4.2.1.2 PEMs adsorption on the silanized surface

On the APTES or GPTES silanized surface, the thickness of PEMs was also measured. TE buffer (10mM Tris, 1mM EDTA, 0.1mM NaCl) was used as buffer solution and the pH for the PEs and TE buffer were adjusted to 7.03. For the bare SiO_2 surface, the point of zero charge (PZC) is 2.0 (Bousse 1982). After the silanization process with APTES, the electrokinetics are changed drastically, and the PZC shifts from 2 to 9.0 (Takafuji et al. 2004). Aliphatic amino groups have a dissociation constant (pK) of approximately of 10.6, although the close packing of the aliphatic amino groups on the surface decreases this pK, the surface will still be positively charged at neutral pH (Bezanilla et al. 1995). In the mean time, the pH sensitivity of the FET sensors is also changed from 34±2 mV/pH for the SiO_2 gate oxide to 52.4±4.2mV/pH for the silanized surface (Uslu et al. 2004). The pH of the buffer should be lower than the isoelectric point (IEP) of the first adsorption PE solution, because free amino groups from APTES will become positively charged at a relatively low pH. If sufficient free amino groups are located on the outside surface of the SiO_2, in this way negatively charge PE will bind to the APTES at the surface. For the GPTES-silanized surface, the epoxy group is highly reactive only at high pH, so the positive charges on the GPTES-silanized surface were much less compared to those on the APTES-silanized surface at pH 7.03 solutions. The thickness of adsorption of PAH and PSS on APTES/GPTES modified surface is shown in Table 4.9.

Table 4.9 Thickness of PEMs on silanized surface with APTES and GPTES measured by Ellipsometry

thickness (nm)	APTES	GPTES
5 layers	4.70nm	18.58nm
10 layers	21.87nm	39.10nm
10layers-5layers	17.17nm	20.52nm

The driving forces for the formation of PEMs are the coulomb interactions between the oppositely charged PEs and between the first layer of PSS and the solid silanized surface. The surface charge could affect the packing of PE, i.e. the structure of PEMs. In our experiment, the thickness increase was not linearly with the numbers of PE layers on the APTES-silanized surface. The thickness for 10 layers (5 double layers) PEMs was almost 4 times larger than 5 layers (2.5 double layers). In contrast to this, the thickness for 10 layers on the GPTES-silanized surface was almost twice the thickness for the five layers. The linear growth of PEMs thickness on the GPTES modified surface, suggested similar adsorption properties for the first and second five layers. The thickness of each PE layer was approximately 4nm, which is twice so large compared to the adsorption on the bare SiO_2 at pH 5.94 of the buffer solutions. A large dependency of PE layer thickness with different pH of the buffer solutions was already reported (Shiratori et al. 2000).

The thickness of the second five layers on the APTES-silanized surface was comparable with the thickness on the GPTES modified surface. The similar thickness for each monolayer means that the structure and the coiling state for both starting surfaces were the same. However, for the first five layers on the APTES-modified surface, the thickness for each layer was just 0.94nm. As an interpretation, the adsorption of the first five layers is strongly affected by the starting surface. Once a certain thickness for the PEMs is reached, the further growth is only affected by the conditions of composition of PE solutions, pH and temperature.

4.2.2 The adsorption of PEMs on the ISFET chip as a function of the surface potential

4.2.2.1 Potentiometric, in-situ detection of the PEMs buildup

In the fixed reaction chamber, a consecutive adsorption of PE was performed, which was monitored by the ISFETs. For a potentiometric measurement, the in-situ PEMs adsorption on the silanized gate surface was monitored by changes in drain-source current as function of time. In Fig 4.25, the consecutive adsorptions of three double layers of PSS/PAH were monitored by the ISFET.

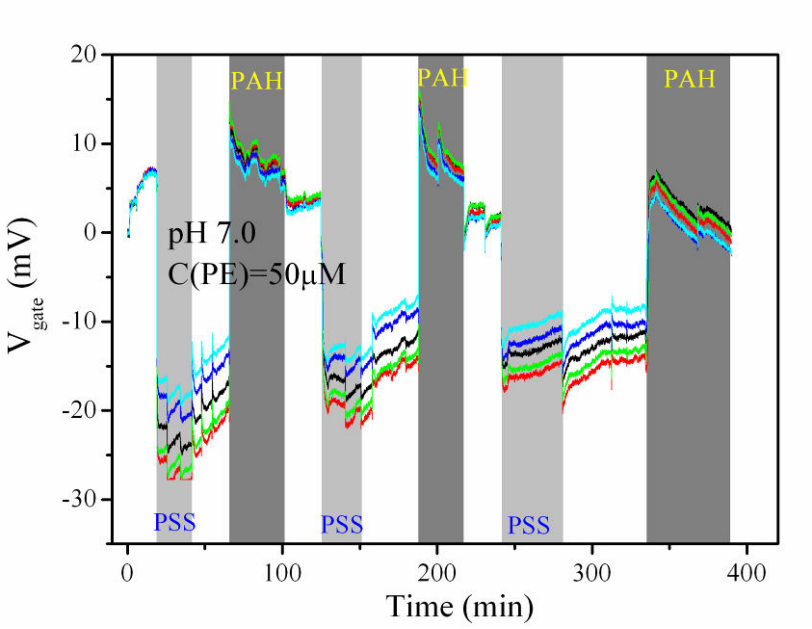

Fig 4.25 Time-dependent ISFET measurement with the negatively charged PSS and the positively charged PAH on the APTES-silanized surface. PEs were diluted in TE buffer solution (10 mM Tris, 1 mM EATA, 0.01 mM NaCl). Different colors indicate different PE layers, light grey are PSS, and dark grey stands for PAH.

The adsorption of the first negatively charged PSS layer on the APTES-modified gate FET surface caused a negative flatband voltage shift, resulting in signal amplitude of about 20 mV after rinsing several times with the initial buffer solution. By this rinsing with the buffer solution, the untethered PSS was rinsed away from the sensor surface. A positive signal was recorded for a further attachment of the positively PAH to the PSS covered surface. By comparing the total signal amplitudes for the strong acid PSS and the weak polyelectrolyte PAH it is clear that a similar surface charge density was introduced to the

transistor surface by each polyelectrolyte monolayer. With increasing thickness, the outer charges are moved away from the surface, leading to a signal reduction. Although the stoichiometry of the PSS and PAH was 1:1, the PAH charges overcompensate the PSS charges in this experimental condition (Riegler et al. 2002).

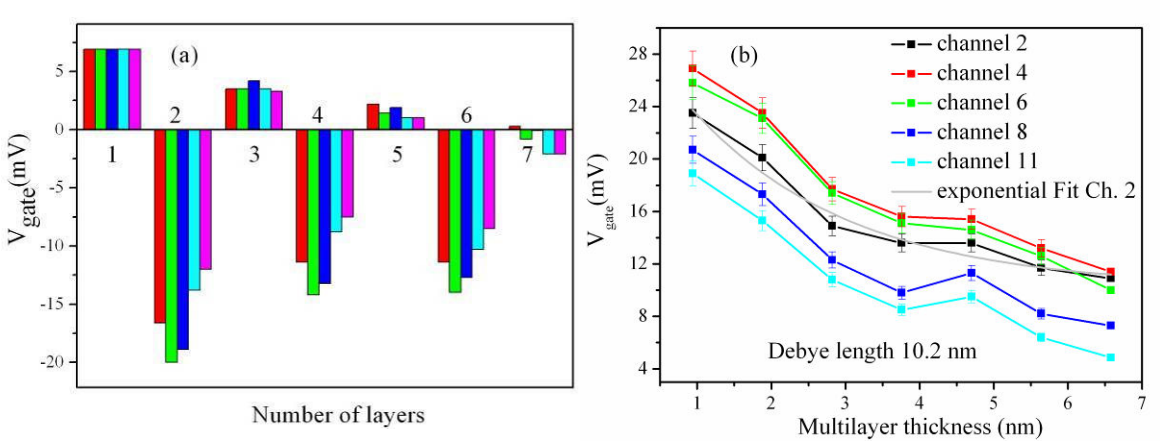

Fig 4.26 Column graph of the recorded voltage changes on the same chip after rinsing with the buffer solution (a). In (b) the respective absolute differences in gate voltage for each single PE layer are plotted. The error bars resulted from the statistics of the 5 ISFET gates.

The Debye-Hückel theory relates the attachment of charges to a solid-liquid interface to a corresponding surface potential change (Eq.18). An additional signal from the ISFETs may be generated, if the ionic strength, the electrical permittivity or the temperature of the PE solution was different from the bare buffer solution. These effects can be neglected for the recordings presented here, because after attachment of the charged molecules to the surface the chamber was flushed with bare buffer solution again, which resulted in the initial starting values of temperature, permittivity, ionic strength and pH. Attachment of charged molecules to the surface will result in a change of the surface potential and the resulting direction of the flatband voltage shift is charge-sensitive. In the present study, the ionic strength of the used TE electrolyte was 6 mM at room temperature.

The following possible mechanisms for explanation of the experimentally observed effects can be suggested: change in the flat-band voltage of an EIS structure or threshold voltage of an ISFET induced by the intrinsic charge of the adsorbed macromolecules; change in the ion concentration (including proton concentration) in the intermolecular spaces and pores or inside the PE multilayer (Poghossian et al. 2006b; Uslu et al. 2004) or impedance effects of the adsorbed layer on the ISFET gate input (Neff et al. 2006; Picart et al. 2004).

The voltage signal of FET depended exponentially on the thickness of PEMs on the FET surface (Fig 4.26). It was reported that the thickness of PE monolayer on solid support is strongly affected by the deposition conditions, especially pH. At pH 6-8 the polyelectrolyte films collapse and thicknesses as low as 5 Å per layer were reported (Shiratori et al. 2000). The output signal amplitude of our ISFET measurement decreases with increasing multilayer thickness, and the adsorption of the first PAH layer overcompensates for the previous surface (Riegler et al. 2002). The resulting signal amplitudes were indicating an exponential distance dependency of the transistor signal.

Furthermore, the PEMs adsorption with PSS/PEI pairs was done with the same condition of pH, concentration and temperature as previous experiment. In Fig 4.27, the response of the gate voltage with changing PE type is shown.

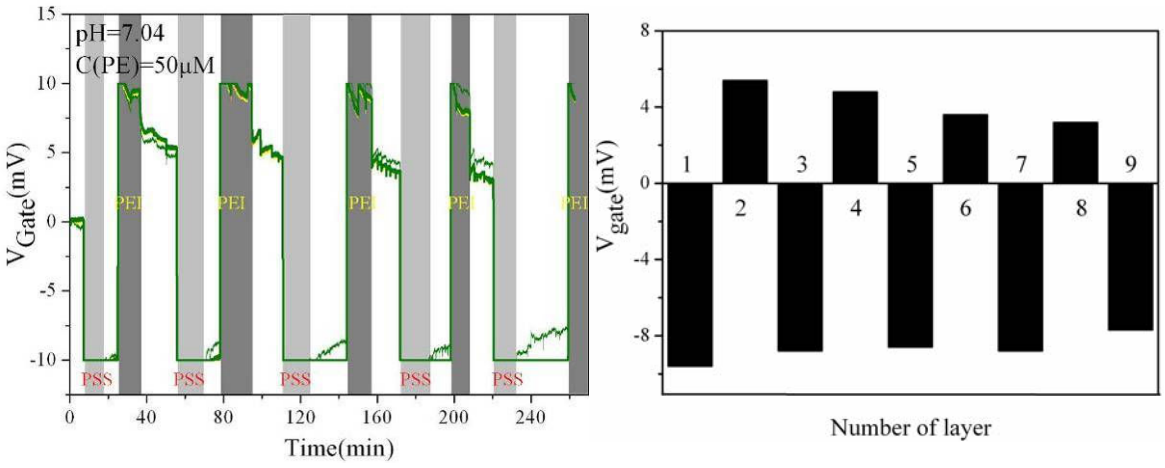

Fig 4.27 Time-dependent measurement of the alternating adsorption of negatively charged PSS and positively charged PEI and the column graph of the gate voltage response to the alternating adsorption. Light grey are PSS and dark grey stands for PEI.

In a pH 7 buffer solution, PEI is higher dissociated than PAH. Compared with the adsorption of PAH/PSS, the signal amplitudes recorded during adsorption of the PEI/PSS PEMs were much larger compared to the PSS/PAH PEMs. Seen from the Fig 4.27, the signal generated by the adsorption of PSS reached the threshold of the recording system. The PSS layer adsorption signal also decayed with increasing number of layers. The higher signal amplitudes of PEI compared to PAH demonstrated the overcompensation effect during the buildup of the PEMs.

4.2.2.3 Potentiometric, in-situ detection of a DNA/PE multilayer buildup

To investigate the adsorption of DNA on the ISFET gate surface, the PSS was replaced by a 20 bases Poly-T DNA sequence during the multilayer buildup.

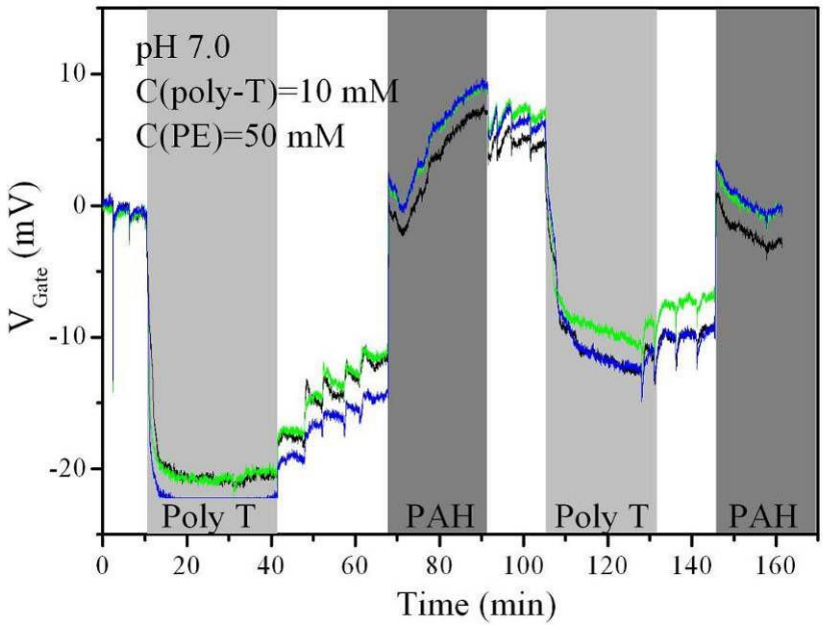

Fig 4.28 Time-dependent ISFET measurement with the positively charged polyelectrolyte PAH and the negatively charged DNA (poly-T 20bp) (3 transistor channels are shown). The attachment of the charged molecules at the transistor gate is shifting the flatband voltage of the device resulting in signal amplitude of about 15 mV after rinsing with the initial buffer solution. The direction of the signal shift depends on the positive or negative charge of the molecules.

The conformation of ssDNA in solution in general, especially long sequences is comparable with the conformation of the PE. The attachment of the short sequence ssDNA and PAH in our experiment caused a voltage shift in opposite directions. The adsorption of the first layer ssDNA on the APTES-silanized surface in this experiment was a non-covalent immobilization. The resulting signal amplitude after rinsing with buffer solution was about 10 mV, because a high concentration of poly-T (10μM) was used in this experiment. Compared with the PSS/PAH adsorption, the first layer of the poly-T gave the same amplitude signal as PSS, showing the same charge density on the gate channels. Therefore, the surface coverages of the first two layers must be different, because of the different length of the molecules.

A theoretical description for the electronic detection of charged molecules in an electrolyte solution using an electrolyte-oxide-semiconductor (EOS) structure is not completely available and still under discussion (Bergveld 2003; Landheer et al. 2005; Poghossian et al. 2006a; vanHal et al. 1996). In the literature it has been mentioned that an accumulation of charged biomolecules at an electrolyte-oxide interface should not generate any signal, because the charge of the biomolecules will be screened by counter ions (Bergveld 1991b; Bergveld 1996). The generally used theoretical description for the charging and discharging of an EOS interface with SiO_2 as oxide material is based on the Site-Binding model (Bousse et al. 1983). Compared with common MOSFET (metal oxide semiconductor) structures the threshold voltage of an ISFET device depends additionally in a linear way on the surface potential ψ_0 of the oxide electrolyte interface. The oxide surface can be charged or discharged by interaction of the -OH groups of the interface with free protons of the electrolyte.

It has been suggested that the accumulation of charged molecules at a surface might be electronically detected as responses to a Donnan potential, which is built up during the attachment of the molecules (Bergveld 1996). The accumulation of these negative charges at the gate oxide of the FET structure caused a shift in the flatband voltage of the transistor, which results in a voltage drop of the output signal in time-dependent measurements. Whether this signal is generated by the build-up of the above-mentioned Donnan potential or whether the signals are generated because of other reasons (e.g. change of the Helmholz layer of the interface) cannot be decided now and will need further investigations.

Nevertheless, the ISFETs detected the attachment of charged polyelectrolytes and biomolecules on the surface as a potentiometric response of the gate voltage. Experiments with the adsorption of various PE and PE/DNA pairs showed that the ISFET was sensitive to the changing of potential on the surface and towards the DNA hybridization process.

4.2.3 Basic transfer function behavior of the ISFETs

In the previous paragraph, it was presented that the ISFET as potentiometric sensor is sensitive to the surface potential change caused by the adsorption of charged molecules. Meanwhile, our newly developed ISFET system can additionally be used as an impedimetric sensor to monitor varying impedance at the gate input. In general, several groups have used the impedance spectroscopy in recent years for the analysis of impedance

changes at modified electrodes upon biorecognition events. In paragraph 2.5, an equivalent circuit described the biological reaction on the ISFET surface as the combination of frequency dependent capacitance and constant resistance in the full frequency range (Fig 2.16). For potentiometric readout mainly the potential at the ISFET gate is monitored. By the impedimetric readout, the input impedance is measured as a function of frequency. In general, the formation of a molecular layer on a gate-oxide surface alters the capacitance and the resistance of the solid-liquid interface. Electrochemical reactions occurring at the electrode/electrolyte interface can be modeled by extracting components of the electronic equivalent circuits that corresponds to the experimental impedance spectra (Antonisse et al. 2000; Kharitonov et al. 2001; Zayats et al. 2001; Zayats et al. 2002a).

4.2.3.1 Effect of the electrolyte conductivity on the transfer function characterization

For a basic characterization, the effect of electrolyte conductivity on the transfer function was characterized (Sakkari 2005). Firstly, the freshly cleaned ISFET chip was immersed in NaCl solutions of different concentrations. For these experiments, a closed reaction chamber of 0.5 ml volume was used. This ensured stable experimental conditions and side parameters like pH or temperature of the buffer solution were kept constant.

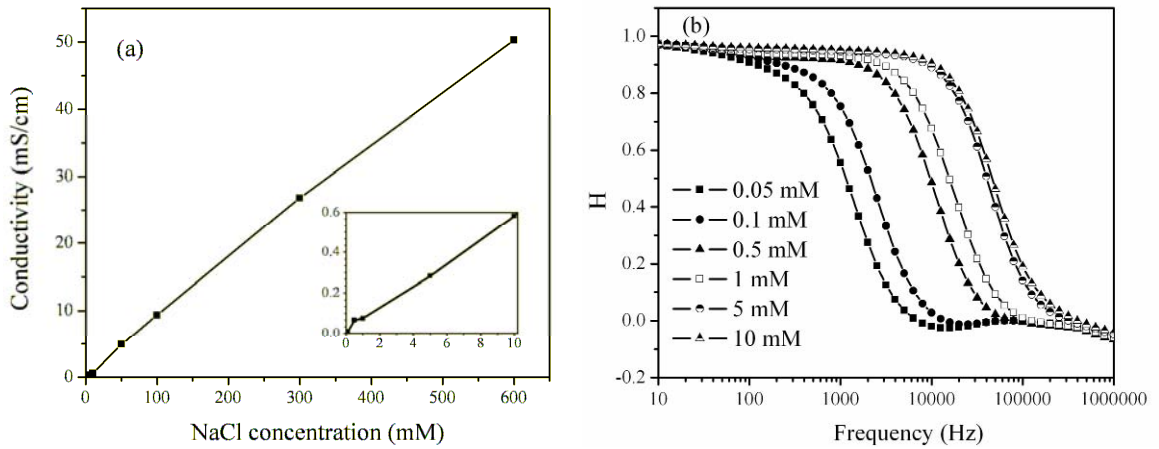

Fig 4.29 The change of the electrolyte conductivity with concentration of the NaCl solution (a). The transfer function is highly dependent on the electrolyte conductivity (b).

As expected, the conductivity increased linearly with the increase of NaCl concentration from 0.01mM, 0.05mM, 0.1mM, 0.5mM, 1mM, 5mM, to 10mM (Fig 4.29). This was confirmed in reference measurement with a standard conductivity meter (S30 Seven Easy

conductivity, Mettler Toledo, Germany). In the transfer function measurements, a shift of the transfer function curve to higher frequencies was observed with higher concentrations of NaCl. In highest conductivity solutions (NaCl concentrations>10mM), the transfer function exceeded the general frequency limitations of the amplifier system.

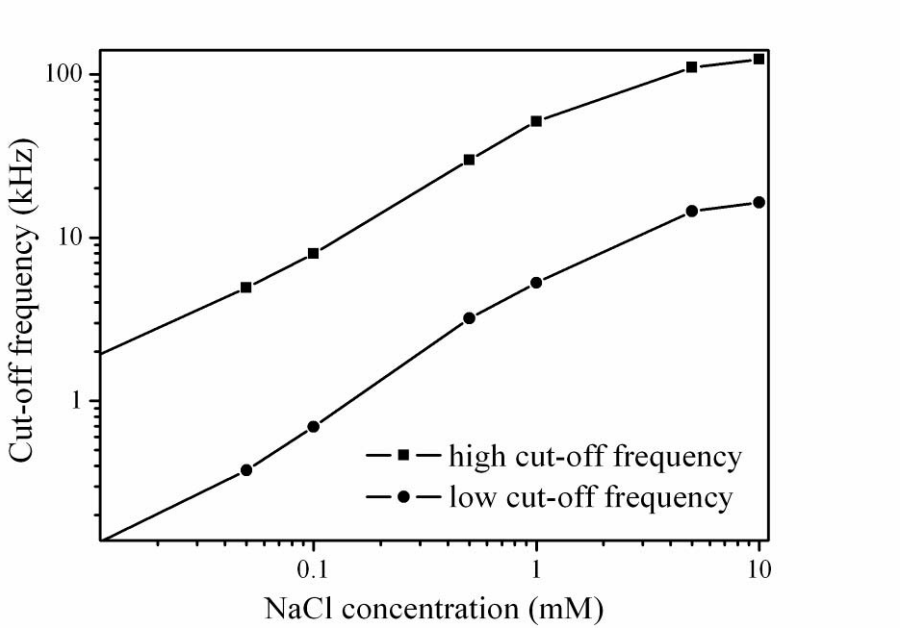

Fig 4.30 Change of the low and high cut-off frequencies of the transfer function with diffeent NaCl concentrations. The cut-off frequencies were extracted from the graphs in Fig 4.29b according to the graphical method described in Fig 2.6.

For the transfer function curve, the two time constants τ_1 and τ_2 can be extracted, which are the reciprocal of the cut-off frequencies. The changes of high and low cut-off frequency as a function of different NaCl concentrations are plotted in Fig 4.30. The equivalent circuit in Fig 2.16 can describe the change of the transfer characteristics with different salt concentration solutions. The overall time constant of the ISFET amplifier system is $\tau_1 \approx R_{sol} C_{CL}$.

4.2.2.2 Transfer function curves in different pH solutions

To further verify the reliability of the transfer function readout, chips were freshly cleaned with EtOH, and dipped in standard pH value solutions (Titrisol standard pH solution, Merck Germany) with pH values of 2, 4, 6, 8 and 10, respectively.

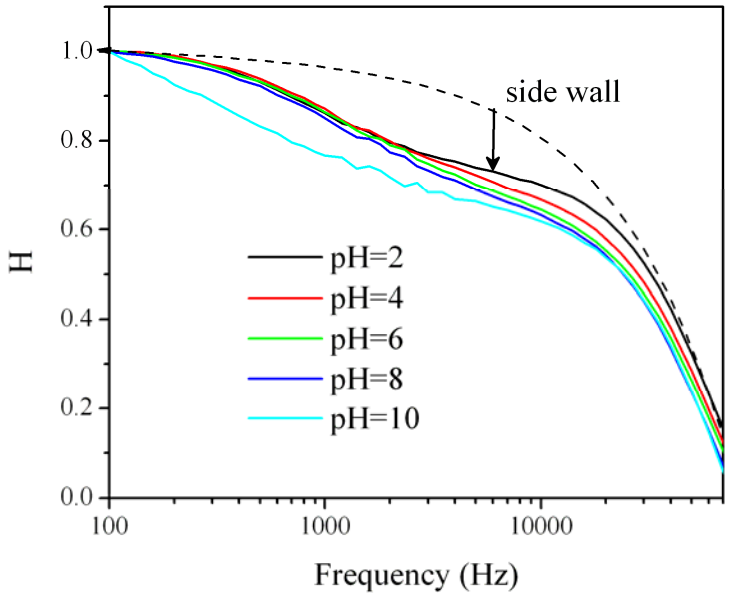

Fig 4.31 Frequency-dependent transfer function curve of the ISFET chip immersed in different standard buffer solutions of pH 2, 4, 6, 8, and 10 respectively. The curves were normalized at 100 Hz. The dotted line shows the standard transfer function curve.

Because of the high conductivity of the standard pH solutions, the transfer function curves were almost outside the general limit of the amplifier system. Therefore, the high cut-off frequency was detectable. There is a minimum difference of the transfer function curves for different pH buffer solutions. The different shape of the transfer function curves from the ideal shape originates from a sidewall effect, which was found to influence the curves of the dip-chip designs. This effect was intensively studied in a related project (Kottuppallil 2006), but was identified not to reduce the selectivity of the DNA readout of the 8-channel array chips.

In summary, the main effects of the transfer function curves were identified as conductivity of the buffer solution and sidewall effect. In the following experiments, these two influences are taken into account.

4.2.4 Frequency-dependent transfer function behavior of the PEMs adsorption

We utilized the buildup of PEMs as model system for the DNA hybridization process. The PE adsorption processes were monitored by the potentiometric and impedimetric readout. In this paragraph, the transfer function behavior upon PE adsorptions are described. The

results were achieved in a related thesis (Sakkari 2005). To explain the main effect and the modeling by an equivalent circuit, the main results are shortly summarized in the following. After the adsorption of each layer, the transfer function scan was taken in the same buffer medium (TE buffer solution), which guaranteed the same conductivity of the electrolyte for each measurement.

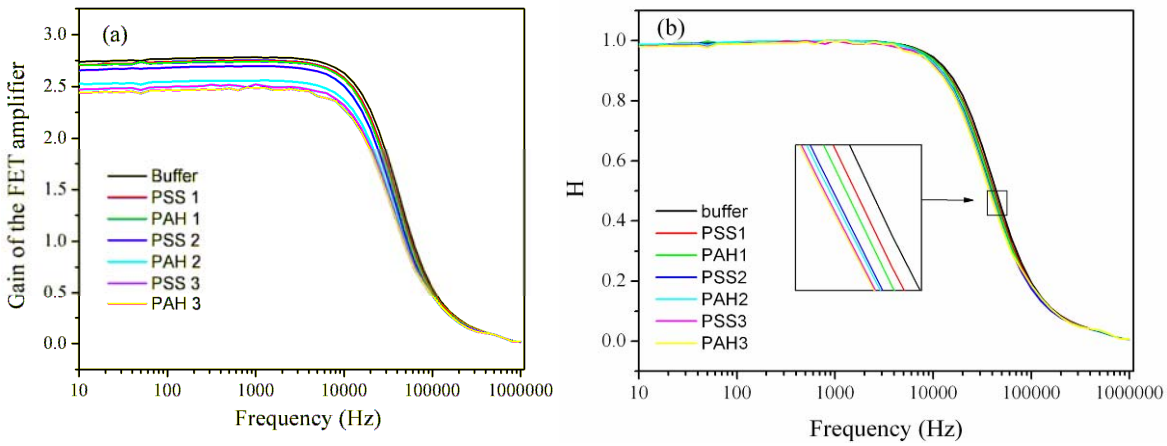

Fig. 4.32 Transfer function response of the ISFET sensor upon polyelectrolyte adsorption (a) change in gain with adsorption of each polyelectrolyte layer. (b) transfer-function of the polyelectrolyte adsorption. The graph is normalized at 100 Hz.

In Fig 4.32 the transfer function curves after each PE layer adsorption on the APTES-silanized starting surface are shown. In contrast to the custom-made amplifier system commercial impedance analyzer (S1-1260 IMPEDANCE/GAIN-PHASE ANALYZER, Solartron Analytical, England) was used, which allowed measurements up to 1MHz (Sakkari 2005). During the buildup of PEMs, two main parameters influence the transfer function curve, namely the resistance and capacitance of the PEM at the gate input.

4.2.5 Modeling of the frequency-dependent transfer function

To model the transfer function results of the PEMs adsorption, PSpice was exploited to simulate the complex electronic circuits.

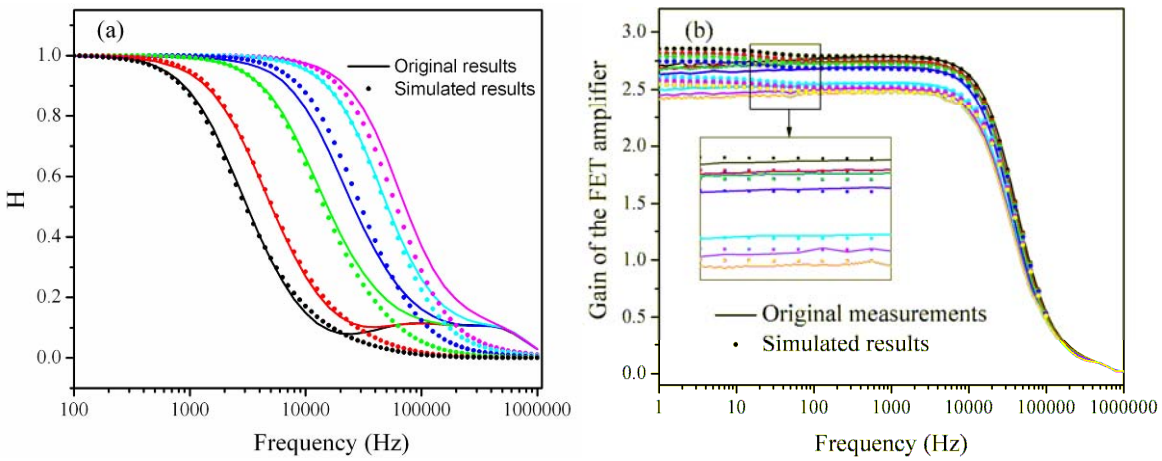

Fig 4.33 Simulation of the electrolyte conductivity measurements, (a) the transfer function curves are normalized. (b) PEMs adsorption with original gain of the FET amplifier without normalization (Sakkari 2005)

In Fig 4.33a and b the experimental data are fitted by the equivalent circuit. By this procedure the main components responsible for the experimentally observed changes were identified. The basic components of the equivalent circuit for the conductivity measurements were already shown in Fig 2.16. These active and passive electronic components have direct influence to the transfer function. The electrolyte resistance (R_{serie}), and the contact lane capacitance $C_{CL} = C_{source} + \sum_i C_{drain}$ are the main determining factors for the conductivity measurements. The electrolyte resistance used for simulations were back calculated from the conductivity values of the solutions. The resistance of the reference electrode was assumed constant with different ionic strength of the electrolyte (Bucher et al. 1999). Furthermore, the double-layer for conductivity modeling was neglected, because it had not large influence on the transfer function graphs. The simulated graphs are included in Fig 4.33a.

For the simulation of the PEMs adsorption (Fig 4.34), it is assumed that the effective gate oxide impedance was the only influencing factor at the sensor surface along with the electrolyte resistance. Capacitance and resistance of the membrane were added under the double layer part, "n" is referred to the number of PE layers. As all the measurements were carried out in the same buffer solution, the electrolyte resistance (R_{serie}) was constant (4 kΩ) through the whole simulation. The capacitance of the each layer (C_{mem}) was calculated according to the gate are and inserted into the model. Although PEMs on both contact lines and the gate surface caused the change of capacitance, only the capacitance from the gate influences the transfer function curves, because of the large thickness of the ONO

passivation on the contact lanes of the chip. The capacitance variation at the gate surface (10nm thick) was changing from 20% to 30%, while the capacitance at the contact lines (ONO stack of 250nm, 130nm, 100nm respectively) was changing below 1% with adsorption of the PEMs. The membrane resistance was assumed to be in the order of GΩ. From the PSpice simulations, it was found that the PEMs adsorption in the frequency-dependent measurements was purely due to the change in the effective gate capacitance.

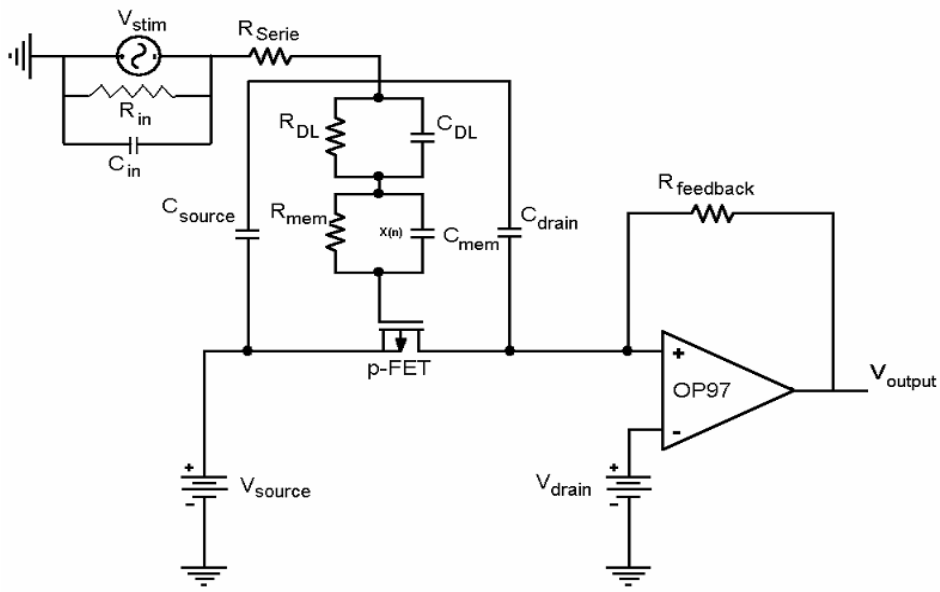

Fig 4.34 Equivalent circuit for modeling of the PEMs on the FET gate surface. The circuit is a further modification of the circuit in Fig 2.18 with R_{mem} and C_{mem} accounting for the PEM impedance.

From the simulation for the PEM adsorption in Fig 4.33b, the capacitance of the each PE layer was found to be 0.5~0.7pF, which is derived from the calculation of τ_1 and τ_2. By inserting this capacitance and the dielectric constant of the PE (ε_r=2.8) (Bordi et al. 2004), the thickness can be calculated as 3±2nm for each PE layer, which is consistent with the ellipsometry measurements, where the thickness of each PE layer was found to be 4±1nm (paragraph 4.2.1). Here, the capacitance calculations were made assuming the gate surface area as 100μm^2 corresponding to the chip design used in these measurements. In this way, the resistant and capacitance values of the PEM layer were simulated. The explanation and simulation values for the resistance and capacitance were given as the layers on the gate surface respectively.

Table 4.10 Simulation values R_{mem} and C_{mem}, which are modeling the PEM impedance of the gate input.

Simulation parameters	explanation	Simulation values
R_{mem}	Resistance of the layers on the gate surface	500 GΩ
C_{mem}	Capacitance of the layers on the gate surface	0.6 pF for each layer

As a summary of this paragraph, the adsorption of PE showed that the output signals of the FET are dependent on the charge of the attached molecules. In addition, the signal amplitudes were found to be exponentially distance-dependent in the range of the Debye length of the used electrolyte. We presented a method for the label-free detection of charged molecules with ISFET devices. The detection was identified to be charge sensitive and in principle all kinds of charged molecules dissolved in a weak electrolyte solution could be detected (e.g. immunoassays or protein detection) as long as they attach close enough to the surface. The ISFET structure can be integrated in standard CMOS processes and multiple sensor chips may be feasible in future (Yeow et al. 1997).

The PEMs buildup can be detected by AC and DC readouts using the ISFETs. With the potentiometric system, the output signal during the in-situ buildup was charge sensitive. The results proved that the signal detection is less sensitive with increasing distance away from the surface. The PE as a model system can also be paired with ssDNA to perform a PE/DNA multilayer buildup. Furthermore, the PEMs can be detected by the transistor transfer function readout to provide a detailed explanation of the equivalent circuits. In order to identify the main parameters of the equivalent circuits, simulations were performed based on the experimental results. The basic equivalent circuits for the conductivity measurement offered the basic influencing components. For the PEMs the signals can be modeled by adding a higher input impedance from the PE membrane.

In the following, the ISFET system is utilized for the detection of biomolecular binding reactions.

4.3 Label-free detection of biomolecular reactions with the FET assays

On the modified gate surfaces of the ISFET biosensor arrays, biomolecules such as probe ssDNA and biotin were immobilized (paragraph 4.1). The DNA hybridization reaction and the biotin/streptavidin binding processes were label-freely detected in a liquid environment in in-situ and ex-situ assays. Two different readouts (DC and AC) were utilized to detect the biomolecular reactions at the ISFET gate surfaces.

4.3.1 Label-free detection of DNA hybridization with a potentiometric readout

In the DC measurements, the 8-channels FET biosensors were utilized to perform the detections (Appendix). Long-term drift of FET devices at the gate input (Jakobson et al. 2000; Jamasb et al. 1998; Jamasb 2004) is mainly influenced by the type of gate material (Bergveld 1996), which is chemically interacting with the electrolyte solution and by heating effects of the transistor channel. To minimize the drift effects during the

hybridization detection, a differential readout is applied between measure and reference transistor (Fritz et al. 2002; Pouthas et al. 2004b; Sakata et al. 2005b). In addition the supramolecular of architecture the ISFET gates was largely improved compared to previous protocols (Uslu et al. 2004). In practices, the reference channel/biosensor was set as reference in the custom-made software and the results from the rest channels/biosensor were compared.

4.3.1.1 Electronic detection of DNA immobilization and hybridization

All electrical recordings of DNA immobilization and hybridization were done at room temperature. For a first trial of a differential readout, two identical biosensor chips were functionalized differently and channels with the same g_m value from each biosensor chip were selected. In the time-dependent measurement mode, one chip was set as reference for a differential readout of the other chip. The change in the drain-source current was recorded and with the known g_m of the transistor transformed into the respective gate voltage. The DNA immobilization and hybridization reaction cause a change in surface potential at the gate, which results in a change of the flatband potential and hence a change in the I_{DS} of the FET (Pouthas et al. 2004a).

For the immobilization experiment, the reference biosensors were only treated with activation (MeOH/HCl) and silanization (APTES in gas phase). The detection biosensors were treated the same, but additionally the crosslinking process with succinic anhydride was applied. After this functionalization, the two biosensors were immersed in the same reaction chamber full of 3µM ssDNA in MES buffer. For the hybridization experiment, probe ssDNA of different sequence were immobilized on the two biosensor chips (reference biosensors: FMM DNA; detection biosensors: PM DNA) according to Table 4.4. The whole immobilization processes were performed overnight. The hybridization detections were carried out in a TE buffer (pH 8.0) solution with 3µM target DNA.

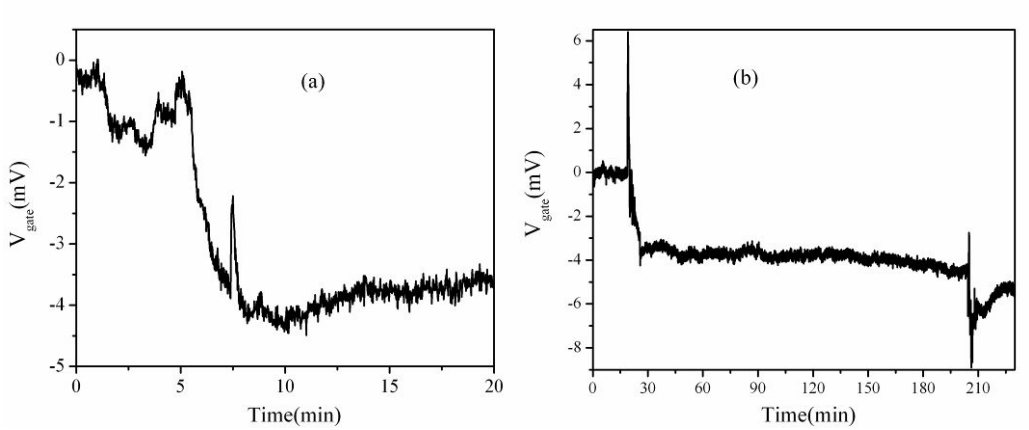

Fig 4.35 Real time detection of the DNA immobilization (a) and hybridization (b), which caused a rapid change in the gate voltage of the FET. In both graphs, the differential signals are plotted.

In Fig. 4.35 the differential, time-dependent measurement for the immobilization (a) and hybridization (b) reactions are shown.

In the immobilization experiment (Fig 4.35a), the difference between the covalent binding and the physisorption of probe DNA on the gate surfaces is detected. The surface modification of activation, silanization and crosslinking led to covalent binding of probe DNA, while on the silanized silicon oxide surface of the reference chip non-specific adsorption will occur. The change of the gate voltage of the measurement chip can be attributed to a different efficiency between physical adsorption and chemical covalent binding with the latter being more efficient.

In Fig 4.35b, the real time detection of the DNA hybridization by the differential readout approach is shown. Two identical chips were immobilized with PM and FMM probe ssDNA, respectively. For the hybridization readout, one channel from the FMM immobilized chip was set as reference channel. The differential readout signal displayed is recorded from one channel of the PM-immobilized chip. The hybridization process in this in-situ detection was finished in about ten minutes. The baseline of the signal was then stable for more than 2 hours, which confirms the high stability of the differential readout. A buffer rinsing step at 205 min was not significantly changing the recorded amplitude. The hybridization signal amplitude was similar to the amplitude of the DNA immobilization for the same concentration of DNA.

With the label-free ISFET detection in these two experiments, the covalent binding and the non-covalent binding were distinguished, which is related to different DNA immobilization conformations. With the non-covalent binding by electrostatic attachment, the ssDNA segments are more likely to lie flatly on the surfaces. In contrast to this, the covalent immobilization of DNA can offer a highly ordered layer. With a higher surface coverage and highly packed probe DNA, the possible hybridization signal is higher.

4.3.1.2 Detection of single nucleotide polymorphisms with a potentiometric readout

The single mismatch DNA hybridization detection was carried out on the same chip. After the activation, silanization and crosslinking process, different sequences of probe DNA from FMM, 3MM, 2MM to PM at the same concentration 3 μM were spotted onto the gate arrays (Table 4.4). An overnight incubation finished the immobilization process. For hybridization detection, the chip was dipped into 500μl TE buffer and the working point of the ISFETs was set. The target DNA was applied into the reaction chamber at the rate of 1.0 ml/min by the use of a peristaltic pump (ISMATEC, USA). The hybridization was monitored in-situ, with the FMM probe DNA gate as reference.

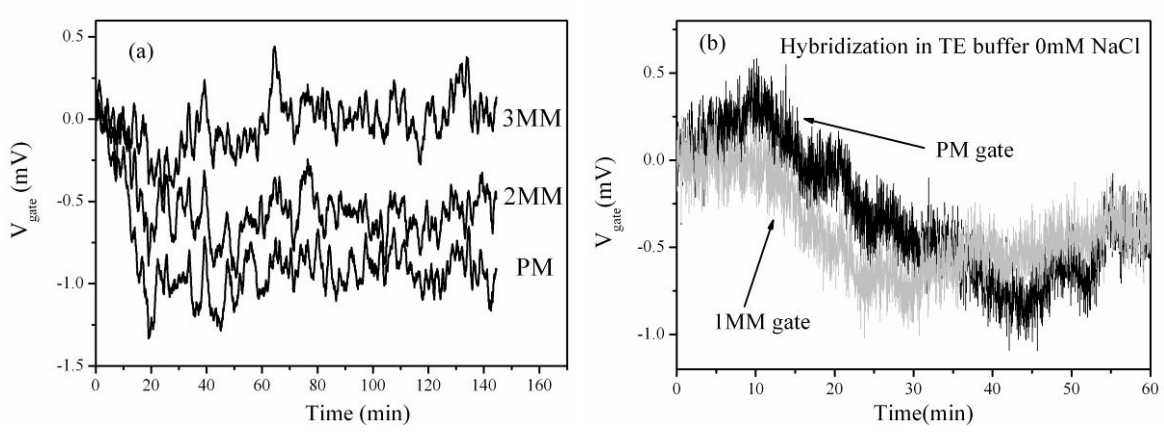

Fig 4.36 The real time detection of the hybridization for different sequence (a: FMM, 3MM, 2MM to PM; b: FMM, 1MM and PM). Before starting this experiment, the baseline of the signal was stable for more than 2 hours. The gate with FMM was set as reference gate, respectively.

In Fig 4.36 the gate voltage change for different DNA hybridization reactions with the FMM gate as reference channel are shown. In order to avoid charge screening of the DNA molecule, the ionic strength of the buffer electrolyte must be kept very low during the

potentiometric field-effect detection of DNA hybridization (Fritz et al. 2002; Pouthas et al. 2004b; Uslu et al. 2004). Usually, the effective voltage change at the gate output is about 1-6mV, mainly depending on the ionic strength of the buffer electrolyte and on the density of the attached probe molecules. Although the selectivity of the SNPs detection was high enough to be detected by fluorescence microscopy on the control substrates (paragraph 4.1), in this experiment, the difference between PM, 1MM, 2MM and 3MM was barely distinguishable for the potentiometric in-situ readout. Therefore, an in-situ assay for the potentiometric readout was not possible for the SNP detection.

4.3.2 Label-free detection of DNA hybridization with an impedimetric readout

Because of the low selectivity of the DC readout for the SNPs detection in the in-situ assays, an amplifier system for impedimetric readout of the ISFET arrays was developed to achieve this detection. Here the ex-situ procedure was applied similarly to the protocols described before.

4.3.2.1 Influence of the buffer ionic strength

Concerning that the ionic strength of the buffer solution strongly influences the ISFET transfer function behavior, the concentration of the NaCl was optimized for the ex-situ detection assays. PM probe ssDNA was immobilized on the biosensor surfaces, and 2 hour hybridizations were carried out in target DNA solutions (3μM in 4×SSC buffer). The transfer function scans before and after hybridization were done in the same NaCl concentration solutions. The selected NaCl concentrations were 0.01mM, 0.1mM, 1mM and 10mM. The differential transfer functions (DTF) between after and before hybridization are plotted in Fig 4.37. Utilizing the differential readout of the transfer function characteristics ex-situ eliminates side effects like pH, temperature drift, electrolyte composition, etc., which are usually the main drawback of the in-situ potentiometric readout.

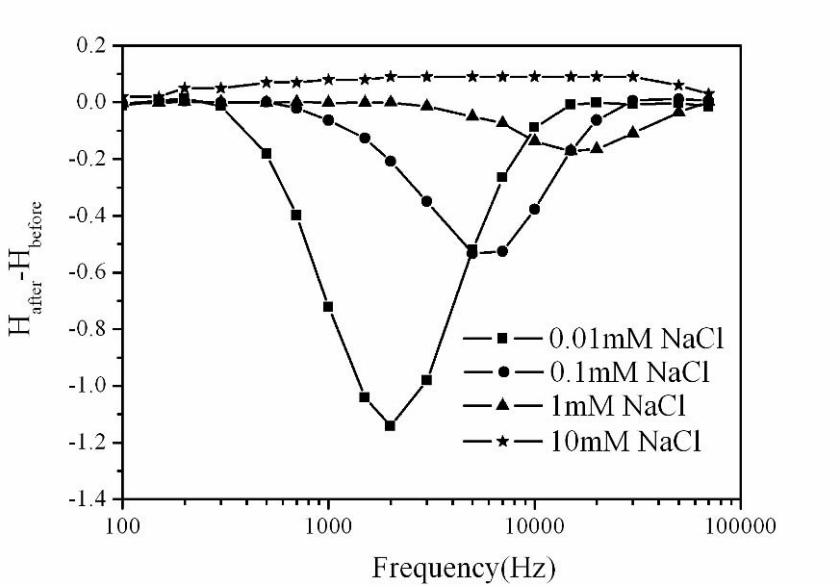

Fig 4.37 Differential transfer function between after the hybridization and before the hybridization in different concentration NaCl solutions. The transistor transfer function (TTF) scans for one channel from the same chip in the different NaCl solutions are shown. The TTF scans were not normalized for this graph.

As shown in Fig 4.37, the biggest DTF peak was obtained in the 0.01mM NaCl solution. With a 10 times higher NaCl concentration (0.1 mM NaCl) the peak amplitude decreased to 50%. For the concentration as high as 10mM NaCl, there was no peak observed in the accessible scan frequency range of the current FET amplifier system. The shift of peak locations along the frequency axis is corresponding to the conductivity change of salt concentrations (Fig 4.29). Therefore, the DTFs are not observable in the high ionic strength solutions and DNA hybridization detections are preferred in low ionic strength solutions. The different signal amplitude, however, follow the theoretically described behavior for higher signals with lower ionic strength (Landheer et al. 2005).

4.3.2.2 In-situ DNA detection in low ionic strength solution

In the fluorescence measurement, it was confirmed that 20mer ssDNA could hybridize in 0.01mM NaCl at the functionalized sensor surfaces (Fig 4.13). The in-situ detection of the DNA hybridization process in 0.01 mM NaCl was investigated using the transfer function scan at certain time intervals. PM probe DNA immobilized biosensors were dipped in reaction chamber with 3µM target DNA in 500µl of 0.01mM NaCl buffer solution. The transfer functions curves were recorded every half hour.

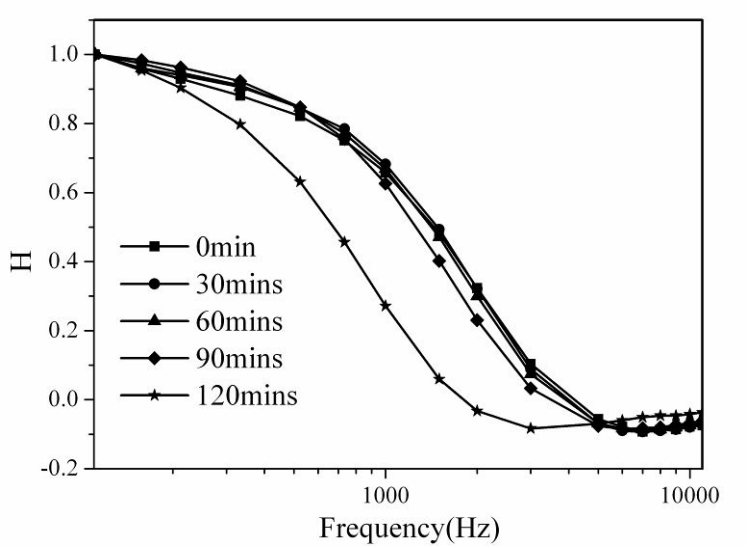

Fig 4.38 Transfer function curves for in-situ DNA hybridization detection at 0, 30, 60 and 120 minutes, respectively

In Fig 4.38 the transfer functions curves for the in-situ DNA hybridization process at 0, 30, 60 and 120 minutes are shown, respectively. The DNA hybridization processes resulted in a nonsymmetrical shift of the transfer function curves to the lower frequencies. In the first 90 minutes, the transfer function did not display great shift. Between 90-120 minutes, the transfer function showed a significant change, demonstrating the achievement of DNA hybridization in between 2 hours.

4.3.2.3 Highly selective, ex-situ detection of single nucleotide polymorphisms

As optimized before, the best distinguishable signal for DNA detection was recorded in the 0.01mM NaCl solution (Fig 4.37). It was previously predicted in a theoretical article that the usual buffer electrolyte concentrations used for DNA hybridization (150 mM NaCl or even higher) would not lead to large surface potential changes and changes in interface impedance. Larger impedance effects were expected at lower ionic strength of the buffer electrolyte (Landheer et al. 2005). In our experiments, the SNP detection was performed in an ex-situ assay in the low ionic strength detection solution. DNA immobilization, sequences (Table 4.4) and the microspotting procedure were identical to the potentiometric detection (paragraph 4.3.1.2). Different ssDNA sequences PM, 1MM and FMM were immobilized onto the ISFET gate array by microspotting. For this experiment, the 8-channel dip chip ISFET sensors were used. After immobilization and hybridization with target DNA, the chips were immersed in 0.01mM NaCl to conduct the transfer function detection. Four channels of the same chip were selected.

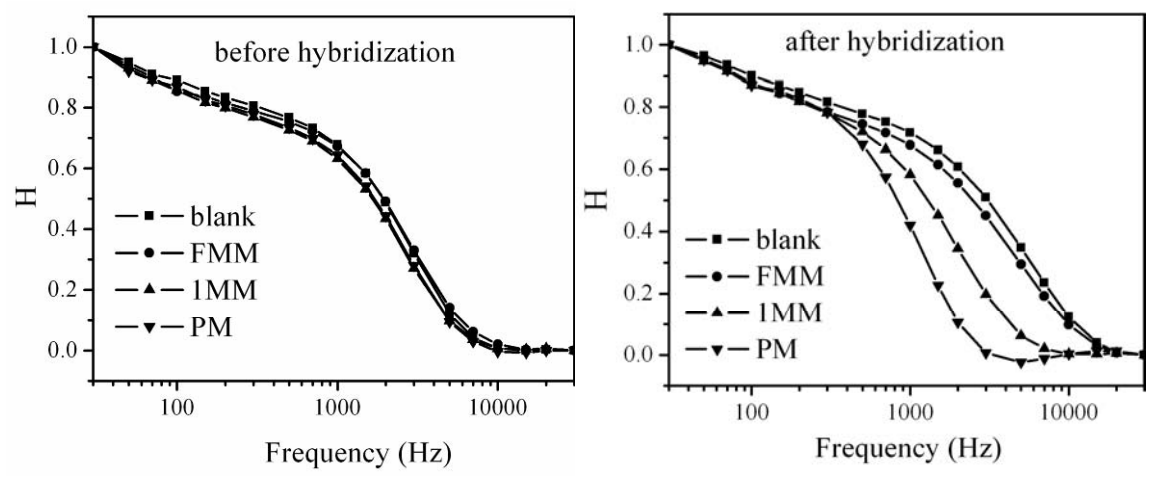

Fig 4.39 Different transfer functions before and after hybridization. The blank, FMM, 1MM, and PM channels were located on the same 8-channel ISFET chip.

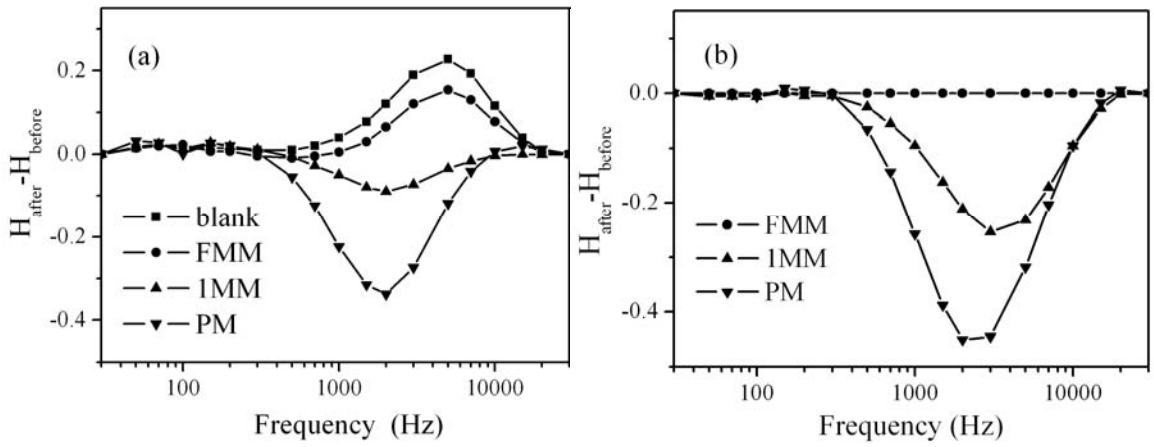

Fig 4.40 Differential transfer functions: transfer function as difference between after and before hybridization (a) and differential transfer functions with the FMM as reference channel (b)

The transfer functions before and after DNA hybridizations are shown in Fig 4.39. In Fig 4.40, the DFTs for the different probe DNAs are displayed. Before the hybridization, the transfer functions for different probe DNA display a similar behavior, whereas after hybridization the transfer functions largely differentiate. With the introduction of a DNA layer after hybridization at the gate input, the interface capacitance will increase (Gu et al. 2005), which decreases the cut-off frequency. The magnitude of the change in the cut-off frequency for the individual channel is related to the different hybridization efficiency with the probe DNA on the respective transistor channel. The transistor gate, where the most probe DNA molecules were reacting, experienced the largest impedance increase of the attached DNA layer, because of the impedance increase with increasing number of fixed

charges at the oxide surface (Landheer et al. 2005). The differences between FMM, 1MM and PM can be clearly distinguished. Hence, the selectivity of the presented method was high enough to enable the detection of SNPs.

From the simplified equivalent circuit of the readout system (Fig 2.16), the DNA layer acts like a biomembrane, and the time constants are:

$$\tau_1 = R_{DNA}(C_{DNA} + C_{OX}) \approx R_{DNA}C_{ox}, \tau_2 = R_{DNA}C_{DNA}$$

The second time constant provides the relaxation time of the DNA membrane. The overall high cut-off frequency of the transistors was mainly dependent on the total sheet capacitance of the whole contact lane area in combination with the series resistor formed by the access resistance of the reference electrode and the resistance of the solution as explained before (paragraph 2.3). The high cut-off frequency was located in the kHz range, because of the large areas of the implanted contact lanes of chips in combination with the large solution resistance due to the dilute salt concentrations. The different impedances of the gate inputs cause the individual cut-off frequency differences at the different gates in the SNP experiments.

Using a FMM channel as reference resulted in a reliable detection of SNPs (Fig 4.40). The impedance effects owing to DNA hybridization were predicted to be much larger with lower electrolyte concentrations. In accordance to the theoretical predicted effects, the differences between FMM, 1MM, and PM were more obvious at lower electrolyte concentrations in our experiment (<1mM) (Landheer et al. 2005)

4.3.2.4 Ex-situ detection of a multi-hybridization process

The multi-hybridization processes of longer DNA segments (50b.) were recorded in the form of the transfer function detection in an ex-situ assay. After the standard surface modification, 20mer PM probe ssDNA was immobilized on the biosensor gate surface, and incubated overnight. Four times hybridizations were carried out with the two target DNAs (Table 4.11) alternatively and recorded in the TE buffer solution. The transfer function was recorded after each step (Fig 4.41).

Table 4.11 Probe DNA and two target DNA sequences in this sandwich multi-hybridization experiment

Probe DNA
5'MMT-ATGAACACTGCATGTAGTCA-3'
1st target DNA
5'-TGCTAGTGACGTACACTCGATTTTTTTTTTTGACTACATGCAGTGTTCAT-3'
2nd target DNA
5'-TCGAGTGTACGTCACTAGCATTTTTTTTTTATGAACACTGCATGTAGTCA-3'

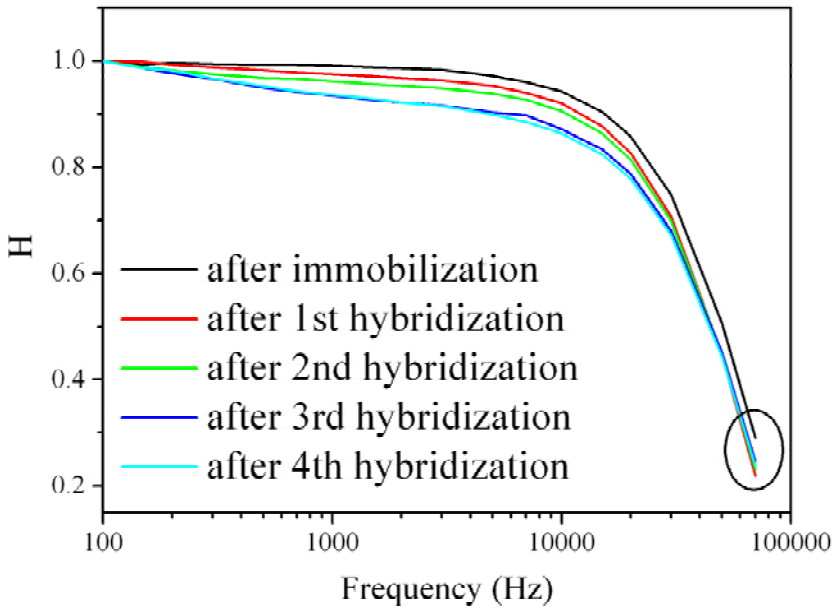

Fig 4.41 Ex-situ transfer function measurements of a multi-hybridization process. The TTF curves shift to lower frequencies.

In Fig 4.41, one channel from the 8-channel ISFET chip was selected to show this process. Because of the higher conductivity of the TE buffer with 0.01mM NaCl (16.43mS/cm) in this experiment, the high cut-off frequency τ_2 was not visible in the scans. However, transfer function measurements showed that the DNA multi-hybridization had only minor effects on the relaxation time τ_1 (Table 4.12).

Table 4.12 Time constant τ_1 extracted from the transfer function after each hybridization step.

Numbers of hybridization	Before hybridization	After 1st hybridization	2nd	3rd	4th
τ_1 (ms)	0.041	0.045	0.042	0.039	0.039

In the high frequency range, the transfer function curve for before hybridization slightly differed from the hybridization curves at the end of the curves (circle in Fig 4.41). Compared to the hybridization experiments presented in the previous paragraph, the signal changes were not very pronounced because of the higher ionic strength of the buffer. In the multi-hybridization experiment, the first hybridization lead to the highest signal changes. In addition, the multi-hybridization experiment resulted in comparable recordings like presented before with the PEM experiments (paragraph 4.2.4).

4.3.2.5 Exploration of gold nanoparticle modified target DNA to enhance the SNPs detection signal

The SNPs detection was done with DNA-modified gold nanoparticles (DNA-AuNPs) to investigate a possible signal enhancement for the FETs detection. Gold nanoparticles (Au-NPs) of 15nm diameter were obtained from the mixture of tetrachloric acid dehydrate ($HAuCl_4 \cdot 3H_2O$) and trisodiumcitrate dehydrate ($HOC(CO_2Na)(CH_2CO_2Na)_2 \cdot H_2O$) (6/255 weight ratio). The DNA-AuNPs were prepared by thiol modified ssDNA (SH-DNA) (5'-thiol-TGACTACATGCAGTGTTCAT-3'), which was covalently immobilized onto the Au-NPs. The hybridization reaction occurred between the probe ssDNA and the DNA-AuNPs for 2 hours at room temperature. In Fig 4.42 the preparation process of the AuNPs and a schematics for the hybridization process with DNA-AuNPs are depicted.

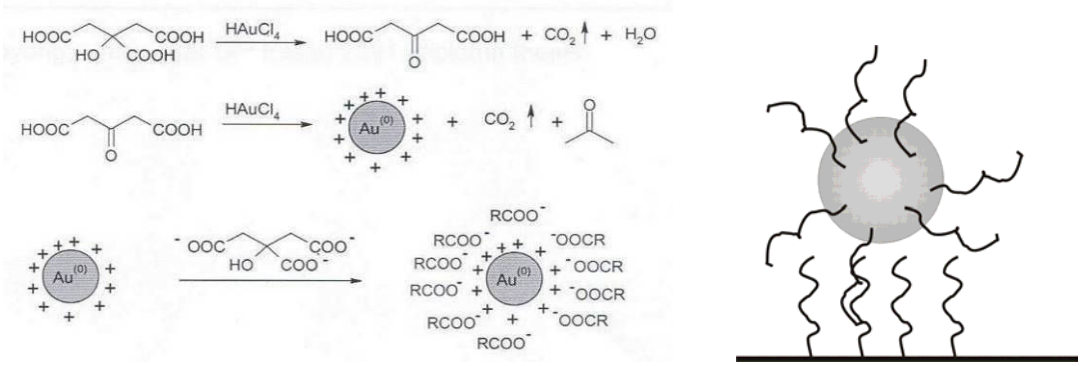

Fig 4.42 Schematic drawing for the preparation of size tunable gold nanoparticles (left). The gold nanoparticles were modified with SH-DNA oligomers. By this, a possible higher amount of target DNA should attach to the sensor surface together with the AuNPs. The ex-situ hybridization reaction was performed with DNA-AuNPs (Niemeyer et al. 2001; Niemeyer et al. 2005; Peschel et al. 2002)

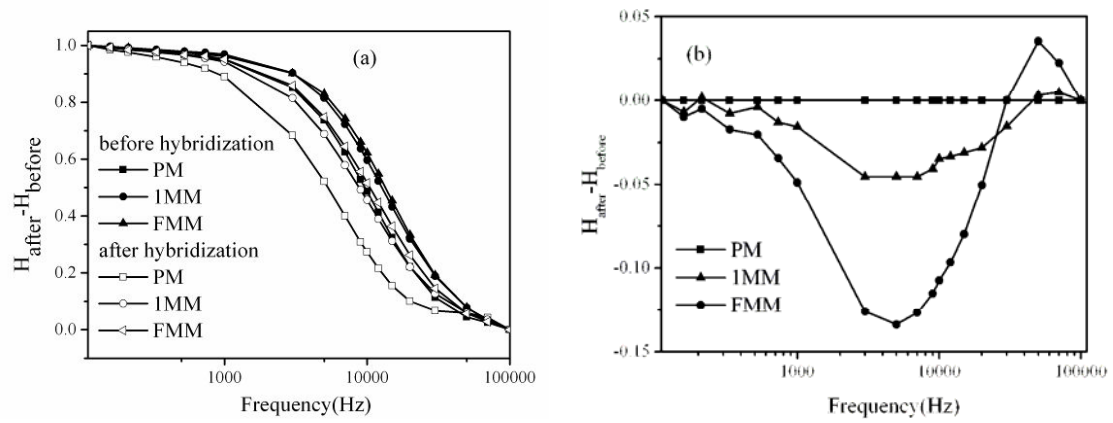

Fig 4.43 Transfer function curves of the individual ISFET channels before and after hybridization with Au-particle cDNA (a) and the differential transfer function of after and before hybridization (b) measured in 0.01mM NaCl

In this assay, we used the same procedure of probe DNA immobilization compared to the normal SNPs detections in Fig 4.39 and 4.40. Three different probe ssDNA sequences were microspotted on the ISFET gates to perform the covalent immobilization. The DNA-AuNPs hybridized with a different efficiency on the individually gates. The transfer function curves were recorded in 0.01mM NaCl before and after the hybridization. The resulting differential transfer function curves showed similar results compared to the normal SNPs experiments. Before the immobilization, the transfer functions curves were similar for the three different probe DNA transistor channels. After the hybridization, the transfer function curves shifted to lower frequency ranges. The adding of AuNPs caused the DNA membrane capacitance to increase and the membrane resistance to decrease (Lu et al. 2004). The DTF curves in Fig 4.43 displayed the high selectivity and sensitivity of the SNPs detection with the DNA Au-NPs. However, compared to the normal SNPs detection, the amplitude for all the recorded signals was smaller. A possible reason could be that the gold nanoparticles were located too far away from the surface to be detected. Furthermore, the low hybridization efficiency could be caused by a steric hindrance of the AuNPs. This results confirms that higher signal amplitudes can only be generated from near surface reactions on the ISFET structure.

4.3.3 Impedimetric detection of the biotin/streptavidin binding

Beside the DNA detection, the project is aiming to a direct electronic detection of proteins. As a first test, the biological reaction between biotin and streptavidin was detected with the differential transfer functions of the ISFETs. It was previously reported that protein

detection is very difficult and most recordings with ISFETs are not reliable (Bergveld 1991a). In this work, the biotin/streptavidin binding on the silanized gate surface was monitored in-situ and ex-situ to display the reaction and reliability of our AC readout system.

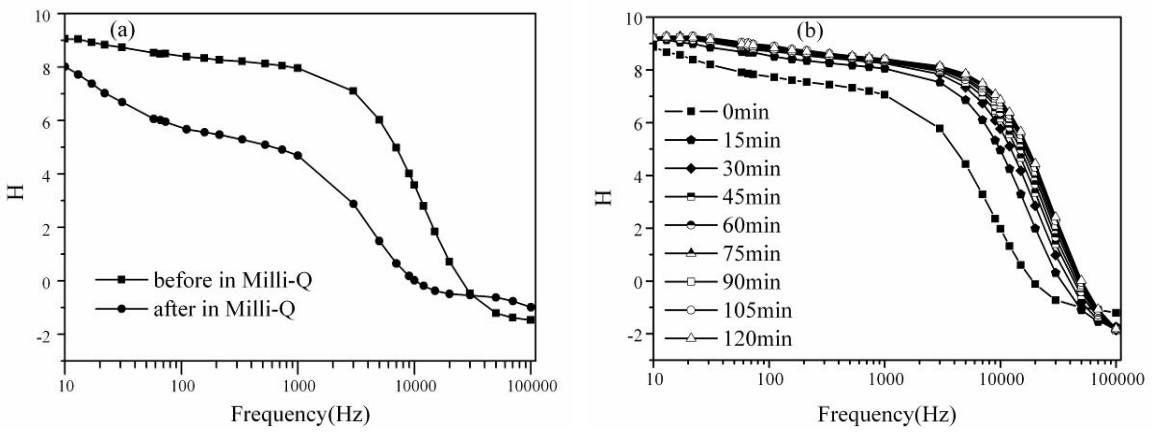

Fig 4.44 Ex-situ (a) and in-situ (b) transfer function of the reaction between streptavidin and biotin on the gate surface. Biotin was covalently immobilized as described in Chapter 4.1.4.

The ex-situ experiment was done in ultrapure water before and after the reaction, while the in-situ experiment was carried out with 1 mg/ml streptavidin in ultrapure water. As observed in Fig 4.44a, the transfer function curves shifted to the lower frequency range after the biotin/streptavidin binding. The binding of biotin and streptavidin caused a thickness increase, since the streptavidin layer thickness is about 5-6nm (Piehler et al. 1996). The capacitance change of a biomolecular layer either can be caused by a change in the dielectric constant (i.e. refractive index) or by a change of the thickness of the layer on the biosensor surface (Berggren et al. 2001). In this experiment, the refractive index for biotin and streptavidin can be treated the same (paragraph 3.2.3). If the density and the dielectric constant of the layers are the same, thicker layers will lead to a smaller capacitance. However, as shown in Fig 4.44a, the transfer function curve shifted to a lower frequency range related to a higher capacitance. A possible reason for this might be that in this pH value solution, the streptavidin molecule is beard negatively charged (Fernando Patolsky et al. 2005). The attachment of charges will lead to a higher capacitance (Landheer et al. 2005). Therefore, the superposition of both effects from these two opposite influences is resulting in a capacitance increase (Bergveld 1991a), and the transfer function curves shift to lower cut-off frequencies.

Considering the larger effect from the thickness and the related capacitance by the streptavidin, the capacitances for the biomembrane and the oxide layer were compared by the extracted time constants.

Table 4.13 Time constants extracted from the transfer function curves in Fig 4.44a

	$1/\tau_1$ (Hz)	$1/\tau_2$ (Hz)	$\frac{C_{mem}}{C_{ox}}(\frac{\tau_2}{\tau_1-\tau_2})$
Before binding	3575	30570	13.2 %
After binding	1405	11068	14.6 %

As shown in Table 4.13, the time constants were extracted form the Fig 4.44a. The capacitance ratios of C_{mem}/C_{ox} were compared before and after the binding reaction. The capacitance ratio increased from 13.2% to 14.6% after the biotin/streptavidin binding. The capacitance of membrane increased 1.5% compared with the oxide layer capacitance.

For the biotin/streptavidin reaction, also in-situ measurements in 1mg/ml streptavidin diluted in ultrapure water were carried out. The transfer functions were monitored every fifteen minutes. For the time-dependent measurement, we observed a quick equilibrium of the biotin-streptavidin binding in 30 minutes. In the in-situ plots (Fig 4.44b), an opposite direction of the transfer function shift was observed that with the time elapsed. The reason might be that the adsorption of streptavidin caused a local low resistance near the surface, thereby increasing the cut-off frequency of the ISFET (Bergveld 1991a). This phenomenon was previously explained by the Donnan effect (paragraph 2.2.3), which might be responsible for the recorded signals.

In summary, the DNA hybridization and the biotin/streptavidin binding were detected with the ISFET biosensors by the DC and AC readout. In the potentiometric, in-situ DNA immobilization and hybridization experiments the change of gate voltage corresponded to the covalent-binding of ssDNA and the specific hybridization process. Different hybridization efficiency for different sequences was distinguishable in the potentiometric measurements. However, the selectivity of these in-situ measurements was not high enough to enable a SNP detection. With the AC readout system and in an ex-situ assay, the SNPs were clearly detected. Furthermore, the detection of the binding of biotin and streptavidin on the modified biosensor surface was possible. The detection mechanism underlying the field-effect based sensing approach is still under discussion (Poghossian et

al. 2005). However, the change of the flatband voltage in DC readout and the change of the input impedance in AC readout are obviously caused by the biomolecules attachment. For a clear explanation of these results, more detailed experiments need to be done in the future.

Chapter V Conclusion and Outlook

ISFET biosensors with a semiconductor/SiO_2/electrolyte structure offered a platform for DNA hybridization and single nucleotide polymorphisms detections. Other studies including PEMs buildup and biotin/streptavidin binding were performed.

On the SiO_2 control substrates, surface modifications were carried out leading to the covalent binding of probe ssDNA and biotin. A series of surface modification reactions including cleaning/activation, silanization and crosslinking was successfully established, and each step was characterized with various surface anslytical methods. These involved Contact Angle (CA), Atomic Force Microscopy (AFM), Image Ellipsometry (IE), Fourier Transform Infra-Red (FT-IR) and X-Ray Photoelectron Spectroscopy (XPS). The standard surface modification was then a step-by-step protocol: firstly activation with a MeOH/HCl mixture for 30mins, and then secondly a silanization from vapor phase at 1m bar with aminopropyltriethoxysilane (APTES). Biotin molecules were covalently immobilized on the silanized surface directly. The biotin/streptavidin binding process was confirmed with XPS and AFM. The third step for covalent DNA immobilization was a crosslinking procedure, which was done with a succinic anhydride solution for 2 hours. The DNA position-specific microarrays for hybridization detection were made by a custom-made microspotter system. The microarray images were analyzed with fluorescence microscopy

and the software package ImageJ to extract brightness values of the spots. The results showed a higher efficiency of the DNA-DNA hybridization in higher ionic strength solution (SSC buffer solution) and higher selectivity for SNPs detection in TE buffer solutions. In contrast to this, the sandwich hybridization experiment was much dependent on the ionic strength of the buffer solution, similar to the hybridization efficiency know for free solutions.

All bioassay protocols were successfully transferred to the fully encapsulated ISFET devices and were “mild” enough for the encapsulation material of the chips. The DNA hybridization and the biotin/streptavidin binding were successfully detected with the ISFET biosensors in the terms of surface potential or input impedance change of the devices.

Before the label-free detection of the biological reactions, polyelectrolyte multilayer systems were used as model. The recordings of the multilayer buildup in AC and DC readouts modes offered details for the principle explanations of the signals and evidence about the main components in the equivalent circuit simulations. In the potentiometric readout assays, the in-situ buildup of the PEMs was monitored. The gate voltage signals change with the alternating adsorption of the oppositely charged PEs and ssDNA/PE layer systems. PEM systems are known to carry their total net charge at the upper layer/electrolyte interface. The recorded results confirmed the surface charge sensitivity and the surface enhanced detection of the ISFETs. With increasing distance away from the surface, the charge detection of the ISFETs is exponentially decreasing. Furthermore, the transfer functions curves of the PEMs buildup and their simulation with an equivalent circuit provided an identification of the main elements involved in the detection. The main parameters such as contact lane capacitance and solution resistance were firstly identified with the conductivity measurements. The influence of a biomembrane attached to the ISFET gate was in a first approximation modeled by a simple RC element.

In the following, probe DNA arrays and biotin were covalently immobilized on the modified ISFET transistor surfaces. The DNA hybridization reaction and the biotin/streptavidin binding were detected with the ISFET system in both the DC and the AC mode. To reduce the long-term drift of the readout and exclude side effects from temperature, pH changes, and buffer concentration changes etc., a reference chip or a reference channel were used to perform differential readout detection. The immobilization

of DNA in the differential potentiometric readout caused the gate voltage to decrease by 4mV. The difference of the DNA immobilization between covalent binding and electrostatic adsorption was distinguished. It was confirmed that the covalent binding of DNA probe molecules introduced a higher surface coverage to distinguish on the transistor surface compared to the electrostatic immobilization. The following hybridization experiment gave a clear signal between the PM and the FMM hybridizations. In contrast to this, the DC readout of the in-situ assay was not selective enough to enable SNPs detection.

Therefore, ISFETs as impedimetric biosensors with AC readout were developed in the timefreame of this thesis. In the ex-situ AC readout, the detection solutions were optimized. A reliable, successful recording of SNPs in low ionic strength detection solutions (0.01mM NaCl) was achieved. However, the adding of AuNPs to the target DNA did not enhance the selectivity of the SNPs detection. One interpretation would be that a steric hindrance during hybridizations decreases the hybridization efficiency of these assays. Furthermore, in-situ and ex-situ measurements of biotin/streptavidin binding reveal different effects on the transfer function curves. First experiments with these proteins were successful, but a deeper understanding of the effects so far can only be achieved by more experiment into this direction in future.

So far, the measurements represented in this thesis, showed the successful label-free and highly selective detection of SNPs and biotin/streptavidin binding with ISFET in both AC and DC mode. The detection mechanism underlying the field-effect based sensing approach is still under discussion (Poghossian et al. 2005). However, the change of the flatband voltage in DC readout and the charge of the input impedance in AC readout are obviously caused by the attachment of the biomolecules. For a clear explanation of these results, more detailed experiment need to be done in the future.

With the development of new biosensor chips, more experiments will be performed in the future. Optimizing the biosensor fabrication with on chip reference electrodes and fully encapsulated biosensors, by employing microfluidics to lower volume of the target molecule solution will increase the sensitivity of the assays. Additionally, alternative gate materials and nanoscale biosensors are also promising for future improvements of the sensors. More detailed Model simulations or analytical calculations will be needed to establish a fully, equivalent circuit to explain the detection principles.

Apart from the technological optimizations, different biological related experiments are also very interesting for the future development. Replacing the probe DNA with peptide nucleic acids (PNA) was recently presented in related works. PNA is made of an artificial backbone based on a peptide chain, and the four kinds of nucleotides can attach on it. The backbone is N-(2-aminoethyl) glycine, which carries no charge compared to the phosphate backbone of DNA. The PNA/DNA hybridization reaction has greater affinities than the DNA/DNA hybridization reaction. A PNA/DNA duplex with a SNP is less stable than the same SNP in the corresponding DNA/DNA duplex. Such assays would offer an even higher selectivity for SNP detections.

Based on the detection of the DNA hybridization and the biotin/streptavidin binding, other biological detections of cells, microorganisms, viruses and small molecule are possible to perform. Making use of the multi channel array design, DNA microarrays for DNA expression profiling, studying DNA variation, chromosome structure, DNA-protein interactions for functional exploration of genomes (Lamartine 2006) and in-situ PCR quantification (Hou et al. 2006) were presented and may possibly be adapted to the ISFET arrays.

Even multi probe arrays with mixed of DNA-DNA, DNA-protein, antibody-antigen reactions etc. might be detected with the ISFET in a single assay.

Appendices

A. Fabrication of the ISFET devices

The fabrication process of the p-channel FETs used in this thesis was previously (Offenhausser et al. 1997b; Sprossler et al. 1998). This design was further modified to lower series resistance of the contact lanes and smaller gate dimensions (Krause et al. 2000). The 16-channel and 8-channel chips were fabricated at the Institute for Micromechanics, Mainz, Germany.

Five lithography steps were involved to fabricate the biosensor wafer. The process started with a strong implantation for the contact lanes and a weaker implantation for the source and drain definition (both boron: 1st 100 keV, dose $5x10^{15}$; 2nd 80 keV, dose $1x10^{15}$). The gate area was then opened and the whole wafer was passivated against the electrolyte solution with an oxide-nitride-oxide stack (250 nm wet oxide, 130 nm LPCVD nitride and 100 nm PECVD silicon oxide). After deposition of the passivation layers, the gate was opened for a second time and a gate oxide was formed by oxidation in dry atmosphere (10 nm SiO_2 at 820°C). Finally, the bond pads were metallized (250 nm Al).

The transistor arrays consisted of 16 transistor (4×4) gates or 8 gates (2×4) with the dimensions of $5\times5mm^2$ and $2.5\times5mm^2$, respectively. Gate dimensions were 16/8×1.1.5/2 μm^2 (channel Length×Width), respectively. The gate spacing was 200µm and the gate oxide consisted of thermally grown SiO_2 in three different thicknesses 8, 10, or 12 nm. The sandwich layer of oxide-nitride-oxide (ONO) for passivation of the FET contact lanes was found to be stable for repeated use of the devices. For the 8-channel dip-chips the Al contacts pads were located on the opposite side of the chip, which enabled an encapsulation such that the chips can be dipped into any solution without touching the encapsulation material. The transconductance g_m of the FET chips range from 0.2 to 0.6 mS depending on gate size and oxide thickness.

The previously fabricated chip design was adapted to the cleanroom of the IBN at the Research Center Juelich in the timeframe of this thesis. Basic common source design, implantations and thickness of the passivation layer were adopted for the Juelich chip design. The gate dimension, however, were different: 100×1, 50×1, 25×1, and $12\times1\mu m^2$, respectively. The pitch of the gate array was 200 µm except for the 100µm design, which

Table A1 Process flow of P-channel FETs, which were fabricatied in the IBN cleanroom at the Research Center Juelich, Germany.

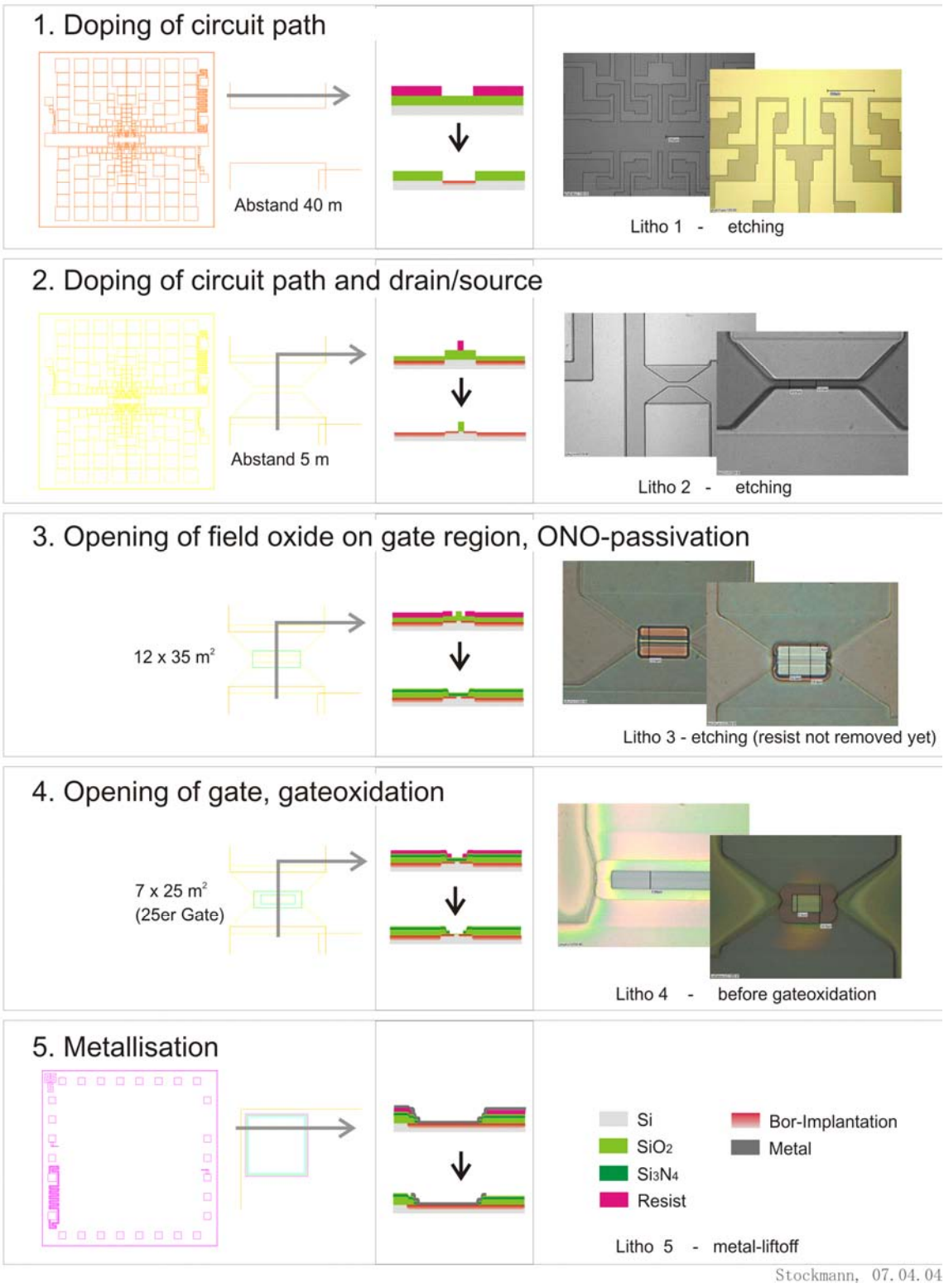

used a pitch of 500 µm. the former Al bond pads were exchanged to a Al/Ti/Au (200/10/100nm) metal stack to enable a flip-chip encapsulation of the devices. The process flow of the Juelich design is provided in Table A1 and the encapsulated chips are shown in Fig A1 and Fig A2.

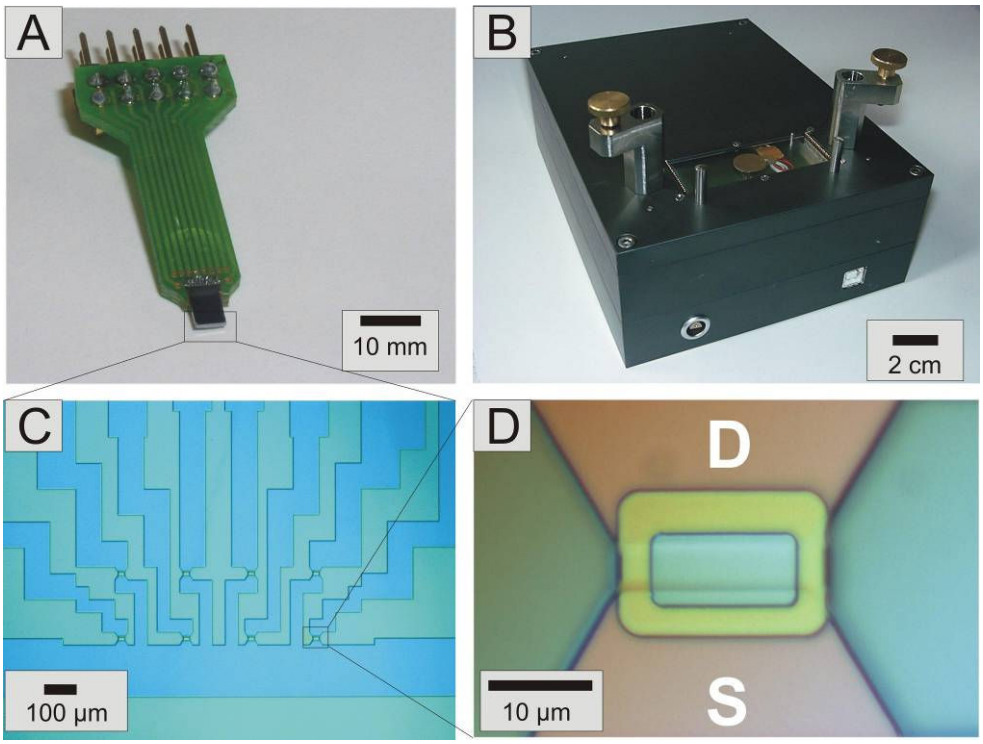

Fig A1 Third generation FET measurement system: A) fully encapsulated 8-channel FET chip, B) miniaturized, 16-channel FET amplifier, C) closer view to the 2x4 FET array (differential interference contrast microscopy (DIC)), and D) zoom to a single FET gate with individual drain (D) and common source (S) connections (Han et al. 2006b).

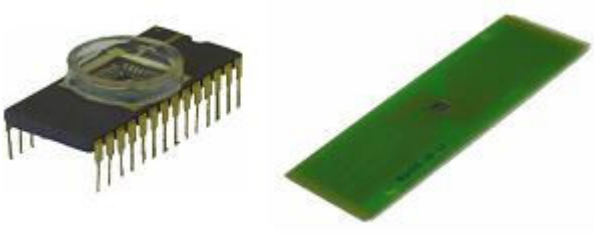

Fig A2 Photography of the two previous generations of FET biosensors also used in this work, which were both 16-channel FET biosensors. The sizes for the encapsulated chips are 3×1cm and 7.5×2.5cm, respectively.

The ISFET biosensors encapsulation starts from ultrasonication in ethanol/acetone (1/1) mixture to remove the protective photoresist layer from the chips. A two-component epoxy glue (H20E-PFC, Epoxy Technology Inc., USA) was applied to fix the chips on the carrier and the glue was cured in an oven for 30 minutes at 120^{o}C. Afterwards, two methods of connections between the chips and the carrier were achieved either by a front side wire

bonding technique (first and third generations) or a flip-chip encapsulation using a screen printer and a fineplacer unit (fineplacer 96 LAMBDA, FINTECH Gemany) (second generation). Passivation of the bond pads or flip-chip contacts was done with epoxy (Epo-tek U300, Polytec Inc, USA) or sylgard glue (Sylgard 96-083, DOW CORNING, USA), respectively. The extra last step for the third generations of biosensors (8-channel dip-chips) was a soldering of a pin connector to the backside of the carriers (Fig A1A).

B. Summary of four generation amplifiers

In the timeframe of this thesis, the development of the amplifiers went through four generations. The amplifiers are connected via USB cable and controlled by PC operations.

amplifier version	16-channel old	16-channel DC	16/8 channel DC 2 channel AC	16/8 channel DC/AC
ISFET characteristics	yes	yes	yes	yes
sampling frequency	1-10kHz	1Hz or10kHz	1Hz	1Hz or 10kHz
heading control	yes	yes	yes	heating and cooling
PC interface	DAC-card in PC	USB 1.0 N1 USB 6015	USB 1.0 N1 USB 6015	USB 1.0 N1 USB 6015 N1 6071E
transfer function	no	no	2 channels switching (operation~4min)	16 channels (operation~30s)
year	2003 (Uslu 2003; Uslu et al. 2004)	2004 (Ingebrandt et al. 2005)	2005 (Han et al. 2006b; Kottuppallil 2006; Sakkari 2005)	2006 (Ingebrandt et al. 2006)
differential reference	no	no	no	yes

C. Custom-made software for the ISFET detection

The different generations of measurement software were programmed in Delphi 5.0.

This software provided several functions:

1. Characterizations of an electronic chip (transfer and output characteristics, Fig A3)

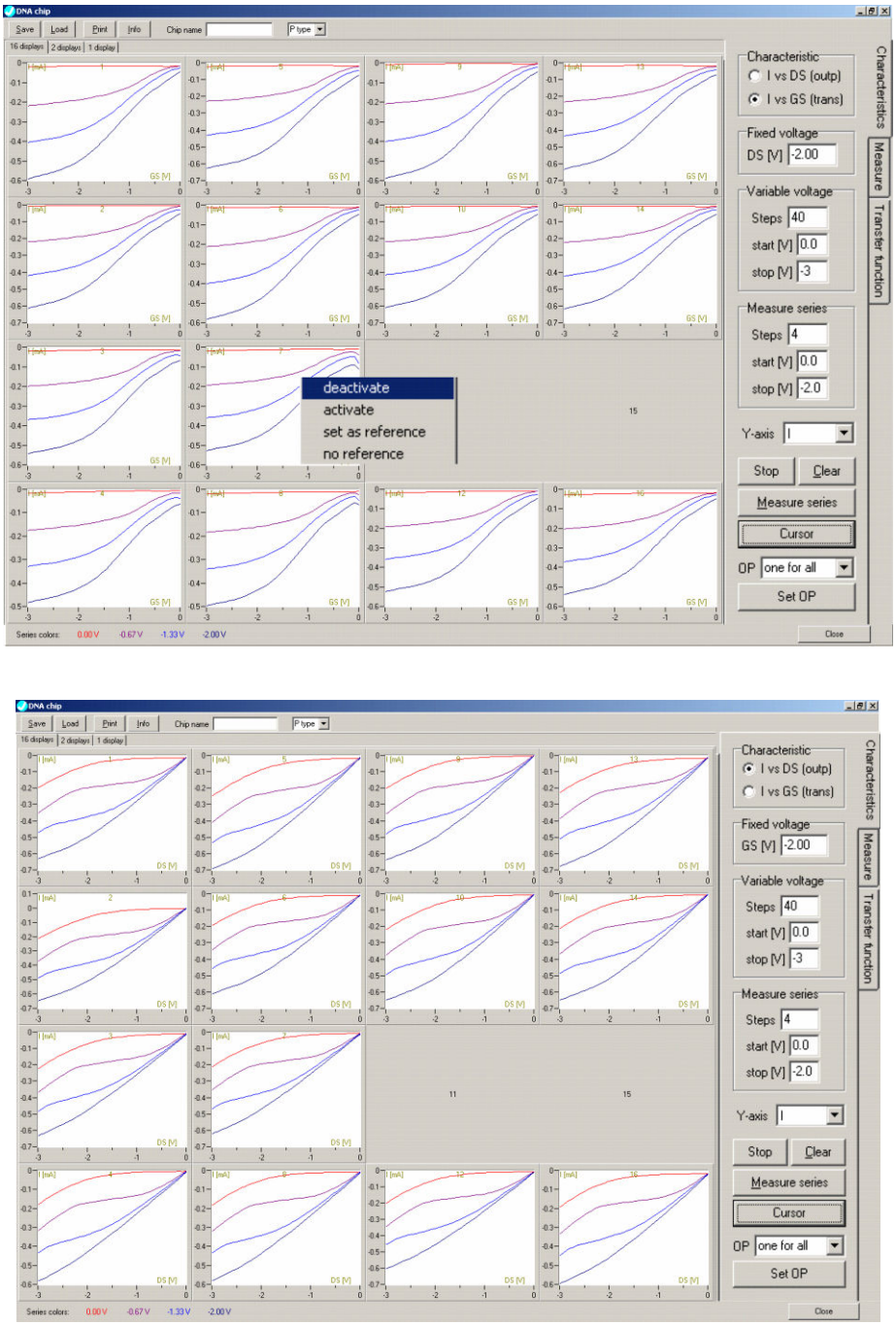

Fig A3 The transfer (upper) and output (below) characteristics of a 16-channel ISFET array used in this work

2. Numerical analysis of the transconductance (Fig A4).

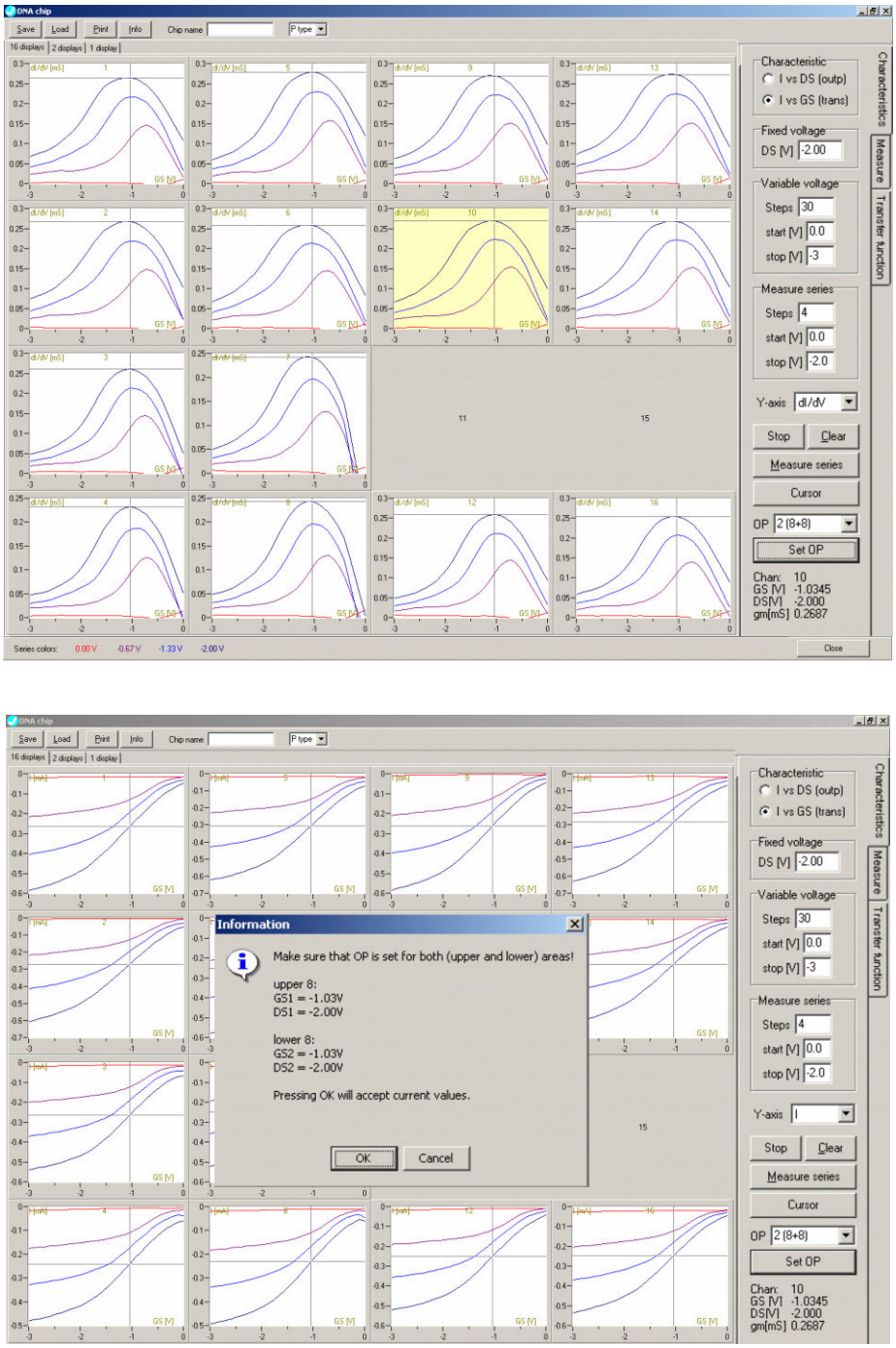

Fig A4 Transconductance curves of a 16-channel ISFET. Not working channels can be deactivated like channels 11 and 15 in this example.

With a movable cursor, the working point for all the transistors can be set prior the time dependent measurements. For 8-channel chips, the working points can be set differently for two chips at the same time. The output data are saved in ASCII format and can be imported i.e. to Origin (Origin 7.5 OriginLab Corporation, USA) for further analysis.

3. Time-dependent measurements

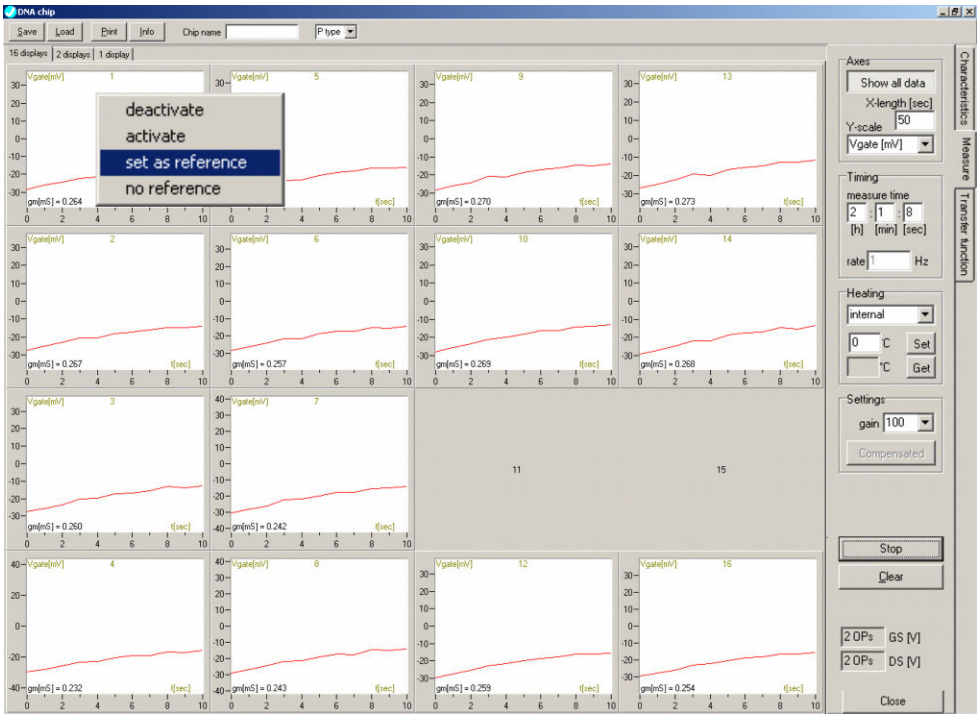

Fig A5 The software for the time-dependent measurements in the DC readout, and any channel from the array can be set as reference channel enabling a differential readout of the remaining channels.

For the time-dependent measurements, the drain-source and gate-source voltages are fixed and changes in the drain-source current are measured (constant voltage mode). In the tunable time, the Y scale could be selected as the change in the terms of gate voltage, drain current accordingly. Before the starting point of the measurements can be set as zero by compensation with the voltage input. The gains of the displaying signal are 1×, 10×, 30×, and 100×. During the measurements, the temperature control is precise from room temperature to 90^{o}C to assist the detections.

4. Transfer function frequency scan

For the transfer function scan at different frequency can be performed by this software, the output are displayed in either transconductance or amplifier output voltage values. Unwanted or broken channels can be turned off.

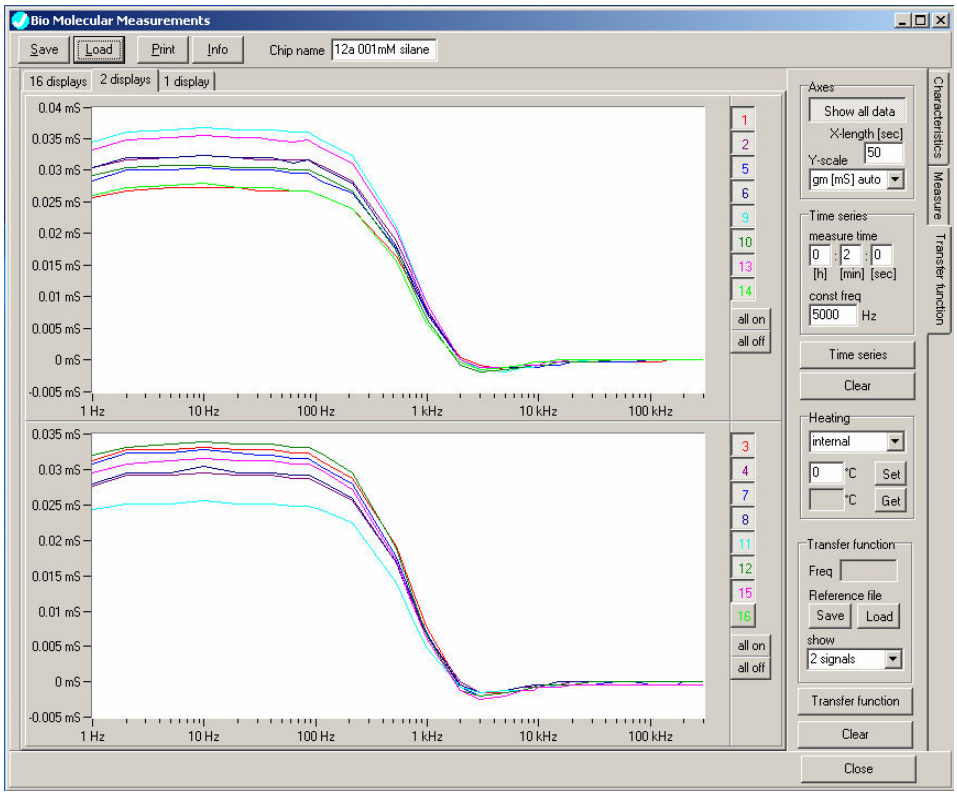

Fig A6 The software for the transfer function scan in the AC readout. The 16 channels from 16-channel chip or two 8-channel chips are recorded at the same time. The frequency range is from 10-10kHz.

5. Time-dependent frequency scan

The measurements measurement at a fixed frequency is also attained for the 16-channel arrays. At the selected frequency in the range of 10-10KHz, the change of the transconductance or the amplifier output voltage values with the time can be recorded.

D. List of reagent used in this thesis

All chemicals from Sigma-Aldrich were used without further purification, and all the oligonucleotides samples were purchased from MWG-Biotech AG, Germany.

Abbreviation	Full name	structure
APTES	(3-Aminopropyl)triethoxysilane	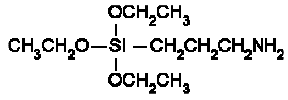
AcOH	Glacial acetic acid	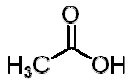
Biotin*	EZ-Link Sulfo-NHS-LC-Biotin (sulfosuccinimidyl-6-[biotinamido]hexanoate)	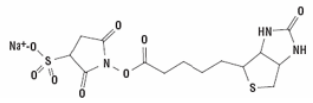
BSA	Bovine Serum Albumin	
Sodium citrate	Citric acid trisodium salt dihydrate	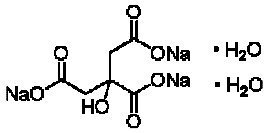
Cy3	Orange fluorescing Cyanine reagents	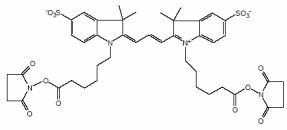
DPEA	N,N-Diisopropylethylamine	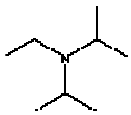
EDC	1-Ethyl-3-(3-dimethylaminopropyl) carbodiimide hydrochloride	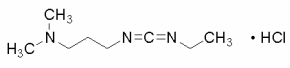
EDTA	Ethylenediaminetetraacetic acid	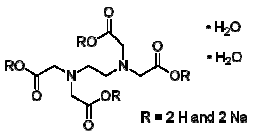
GPTES	(3-Glycidyloxypropyl) trimethoxysilane	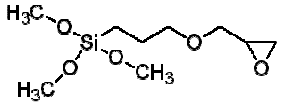

MES	4-Morpholineethanesulfonic acid monohydrate	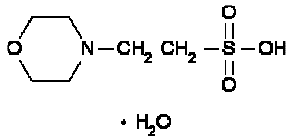
O-xylene	1,2-Dimethylbenzene	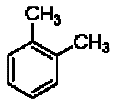
PAH	Poly (allylamine hydrochloride) 70,000 (M.W.)	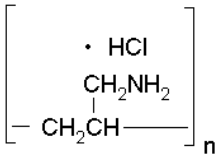
PBS	Phosphate Buffered Saline Buffer	$NaCl+KCl+Na_2HPO_4+KH_2PO_4$
PEI	Polyethylenimine 750,000 (M.W.)	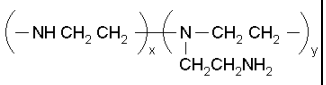
PSS	Poly (sodium 4-styrensulfonate) 70,000 (M.W.)	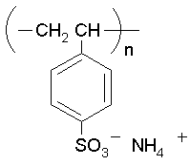
SSC buffer 20×concentrated		Sodium citrate+NaCl (3M)
Succinic anhydride	Dihydro-2, 5-furandione	
Streptavidin	Streptomyces Avidinii	
Titrisol**	Standard pH solutions (pH 1-10)	$C_6H_8O_7+NaOH+HCl$ $H_3BO_3+NaOH+KCl$
Tris	Tris (hydroxymethyl) amino methane	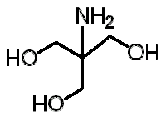

* Pierce Biotechnology, Inc., USA

** Merck KGaA, Germany

E. Recipes for buffers and different solutions

Silanization

APTES: in liquid phase, 5% in EtOH solution (V/V)

APTES: in gas phase, pure silane was utilized

GPTES: GPTES: oxylene: N,N-Diisopropylethylamine solution 25: 222: 3 (V: V: V)

Crosslinking

Succinic anhydride: 143 mM succinic anhydride in 87% 1-methyl-2-pyrrolidone and 13% sodium borate solution (V/V) with pH 7.04

DNA Immobilization buffer solution

MES buffer: 0.1 M MES in 0.5 M NaCl solution and 10 mg/ml EDC as condensing agent pH 7.0

Non-specific blocking solution

1% BSA in PBS

DNA Hybridization buffer solution

TE buffer: 10mM Tris, 1mM EDTA pH=8.0

SSC buffer: 4×SSC buffer solution (60mM sodium citrate, 600mM sodium chloride pH =7.0)

PE solution: 50μM in TE buffer with 0.01mM NaCl

Biotin immobilization

0.5mg/ml EZ-link Sulfo-NHS-LC-biotin in 10mM boric acid with pH 8.04

Streptavidin

1mg/ml streptavidin in Milli-Q water

AC detection solution

Different concentration NaCl solution from 0.01mM to 600mM

F. Standard protocols used in this thesis

Silanization

Silanization in gas phase, APTES few drops under approx. 1m bar for 1 hour

Crosslinking

In succinic anhydride for 2 hours and finally rinsing with Milli-Q water

DNA Immobilization

In immobilization buffer solution by overnight incubation at 37^{o}C

Non-specific hybridization blocking

2 hours at R.T.

DNA Hybridization

In hybridization buffer solution for 2 hours at R.T., sequentially rinsed with 2×SSC, 0.1×SSC and Milli-Q water

Biotin immobilization

In 0.5mg/ml biotin in boric acid (pH=8.04) for 1 hour and rinsing with Milli-Q water

Streptavidin

In streptavidin solution (1mg/ml) for 1 hour and ringsing with Milli-Q water

PEMs

Each layer was formed by immersion in PE solution for 20 minutes and rinsing with buffer solution

Reference

2006a, http://ece-www.colorado.edu/~bart/book/

2006b, http://www.uweb.engr.washington.edu/research/tutorials/contact.html

2006c, http://www.jawoollam.com/tutorial_1.html

2006d, http://www.azonano.com/details.asp?ArticleID=1258

2006e, http://rsb.info.nih.gov/ij/

2006f, http://www.uni-leipzig.de/~unifit/

2006g, http://srdata.nist.gov/xps/

2006h, http://www.microdrop.de/wDeutsch/products/md_series.shtml?navid=11

2006i,
http://www.roche-applied-science.com/PROD_INF/MANUALS/InSitu/InSi_toc.htm

Anderson, C. F. & Record, M. T. 1995, "Salt Nucleic-Acid Interactions", *Annual Review of Physical Chemistry*, vol. 46, pp. 657-700

Antonisse, M. M. G., Snellink-Ruel, B. H. M., Lugtenberg, R. J. W., Engbersen, J. F. J., van den Berg, A., & Reinhoudt, D. N. 2000, "Membrane characterization of anion-selective CHEMFETs by impedance spectroscopy", *Analytical Chemistry*, vol. 72, no. 2, pp. 343-348

Armstrong, R. D. & Horvai, G. 1990, "Properties of Pvc Based Membranes Used in Ion-Selective Electrodes", *Electrochimica Acta*, vol. 35, no. 1, pp. 1-7

Audesirk, Teresa, Audesirk, Gerald, and Byers, Bruce E.2005"Biology : life on Earth, seventh edition : student study companion"Upper Saddle River, NJ : Prentice Hall

Aydil, E. S., Gottscho, R. A., & Chabal, Y. J. 1994, "Real-Time Monitoring of Surface-Chemistry During Plasma Processing", *Pure and Applied Chemistry*, vol. 66, no. 6, pp. 1381-1388

Bain, C. D., Evall, J., & Whitesides, G. M. 1989a, "Formation of Monolayers by the Coadsorption of Thiols on Gold - Variation in the Head Group, Tail Group, and Solvent", *Journal of the American Chemical Society*, vol. 111, no. 18, pp. 7155-7164

Bain, C. D., Troughton, E. B., Tao, Y. T., Evall, J., Whitesides, G. M., & Nuzzo, R. G. 1989b, "Formation of Monolayer Films by the Spontaneous Assembly of Organic Thiols from Solution Onto Gold", *Journal of the American Chemical Society*, vol. 111, no. 1, pp. 321-335

Bain, C. D. & Whitesides, G. M. 1988, "Correlations Between Wettability and Structure in Monolayers of Alkanethiols Adsorbed on Gold", *Journal of the American Chemical Society*, vol. 110, no. 11, pp. 3665-3666

Balachander, N. & Sukenik, C. N. 1990, "Monolayer Transformation by Nucleophilic-Substitution - Applications to the Creation of New Monolayer Assemblies", *Langmuir*, vol. 6, no. 11, pp. 1621-1627

Balladur, V., Theretz, A., & Mandrand, B. 1997, "Determination of the main forces driving DNA oligonucleotide adsorption onto aminated silica wafers", *Journal of Colloid and Interface Science*, vol. 194, no. 2, pp. 408-418

Barbaro, M., Bonfiglio, A., & Raffo, L. 2006, "A charge-modulated FET for detection of biomolecular processes: Conception, modeling, and simulation", *Ieee Transactions on Electron Devices*, vol. 53, no. 1, pp. 158-166

Barrat, J. L. & Joanny, J. F. 1996, "Theory of polyelectrolyte solutions", *Advances in Chemical Physics, Vol Xciv*, vol. 94, pp. 1-66

Barres, O., Burneau, A., Dubessy, J., & Pagel, M. 1987, "Application of Micro-Ft-Ir Spectroscopy to Individual Hydrocarbon Fluid Inclusion Analysis", *Applied Spectroscopy*, vol. 41, no. 6, pp. 1000-1008

Bataillard, P., Clechet, P., JaffrezicRenault, N., Kong, X. G., & Martelet, C. 1987, "The Preparation of Chemfet Selective Gates by Thin Silica Layer Grafting and Their Behavior", *Sensors and Actuators*, vol. 12, no. 3, pp. 245-254

Bayer, E. A. & Wilchek, M. 1990, "Application of Avidin Biotin Technology to Affinity-Based Separations", *Journal of Chromatography*, vol. 510, pp. 3-11

Bekiari, V. & Lianos, P. 1998, "Characterization of photoluminescence from a material made by interaction of (3-aminopropyl)triethoxysilane with acetic acid", *Langmuir*, vol. 14, no. 13, pp. 3459-3461

Berggren, C., Bjarnason, B., & Johansson, G. 2001, "Capacitive biosensors", *Electroanalysis*, vol. 13, no. 3, pp. 173-180

Bergna, H. E. 1990, "Dense Silica Coatings on Micro and Nanoparticles by Deposition of Monosilicic Acid", *Abstracts of Papers of the American Chemical Society*, vol. 200, p. 207-COLL

Bergveld, P. 1991a, "A Critical-Evaluation of Direct Electrical Protein-Detection Methods", *Biosensors & Bioelectronics*, vol. 6, no. 1, pp. 55-72

Bergveld, P. 1991b, "Future Applications of Isfets", *Sensors and Actuators B-Chemical*, vol. 4, no. 1-2, pp. 125-133

Bergveld, P. 1996, "The future of biosensors", *Sensors and Actuators A-Physical*, vol. 56, no. 1-2, pp. 65-73

Bergveld, P. 2003, "Thirty years of ISFETOLOGY - What happened in the past 30 years and what may happen in the next 30 years", *Sensors and Actuators B-Chemical*, vol. 88, no. 1, pp. 1-20

Bergveld, P., Eijkel, J. C. T., & Olthuis, W. 1997, "Detection of protein concentrations with chronopotentiometry", *Biosensors & Bioelectronics*, vol. 12, no. 9-10, pp. 905-916

Bergveld, P., Vandenberg, A., Vanderwal, P. D., Skowronskaptasinska, M., Sudholter, E. J. R., & Reinhoudt, D. N. 1989, "How Electrical and Chemical-Requirements for Refets May Coincide", *Sensors and Actuators*, vol. 18, no. 3-4, pp. 309-327

Bertrand, P., Jonas, A., Laschewsky, A., & Legras, R. 2000, "Ultrathin polymer coatings by complexation of polyelectrolytes at interfaces: suitable materials, structure and properties", *Macromolecular Rapid Communications*, vol. 21, no. 7, pp. 319-348

Bezanilla, M., Manne, S., Laney, D. E., Lyubchenko, Y. L., & Hansma, H. G. 1995, "Adsorption of Dna to Mica, Silylated Mice, and Minerals - Characterization by Atomic-Force Microscopy", *Langmuir*, vol. 11, no. 2, pp. 655-659

Binnig, G., Quate, C. F., & Gerber, C. 1986, "Atomic Force Microscope", *Physical Review Letters*, vol. 56, no. 9, pp. 930-933

Bolton, E. T. & Mccarthy, B. J. 1962, "A General Method for Isolation of Rna Complementary to Dna", *Proceedings of the National Academy of Sciences of the United States of America*, vol. 48, no. 8, p. 1390-&

Bordi, F., Cametti, C., & Colby, R. H. 2004, "Dielectric spectroscopy and conductivity of polyelectrolyte solutions", *Journal of Physics-Condensed Matter*, vol. 16, no. 49, p. R1423-R1463

Borstlap, D.Dissertation, "High-k Dielectrics as Bioelectronic Interface for Field-Effect Transistors", RWTH Aachen University (2006)

Bosio, V., Dubreuil, F., Bogdanovic, G., & Fery, A. 2004, "Interactions between silica surfaces coated by polyelectrolyte multilayers in aqueous environment: comparison between precursor and multilayer regime", *Colloids and Surfaces A-Physicochemical and Engineering Aspects*, vol. 243, no. 1-3, pp. 147-155

Bousse, L. 1982, "Single Electrode-Potentials Related to Flat-Band Voltage Measurements on Eos and Mos Structures", *Journal of Chemical Physics*, vol. 76, no. 10, pp. 5128-5133

Bousse, L. & Bergveld, P. 1983, "On the Impedance of the Silicon Dioxide Electrolyte Interface", *Journal of Electroanalytical Chemistry*, vol. 152, no. 1-2, pp. 25-39

Breimer, M. A., Gelfand, Y., & Sadik, O. A. 2003, "Integrated capillary fluorescence DNA biosensor", *Biosensors & Bioelectronics*, vol. 18, no. 9, pp. 1135-1147

Breslauer, K. J., Frank, R., Blocker, H., & Marky, L. A. 1986, "Predicting Dna Duplex Stability from the Base Sequence", *Proceedings of the National Academy of Sciences of the United States of America*, vol. 83, no. 11, pp. 3746-3750

Bucher, V., Graf, M., Stelzle, M., & Nisch, W. 1999, "Low-impedance thin-film polycrystalline silicon microelectrodes for extracellular stimulation and recording", *Biosensors & Bioelectronics*, vol. 14, no. 7, pp. 639-649

Bullock, Gillian R. and Petrusz, Peter1983"Techniques in immunocytochemistry"London : Academic Press

Buzea, C. & Robbie, K. 2005, "State of the art in thin film thickness and deposition rate monitoring sensors", *Reports on Progress in Physics*, vol. 68, no. 2, pp. 385-409

Cai, W., Peck, J. R., van der Weide, D. W., & Hamers, R. J. 2004, "Direct electrical detection of hybridization at DNA-modified silicon surfaces", *Biosensors & Bioelectronics*, vol. 19, no. 9, pp. 1013-1019

Caruso, F., Niikura, K., Furlong, D. N., & Okahata, Y. 1997, "Assembly of alternating polyelectrolyte and protein multilayer films for immunosensing .2", *Langmuir*, vol. 13, no. 13, pp. 3427-3433

Chaiet, L. & Wolf, F. J. 1964, "Properties of Streptavidin Biotin-Binding Protein Produced by Streptomycetes", *Archives of Biochemistry and Biophysics*, vol. 106, no. 1-3, p. 1-&

Chodanowski, P. & Stoll, S. 1999, "Monte Carlo simulations of hydrophobic polyelectrolytes: Evidence of complex configurational transitions", *Journal of Chemical Physics*, vol. 111, no. 13, pp. 6069-6081

Chrisey, L. A., Lee, G. U., & OFerrall, C. E. 1996, "Covalent attachment of synthetic DNA to self-assembled monolayer films", *Nucleic Acids Research*, vol. 24, no. 15, pp. 3031-3039

Collings, A. F. & Caruso, F. 1997, "Biosensors: recent advances", *Reports on Progress in Physics*, vol. 60, no. 11, pp. 1397-1445

Cras, J. J., Rowe-Taitt, C. A., Nivens, D. A., & Ligler, F. S. 1999, "Comparison of chemical cleaning methods of glass in preparation for silanization", *Biosensors & Bioelectronics*, vol. 14, no. 8-9, pp. 683-688

Creeth, J. M. & Jordan, D. O. 1949, "Deoxypentose Nucleic Acids .5. An Attempted Interpretation of the Electrophoretic Mobilities of the Deoxypentose Nucleic Acid of Calf Thymus", *Journal of the Chemical Society* no. JUN, pp. 1409-1413

Dautzenberg, H.1994"Polyelectrolytes : formation, characterization, and application"Munich : Hanser

Decher, G. 1997, "Fuzzy nanoassemblies: Toward layered polymeric multicomposites", *Science*, vol. 277, no. 5330, pp. 1232-1237

Decher, G., Eckle, M., Schmitt, J., & Struth, B. 1998, "Layer-by-layer assembled multicomposite films", *Current Opinion in Colloid & Interface Science*, vol. 3, no. 1, pp. 32-39

Decher, G., Hong, J. D., & Schmitt, J. 1992, "Buildup of Ultrathin Multilayer Films by A Self-Assembly Process .3. Consecutively Alternating Adsorption of Anionic and Cationic Polyelectrolytes on Charged Surfaces", *Thin Solid Films*, vol. 210, no. 1-2, pp. 831-835

Decher, Gero and Schlenoff, Joseph B.2003"Multilayer thin films : sequential assembly of nanocomposite materials"Weinheim ; Chichester : Wiley-VCH

Defeijter, J. A., Benjamins, J., & Veer, F. A. 1978, "Ellipsometry As A Tool to Study Adsorption Behavior of Synthetic and Biopolymers at Air-Water-Interface", *Biopolymers*, vol. 17, no. 7, pp. 1759-1772

Demoz, A., Verpoorte, E. M. J., & Harrison, D. J. 1995, "An Equivalent-Circuit Model of Ion-Selective Membrane Broken-Vertical-Bar Insulator Broken-Vertical-Bar Semiconductor Interfaces Used for Chemical Sensors", *Journal of Electroanalytical Chemistry*, vol. 389, no. 1-2, pp. 71-78

Diamandis, E. P. & Christopoulos, T. K. 1991, "The Biotin (Strept)Avidin System - Principles and Applications in Biotechnology", *Clinical Chemistry*, vol. 37, no. 5, pp. 625-636

Diot, J. L., Joseph, J., Martin, J. R., & Clechet, P. 1985, "Ph-Dependence of the Si/Sio2 Interface State Density for Eos Systems - Quasi-Static and Ac Conductance Methods", *Journal of Electroanalytical Chemistry*, vol. 193, no. 1-2, pp. 75-88

Dobrynin, A. V. & Rubinstein, M. 2005, "Theory of polyelectrolytes in solutions and at surfaces", *Progress in Polymer Science*, vol. 30, no. 11, pp. 1049-1118

Dobrynin, A. V., Rubinstein, M., & Obukhov, S. P. 1996, "Cascade of transitions of polyelectrolytes in poor solvents", *Macromolecules*, vol. 29, no. 8, pp. 2974-2979

Dong, Y., Pappu, S. V., & Xu, Z. 1998, "Detection of local density distribution of isolated silanol groups on planar silica surfaces using nonlinear optical molecular probes", *Analytical Chemistry*, vol. 70, no. 22, pp. 4730-4735

Dubas, S. T. & Schlenoff, J. B. 2001, "Swelling and smoothing of polyelectrolyte multilayers by salt", *Langmuir*, vol. 17, no. 25, pp. 7725-7727

Duman, M., Saber, R., & Piskin, E. 2003, "A new approach for immobilization of oligonucleotides onto piezoelectric quartz crystal for preparation of a nucleic acid sensor for following hybridization", *Biosensors & Bioelectronics*, vol. 18, no. 11, pp. 1355-1363

Felsenfe, G. & Miles, H. T. 1967, "Physical and Chemical Properties of Nucleic Acids", *Annual Review of Biochemistry*, vol. 36, p. 407-&

Fernando Patolsky & Charles M.Lieber 2005, "Nanowire nanosensors", *Materialstoday*, vol. April, pp. 20-28

Flanagan, M. T. & Pantell, R. H. 1984, "Surface-Plasmon Resonance and Immunosensors", *Electronics Letters*, vol. 20, no. 23, pp. 968-970

Ford, W. E. & Tollin, G. 1982, "Direct Observation of Electron-Transfer Across A Lipid Bilayer - Pulsed Laser Photolysis of An Asymmetric Vesicle System Containing Chlorophyll, Methyl Viologen and Edta", *Photochemistry and Photobiology*, vol. 35, no. 6, pp. 809-819

Forster, S. & Schmidt, M. 1995, "Polyelectrolytes in Solution", *Physical Properties of Polymers*, vol. 120, pp. 51-133

Fritz, J., Cooper, E. B., Gaudet, S., Sorger, P. K., & Manalis, S. R. 2002, "Electronic detection of DNA by its intrinsic molecular charge", *Proceedings of the National Academy of Sciences of the United States of America*, vol. 99, no. 22, pp. 14142-14146

Fung, C. D., Cheung, P. W., & Ko, W. H. 1986, "A Generalized Theory of An "Electrolyte-Insulator-Semiconductor Field-Effect Transistor", *Ieee Transactions on Electron Devices*, vol. 33, no. 1, pp. 8-18

Gong, H. F., Garcia-Turiel, J., Vasilev, K., & Vinogradova, O. I. 2005, "Interaction and adhesion properties of polyelectrolyte multilayers", *Langmuir*, vol. 21, no. 16, pp. 7545-7550

Green, W. H., Le, K. P., Grey, J., Au, T. T., & Sailor, M. J. 1997, "White phosphors from a silicate-carboxylate sol-gel precursor that lack metal activator ions", *Science*, vol. 276, no. 5320, pp. 1826-1828

Gu, H. R., di Su, X., & Loh, K. P. 2005, "Electrochemical impedance sensing of DNA hybridization on conducting polymer film-modiried diamond", *Journal of Physical Chemistry B*, vol. 109, no. 28, pp. 13611-13618

Haller, I. 1978, "Covalently Attached Organic Monolayers on Semiconductor Surfaces", *Journal of the American Chemical Society*, vol. 100, no. 26, pp. 8050-8055

Hammond, P. T. 1999, "Recent explorations in electrostatic multilayer thin film assembly", *Current Opinion in Colloid & Interface Science*, vol. 4, no. 6, pp. 430-442

Han, Y., Mayer, D., Offenhausser, A., & Ingebrandt, S. 2006a, "Surface activation of thin silicon oxides by wet cleaning and silanization", *Thin Solid Films*, vol. 510, no. 1-2, pp. 175-180

Han, Y., Offenhausser, A., & Ingebrandt, S. 2006b, "Detection of DNA hybridization by a field-effect transistor with covalently attached catcher molecules", *Surface and Interface Analysis*, vol. 38, no. 4, pp. 176-181

Han, Y. H. & Lin, J. 2003, "Luminescence and energy transfer of organically modified silica xerogels (OMSX) doped and undoped with Eu3+ and Tb3+", *Journal of Solid State Chemistry*, vol. 171, no. 1-2, pp. 396-400

Haussling, L., Ringsdorf, H., Schmitt, F. J., & Knoll, W. 1991, "Biotin-Functionalized Self-Assembled Monolayers on Gold - Surface-Plasmon Optical Studies of Specific Recognition Reactions", *Langmuir*, vol. 7, no. 9, pp. 1837-1840

Hnatowich, D. J., Virzi, F., & Rusckowski, M. 1987, "Investigations of Avidin and Biotin for Imaging Applications", *Journal of Nuclear Medicine*, vol. 28, no. 8, pp. 1294-1302

Holm, C., Joanny, J. F., Kremer, K., Netz, R. R., Reineker, P., Seidel, C., Vilgis, T. A., & Winkler, R. G. 2004, "Polyelectrolyte theory", *Polyelectrolytes with Defined Molecular Architecture Ii*, vol. 166, pp. 67-111

Hou, C. S. J., Milovic, N., Godin, M., Russo, P. R., Chakrabarti, R., & Manalis, S. R. 2006, "Label-free microelectronic PCR quantification", *Analytical Chemistry*, vol. 78, no. 8, pp. 2526-2531

Huizenga, J. R., Grieger, P. F., & Wall, F. T. 1950, "Electrolytic Properties of Aqueous Solutions of Polyacrylic Acid and Sodium Hydroxide .1. Transference Experiments Using Radioactive Sodium", *Journal of the American Chemical Society*, vol. 72, no. 6, pp. 2636-2642

Inczedy, J., Inczedy, Jan, Lengyel, Ta, s, Ure, A, ., Freiser, He, y, and International Union of Pure and Applied Chemis1998"Compendium of analytical nomenclature : definitive rules 1997"3rd ed / prepared for publication by Janos Inczedy, Tamas Lengyel, Allan M. Ure / with the assistance of Andras Gelencser and cooperation of Adam HulanickiOxford : Blackwell Science

Ingebrandt, S.Dissertation, "Characterisation of the cell-transistor coupling", University Mainz, Germany (2001)

Ingebrandt, S., Han, Y., Nakamura, F., & Offenhausser, A. 2006, "Label-free DNA detection utilizing the differential transfer function of field-effect transistors", *Biosensors & Bioelectronics*

Ingebrandt, S., Han, Y. H., Sakkari, M. R., Stockmann, R., Belinskyy, O., & Offenhausser, A. "Electronic detection of nucleic acid molecules with a field-effect transistor", Materials Research Society, Warrendale, pp. 307-312.

Ingebrandt, S., Yeung, C. K., Krause, M., & Offenhausser, A. 2001, "Cardiomyocyte-transistor-hybrids for sensor application", *Biosensors & Bioelectronics*, vol. 16, no. 7-8, pp. 565-570

Ingebrandt, S., Yeung, C. K., Staab, W., Zetterer, T., & Offenhausser, A. 2003, "Backside contacted field effect transistor array for extracellular signal recording", *Biosensors & Bioelectronics*, vol. 18, no. 4, pp. 429-435

Israelachvili, J. & Drummond, C. 1999, "Time- and distance-dependent molecular rearrangements at shearing junctions", *Abstracts of Papers of the American Chemical Society*, vol. 217, p. U585

Ito, E., Nakamura, F., Kanai, K., Ouchi, Y., Seki, K., & Hara, M. 2006, "Characterization of COOH-terminated self-assembled monolayers and adsorption efficiency of DNA molecules studied by X-ray photoelectron Spectroscopy and near-edge X-ray absorption fine structure spectroscopy", *Japanese Journal of Applied Physics Part 1-Regular Papers Brief Communications & Review Papers*, vol. 45, no. 1B, pp. 409-412

Jakobson, C. G., Feinsod, M., & Nemirovsky, Y. 2000, "Low frequency noise and drift in Ion Sensitive Field Effect Transistors", *Sensors and Actuators B-Chemical*, vol. 68, no. 1-3, pp. 134-139

Jal, P. K., Patel, S., & Mishra, B. 2004, "Chemical modification of silica surface by immobilization of functional groups for extractive concentration of metal ions", *Talanta*, vol. 62, no. 5, pp. 1005-1028

Jamasb, S. 2004, "An analytical technique for counteracting drift in ion-selective field effect transistors (ISFETs)", *Ieee Sensors Journal*, vol. 4, no. 6, pp. 795-801

Jamasb, S., Collins, S., & Smith, R. L. 1998, "A physical model for drift in pH ISFETs", *Sensors and Actuators B-Chemical*, vol. 49, no. 1-2, pp. 146-155

Kalofonos, H. P., Rusckowski, M., Siebecker, D. A., Sivolapenko, G. B., Snook, D., Lavender, J. P., Epenetos, A. A., & Hnatowich, D. J. 1990, "Imaging of Tumor in Patients with Indium-111-Labeled Biotin and Streptavidin-Conjugated Antibodies - Preliminary Communication", *Journal of Nuclear Medicine*, vol. 31, no. 11, pp. 1791-1796

Katz, E. & Willner, I. 2003, "Probing biomolecular interactions at conductive and semiconductive surfaces by impedance spectroscopy: Routes to impedimetric immunosensors, DNA-Sensors, and enzyme biosensors", *Electroanalysis*, vol. 15, no. 11, pp. 913-947

Kern, W. & Puotinen, D. A. 1970, "Cleaning Solutions Based on Hydrogen Peroxide for Use in Silicon Semiconductor Technology", *Rca Review*, vol. 31, no. 2, p. 187-&

Kharitonov, A. B., Wasserman, J., Katz, E., & Willner, I. 2001, "The use of impedance spectroscopy for the characterization of protein-modified ISFET devices: Application of the method for the analysis of biorecognition processes", *Journal of Physical Chemistry B*,

vol. 105, no. 19, pp. 4205-4213

Kharitonov, A. B., Zayats, M., Lichtenstein, A., Katz, E., & Willner, I. 2000, "Enzyme monolayer-functionalized field-effect transistors for biosensor applications", *Sensors and Actuators B-Chemical*, vol. 70, no. 1-3, pp. 222-231

Kim, C. K., Chung, C. H., & Moon, S. H. 1996, "Removal of organic impurities from the silicon surface by oxygen and UV cleaning", *Korean Journal of Chemical Engineering*, vol. 13, no. 3, pp. 328-330

Kim, D. S., Jeong, Y. T., Park, H. J., Shin, J. K., Choi, P., Lee, J. H., & Lim, G. 2004a, "An FET-type charge sensor for highly sensitive detection of DNA sequence", *Biosensors & Bioelectronics*, vol. 20, no. 1, pp. 69-74

Kim, D. S., Park, H. J., Jung, H. M., Shin, J. K., Choi, P., Lee, J. H., & Lim, G. 2004c, "Field effect transistor-based bimolecular sensor employing a Pt reference electrode for the detection of deoxyribonucleic acid sequence", *Japanese Journal of Applied Physics Part 1-Regular Papers Short Notes & Review Papers*, vol. 43, no. 6B, pp. 3855-3859

Kim, D. S., Park, H. J., Jung, H. M., Shin, J. K., Choi, P., Lee, J. H., & Lim, G. 2004b, "Field effect transistor-based bimolecular sensor employing a Pt reference electrode for the detection of deoxyribonucleic acid sequence", *Japanese Journal of Applied Physics Part 1-Regular Papers Short Notes & Review Papers*, vol. 43, no. 6B, pp. 3855-3859

Kolarik, L., Furlong, D. N., Joy, H., Struijk, C., & Rowe, R. 1999, "Building assemblies from high molecular weight polyelectrolytes", *Langmuir*, vol. 15, no. 23, pp. 8265-8275

Kottuppallil, M. M.Dissertation, "Detection of bio-molecular recognition reactions at the solid-liquid interface utilizing the ISFET transfer function", Aachen University of Applied Sciences, Campus Juelich, Germany (2006)

Krause, M., Ingebrandt, S., Richter, D., Denyer, M., Scholl, M., Sprossler, C., & Offenhausser, A. 2000, "Extended gate electrode arrays for extracellular signal recordings", *Sensors and Actuators B-Chemical*, vol. 70, no. 1-3, pp. 101-107

Kruise, J., Rispens, J. G., Bergveld, P., Kremer, F. J. B., Starmans, D., Haak, J. R., Feijen, J., & Reinhoudt, D. N. 1992, "Detection of Charged Proteins by Means of Impedance Measurements", *Sensors and Actuators B-Chemical*, vol. 6, no. 1-3, pp. 101-105

Krull, U. J., Thompson, M., & Wong, H. E. 1986, "Chemical Modification of the Bilayer Lipid-Membrane Biosensor Dipolar Potential", *Bioelectrochemistry and Bioenergetics*, vol. 15, no. 3, pp. 371-382

Kuhn, W., Kunzle, O., & Katchalsky, A. 1948, "Verhalten Polyvalenter Fadenmolekelionen in Losung", *Helvetica Chimica Acta*, vol. 31, no. 7, pp. 1994-2037

Kumar, P., Choithani, J., & Gupta, K. C. 2004, "Construction of oligonucleotide arrays on a glass surface using a heterobifunctional reagent,

N-(2-trifluoroethanesulfonatoethyl)-N-(methyl)-triethoxysilylpropyl-3-am ine (NTMTA)", *Nucleic Acids Research*, vol. 32, no. 10,

Kurth, D. G. & Bein, T. 1993, "Surface-Reactions on Thin-Layers of Silane Coupling Agents", *Langmuir*, vol. 9, no. 11, pp. 2965-2973

Lahav, M., Kharitonov, A. B., & Willner, I. 2001, "Imprinting of chiral molecular recognition sites in thin TiO2 films associated with field-effect transistors: Novel functionalized devices for chiroselective and chirospecific analyses", *Chemistry-a European Journal*, vol. 7, no. 18, pp. 3992-3997

Lahiri, J., Isaacs, L., Tien, J., & Whitesides, G. M. 1999, "A strategy for the generation of surfaces presenting ligands for studies of binding based on an active ester as a common reactive intermediate: A surface plasmon resonance study", *Analytical Chemistry*, vol. 71, no. 4, pp. 777-790

Lamartine, J. 2006, "The benefits of DNA microarrays in fundamental and applied bio-medicine", *Materials Science & Engineering C-Biomimetic and Supramolecular Systems*, vol. 26, no. 2-3, pp. 354-359

Landheer, D., Aers, G., McKinnon, W. R., Deen, M. J., & Ranuarez, J. C. 2005, "Model for the field effect from layers of biological macromolecules on the gates of metal-oxide-semiconductor transistors", *Journal of Applied Physics*, vol. 98, no. 4,

Lide, David R.2004"CRC handbook of chemistry and physics : a ready refererence book of chemical and physical data"85th ed.Boca Raton, FL. ; London : CRC

Lide, David R., Milne, George W. A., and Chemical Rubber Company1994"Handbook of data on organic compounds"3rd edBoca Raton ; London : CRC Press

Lim, S. W. 2003, "Control of SC1 wet cleaning process for nano-scale gate oxide integrity", *Japanese Journal of Applied Physics Part 1-Regular Papers Short Notes & Review Papers*, vol. 42, no. 8, pp. 5002-5009

Loffler, U., Wiemhofer, H. D., & Gopel, W. 1991, "Amperometric Biosensors - Characterization of Dispersed Mediator Systems", *Biosensors & Bioelectronics*, vol. 6, no. 4, pp. 343-352

Losche, M., Schmitt, J., Decher, G., Bouwman, W. G., & Kjaer, K. 1998, "Detailed structure of molecularly thin polyelectrolyte multilayer films on solid substrates as revealed by neutron reflectometry", *Macromolecules*, vol. 31, no. 25, pp. 8893-8906

Lu, L. P. & Lin, X. Q. 2004, "Glassy carbon electrode modified with gold nanoparticles and DNA for the simultaneous determination of uric acid and norepinephrine under coexistence of ascorbic acid", *Analytical Sciences*, vol. 20, no. 3, pp. 527-530

Lu, X. L. & Mi, Y. L. 2005, "Characterization of the interfacial interaction between polyacrylamide and silicon substrate by Fourier transform infrared spectroscopy",

Macromolecules, vol. 38, no. 3, pp. 839-843

Lugtenberg, R. J. W., Egberink, R. J. M., van den Berg, A., Engbersen, J. F. J., & Reinhoudt, D. N. 1998, "The effects of covalent binding of the electroactive components in durable CHEMFET membranes - impedance spectroscopy and ion sensitivity studies", *Journal of Electroanalytical Chemistry*, vol. 452, no. 1, pp. 69-86

Makino, T., Inada, M., Umezu, I., & Sugimura, A. 2005, "Structural and optical properties of surface-hydrogenated silicon nanocrystallites prepared by reactive pulsed laser ablation", *Journal of Physics D-Applied Physics*, vol. 38, no. 18, pp. 3507-3511

Manalis, S. R., Cooper, E. B., Indermuhle, P. F., Kernen, P., Wagner, P., Hafeman, D. G., Minne, S. C., & Quate, C. F. 2000, "Microvolume field-effect pH sensor for the scanning probe microscope", *Applied Physics Letters*, vol. 76, no. 8, pp. 1072-1074

Maskos, U. & Southern, E. M. 1992, "Oligonucleotide Hybridizations on Glass Supports - A Novel Linker for Oligonucleotide Synthesis and Hybridization Properties of Oligonucleotides Synthesized Insitu", *Nucleic Acids Research*, vol. 20, no. 7, pp. 1679-1684

Micka, U., Holm, C., & Kremer, K. 1999, "Strongly charged, flexible polyelectrolytes in poor solvents: Molecular dynamics simulations", *Langmuir*, vol. 15, no. 12, pp. 4033-4044

Miyamoto, S. & Kollman, P. A. 1993, "Absolute and Relative Binding Free-Energy Calculations of the Interaction of Biotin and Its Analogs with Streptavidin Using Molecular-Dynamics Free-Energy Perturbation Approaches", *Proteins-Structure Function and Bioinformatics*, vol. 16, no. 3, pp. 226-245

Moiseev, L., Unlu, M. S., Swan, A. K., Goldberg, B. B., & Cantor, C. R. 2006, "DNA conformation on surfaces measured by fluorescence self-interference", *Proceedings of the National Academy of Sciences of the United States of America*, vol. 103, no. 8, pp. 2623-2628

Morrison, S. Roy1980"Electrochemistry at semiconductor and oxidized metal electrodes"New York ; London : Plenum, c1980

Mrksich, M., Sigal, G. B., & Whitesides, G. M. 1995, "Surface-Plasmon Resonance Permits In-Situ Measurement of Protein Adsorption on Self-Assembled Monolayers of Alkanethiolates on Gold", *Langmuir*, vol. 11, no. 11, pp. 4383-4385

Muller, Richard S., Kamins, Theodore I., and Chan, Mansun2003"Device electronics for integrated circuits
126"3rd ed[New York ; Chichester] : John Wiley & Sons

Neamen, Donald A.2003"Semiconductor physics and devices : Basic principles"3rd edBoston ; London : McGraw-Hill

Neff, P. A., Naji, A., Ecker, C., Nickel, B., von Klitzing, R., & Bausch, A. R. 2006,

"Electrical detection of self-assembled polyelectrolyte multilayers by a thin film resistor", *Macromolecules*, vol. 39, no. 2, pp. 463-466

Niemeyer, C. M., Ceyhan, B., Gao, S., Chi, L., Peschel, S., & Simon, U. 2001, "Site-selective immobilization of gold nanoparticles functionalized with DNA oligomers", *Colloid and Polymer Science*, vol. 279, no. 1, pp. 68-72

Niemeyer, C. M. & Simon, U. 2005, "DNA-based assembly of metal nanoparticles", *European Journal of Inorganic Chemistry* no. 18, pp. 3641-3655

Oehr, P., Westermann, J., & Biersack, H. J. 1988, "Streptavidin and Biotin As Potential Tumor Imaging Agents", *Journal of Nuclear Medicine*, vol. 29, no. 5, pp. 728-729

Offenhausser, A., Sprossler, C., Matsuzawa, M., & Knoll, W. 1997a, "Electrophysiological development of embryonic hippocampal neurons from the rat grown on synthetic thin films", *Neuroscience Letters*, vol. 223, no. 1, pp. 9-12

Offenhausser, A., Sprossler, C., Matsuzawa, M., & Knoll, W. 1997b, "Field-effect transistor array for monitoring electrical activity from mammalian neurons in culture", *Biosensors & Bioelectronics*, vol. 12, no. 8, pp. 819-826

Ohshima, H. & Kondo, T. 1988, "Double-Layer Interaction Regulated by the Donnan Potential", *Journal of Colloid and Interface Science*, vol. 123, no. 1, pp. 136-142

Ohtake, T., Hamai, C., Uno, T., Tabata, H., & Kawai, T. 2004a, "Immobilization of probe DNA on Ta2O5 thin film and detection of hybridized helix DNA using IS-FET", *Japanese Journal of Applied Physics Part 2-Letters & Express Letters*, vol. 43, no. 9A-B, p. L1137-L1139

Ohtake, T., Hamai, C., Uno, T., Tabata, H., & Kawai, T. 2004b, "Immobilization of probe DNA on Ta2O5 thin film and detection of hybridized helix DNA using IS-FET", *Japanese Journal of Applied Physics Part 2-Letters & Express Letters*, vol. 43, no. 9A-B, p. L1137-L1139

Oosawa, Fumio2001"Polyelectrolytes"Ann Arbor, Mich. : UMI Books on Demand

Penfold, J., Taylor, D. J. F., Thomas, R. K., Tucker, I., & Thompson, L. J. 2003, "Adsorption of polymer/surfactant mixtures at the air-water interface: Ethoxylated poly(ethyleneimine) and sodium dodecyl sulfate", *Langmuir*, vol. 19, no. 19, pp. 7740-7745

Perez-Luna, V. H., O'Brien, M. J., Opperman, K. A., Hampton, P. D., Lopez, G. P., Klumb, L. A., & Stayton, P. S. 1999, "Molecular recognition between genetically engineered streptavidin and surface-bound biotin", *Journal of the American Chemical Society*, vol. 121, no. 27, pp. 6469-6478

Peschel, S., Ceyhan, B., Niemeyer, C. M., Gao, S., Chi, L., & Simon, U. 2002, "Immobilization of gold nanoparticles on solid supports utilizing DNA hybridization",

Materials Science & Engineering C-Biomimetic and Supramolecular Systems, vol. 19, no. 1-2, pp. 47-50

Picart, C., Sengupta, K., Schilling, J., Maurstad, G., Ladam, G., Bausch, A. R., & Sackmann, E. 2004, "Microinterferometric study of the structure, interfacial potential, and viscoelastic properties of polyelectrolyte multilayer films on a planar substrate", *Journal of Physical Chemistry B*, vol. 108, no. 22, pp. 7196-7205

Piehler, J., Brecht, A., & Gauglitz, G. 1996, "Affinity detection of low molecular weight analytes", *Analytical Chemistry*, vol. 68, no. 1, pp. 139-143

Poghossian, A., Abouzar, M. H., Amberger, F., Mayer, D., Han, Y., Ingebrandt, S., Offenhausser, A., & Schoning, M. J. 2006a, "Field-effect sensors with charged macromolecules: characterisation by capacitance-voltage, constant-capacitance, impedance-spectroscopy and atomic-force microscopy methods", *Biosensors 2006* p. in press

Poghossian, A., Cherstvy, A., Ingebrandt, S., Offenhausser, A., & Schoning, M. J. 2005, "Possibilities and limitations of label-free detection of DNA hybridization with field-effect-based devices", *Sensors and Actuators B-Chemical*, vol. 111, pp. 470-480

Poghossian, A., Schumacher, K., Kloock, J. P., Rosenkranz, C., Schultze, J. W., Muller-Veggian, M., & Schoning, M. J. 2006b, "Functional testing and characterisation of ISFETs on wafer level by means of a micro-droplet cell", *Sensors*, vol. 6, no. 4, pp. 397-404

Pogorelova, S. P., Bourenko, T., Kharitonov, A. B., & Willner, I. 2002, "Selective sensing of triazine herbicides in imprinted membranes using ion-sensitive field-effect transistors and microgravimetric quartz crystal microbalance measurements", *Analyst*, vol. 127, no. 11, pp. 1484-1491

Pogorelova, S. P., Kharitonov, A. B., Willner, I., Sukenik, C. N., Pizem, H., & Bayer, T. 2004, "Development of ion-sensitive field-effect transistor-based sensors for benzylphosphonic acids and thiophenols using molecularly imprinted TiO2 films", *Analytica Chimica Acta*, vol. 504, no. 1, pp. 113-122

Pouthas, F., Gentil, C., Cote, D., & Bockelmann, U. 2004a, "DNA detection on transistor arrays following mutation-specific enzymatic amplification", *Applied Physics Letters*, vol. 84, no. 9, pp. 1594-1596

Pouthas, F., Gentil, C., Cote, D., Zeck, G., Straub, B., & Bockelmann, U. 2004b, "Spatially resolved electronic detection of biopolymers", *Physical Review e*, vol. 70, no. 3,

Purves, William K.2004"Life : the science of biology"7th edSunderland, Mass. ; Gordonsville, VA : Sinauer Associates, Inc. : W.H. Freeman & Co.

Radeva, Tsetska2001"Physical chemistry of polyelectrolytes"New York : Marcel Dekker

Riegler, H. & Essler, F. 2002, "Polyelectrolytes. 2. Intrinsic or extrinsic charge compensation? Quantitative charge analysis of PAH/PSS multilayers", *Langmuir*, vol. 18, no. 17, pp. 6694-6698

Roederer, J. E. & Bastiaans, G. J. 1983, "Microgravimetric Immunoassay with Piezoelectric-Crystals", *Analytical Chemistry*, vol. 55, no. 14, pp. 2333-2336

Rychlik, W. & Rhoads, R. E. 1989, "A Computer-Program for Choosing Optimal Oligonucleotides for Filter Hybridization, Sequencing and Invitro Amplification of Dna", *Nucleic Acids Research*, vol. 17, no. 21, pp. 8543-8551

Sakata, T., Kamahori, M., & Miyahara, Y. 2004, "Immobilization of oligonucleotide probes on Si3N4 surface and its application to genetic field effect transistor", *Materials Science & Engineering C-Biomimetic and Supramolecular Systems*, vol. 24, no. 6-8, pp. 827-832

Sakata, T., Kamahori, M., & Miyahara, Y. 2005a, "DNA analysis chip based on field-effect transistors", *Japanese Journal of Applied Physics Part 1-Regular Papers Short Notes & Review Papers*, vol. 44, no. 4B, pp. 2854-2859

Sakata, T. & Miyahara, Y. 2005b, "Potentiometric detection of single nucleotide polymorphism by using a genetic field-effect transistor", *Chembiochem*, vol. 6, no. 4, pp. 703-710

Sakkari, M. R.Dissertation, "Exploration of ISFET transfer-function for biochemical applications", Aachen University of Applied Sciences, Campus Juelich, Germany (2005)

Sallacan, N., Zayats, M., Bourenko, T., Kharitonov, A. B., & Willner, I. 2002, "Imprinting of nucleotide and monosaccharide recognition sites in acrylamidephenylboronic acid-acrylamide copolymer membranes associated with electronic transducers", *Analytical Chemistry*, vol. 74, no. 3, pp. 702-712

Schasfoort, R. B. M., Bergveld, P., Bomer, J., Kooyman, R. P. H., & Greve, J. 1989, "Modulation of the Isfet Response by An Immunological Reaction", *Sensors and Actuators*, vol. 17, no. 3-4, pp. 531-535

Schmitz, Kenneth S.1993"Macroions in solution and colloidal suspension"New York ; Cambridge : VCH

Schonhoff, M. 2003a, "Layered polyelectrolyte complexes: physics of formation and molecular properties", *Journal of Physics-Condensed Matter*, vol. 15, no. 49, p. R1781-R1808

Schonhoff, M. 2003b, "Self-assembled polyelectrolyte multilayers", *Current Opinion in Colloid & Interface Science*, vol. 8, no. 1, pp. 86-95

Shin, J. K., Kim, D. S., Park, H. J., & Lim, G. 2004, "Detection of DNA and protein molecules using an FET-type biosensor with gold as a gate metal", *Electroanalysis*, vol. 16, no. 22, pp. 1912-1918

Shirai, K., Yoshida, Y., Nakayama, Y., Fujitani, M., Shintani, H., Wakasa, K., Okazaki, M., Snauwaert, J., & Van Meerbeek, B. 2000, "Assessment of decontamination methods as pretreatment of silanization of composite glass fillers", *Journal of Biomedical Materials Research*, vol. 53, no. 3, pp. 204-210

Shiratori, S. S. & Rubner, M. F. 2000, "pH-dependent thickness behavior of sequentially adsorbed layers of weak polyelectrolytes", *Macromolecules*, vol. 33, no. 11, pp. 4213-4219

Shockley, W.1950"Electrons and holes in semiconductors: with applications to transistor electronics"Princeton, N.J. ; London : Van Nostrand, [1950]

Sigal, G. B., Bamdad, C., Barberis, A., Strominger, J., & Whitesides, G. M. 1996, "A self-assembled monolayer for the binding and study of histidine tagged proteins by surface plasmon resonance", *Analytical Chemistry*, vol. 68, no. 3, pp. 490-497

Silberzan, P., Leger, L., Ausserre, D., & Benattar, J. J. 1991, "Silanation of Silica Surfaces - A New Method of Constructing Pure Or Mixed Monolayers", *Langmuir*, vol. 7, no. 8, pp. 1647-1651

Souteyrand, E., Cloarec, J. P., Martin, J. R., Wilson, C., Lawrence, I., Mikkelsen, S., & Lawrence, M. F. 1997, "Direct detection of the hybridization of synthetic homo-oligomer DNA sequences by field effect", *Journal of Physical Chemistry B*, vol. 101, no. 15, pp. 2980-2985

Souteyrand, E., Martin, J. R., & Martelet, C. 1994, "Direct-Detection of Biomolecules by Electrochemical Impedance Measurements", *Sensors and Actuators B-Chemical*, vol. 20, no. 1, pp. 63-69

Sprossler, C., Richter, D., Denyer, M., & Offenhausser, A. 1998, "Long-term recording system based on field-effect transistor arrays for monitoring electrogenic cells in culture", *Biosensors & Bioelectronics*, vol. 13, no. 6, pp. 613-618

Sproull, Robert L. and Phillips, W. Andrew1990"Modern physics : the quantum physics of atoms, solids, and nuclei"Reprint edMalabar, Fla : R.E. Krieger Pub. Co

Star, A., Gabriel, J. C. P., Bradley, K., & Gruner, G. 2003, "Electronic detection of specific protein binding using nanotube FET devices", *Nano Letters*, vol. 3, no. 4, pp. 459-463

Steitz, R., Leiner, V., Siebrecht, R., & von Klitzing, R. 2000, "Influence of the ionic strength on the structure of polyelectrolyte films at the solid/liquid interface", *Colloids and Surfaces A-Physicochemical and Engineering Aspects*, vol. 163, no. 1, pp. 63-70

Strother, T., Hamers, R. J., & Smith, L. M. 2000, "Covalent attachment of oligodeoxyribonucleotides to amine-modified Si (001) surfaces", *Nucleic Acids Research*, vol. 28, no. 18, pp. 3535-3541

Sukhorukov, G. B., Mohwald, H., Decher, G., & Lvov, Y. M. 1996, "Assembly of polyelectrolyte multilayer films by consecutively alternating adsorption of polynucleotides

and polycations", *Thin Solid Films*, vol. 285, pp. 220-223

Sun, Q., Yao, K. H., Gatos, H. C., & Lagowski, J. 1992, "Effects of Nitrogen on Oxygen Precipitation in Silicon", *Journal of Applied Physics*, vol. 71, no. 8, pp. 3760-3765

Swan, A. K., Moiseev, L. A., Cantor, C. R., Davis, B., Ippolito, S. B., Karl, W. C., Goldberg, B. B., & Unlu, M. S. 2003, "Toward nanometer-scale resolution in fluorescence microscopy using spectral self-interference", *Ieee Journal of Selected Topics in Quantum Electronics*, vol. 9, no. 2, pp. 294-300

Takafuji, M., Ide, S., Ihara, H., & Xu, Z. H. 2004, "Preparation of poly(1-vinylimidazole)-grafted magnetic nanoparticles and their application for removal of metal ions", *Chemistry of Materials*, vol. 16, no. 10, pp. 1977-1983

Tanford, Charles1961"Physical chemistry of macromolecules"New York ; London : John Wiley

Tsuruta, H., Matsui, S., Hatanaka, T., Namba, T., Miyamoto, K., & Nakamura, M. 1994, "Detection of the Products of Polymerase Chain-Reaction by An Elisa System Based on An Ion Sensitive Field-Effect Transistor", *Journal of Immunological Methods*, vol. 176, no. 1, pp. 45-52

Uno, T., Ohtake, T., Tabata, H., & Kawai, T. 2004, "Direct deoxyribonucleic acid detection using ion-sensitive field-effect transistors based on peptide nucleic acid", *Japanese Journal of Applied Physics Part 2-Letters & Express Letters*, vol. 43, no. 12B, p. L1584-L1587

Uslu, F.Dissertation, "Untersuchungzen zum elektronischen-Nachweis der DNA-Hybridisierung", Techischen Hochschule Aachen (2003)

Uslu, F., Ingebrandt, S., Mayer, D., Bocker-Meffert, S., Odenthal, M., & Offenhausser, A. 2004, "Labelfree fully electronic nucleic acid detection system based on a field-effect transistor device", *Biosensors & Bioelectronics*, vol. 19, no. 12, pp. 1723-1731

vanHal, R. E. G., Eijkel, J. C. T., & Bergveld, P. 1996, "A general model to describe the electrostatic potential at electrolyte oxide interfaces", *Advances in Colloid and Interface Science*, vol. 69, pp. 31-62

Wang, J. & Bard, A. J. 2001, "Monitoring DNA immobilization and hybridization on surfaces by atomic force microscopy force measurements", *Analytical Chemistry*, vol. 73, no. 10, pp. 2207-2212

Watson, J. D. & Crick, F. H. C. 1953, "Molecular Structure of Nucleic Acids - A Structure for Deoxyribose Nucleic Acid", *Nature*, vol. 171, no. 4356, pp. 737-738

Watts, John F. and Wolstenholme, John2003"An introduction to surface analysis by XPS and AES"Chichester : John Wiley

Weber, P. C., Ohlendorf, D. H., Wendoloski, J. J., & Salemme, F. R. 1989, "Structural Origins of High-Affinity Biotin Binding to Streptavidin", *Science*, vol. 243, no. 4887, pp. 85-88

Witucki, G. L. 1993, "A Silane Primer - Chemistry and Applications of Alkoxy Silanes", *Journal of Coatings Technology*, vol. 65, no. 822, pp. 57-60

Wroblewski, W., Mirzynska, B., & Brzozka, Z. 1996, "Field effect transistors (FETs) as transducers in electrochemical sensors", *Chemia Analityczna*, vol. 41, no. 4, pp. 697-706

Xu, X. H. & Bard, A. J. 1995, "Immobilization and Hybridization of Dna on An Aluminum(Iii) Alkanebisphosphonate Thin-Film with Electrogenerated Chemiluminescent Detection", *Journal of the American Chemical Society*, vol. 117, no. 9, pp. 2627-2631

Xu, X. H., Yang, H. C., Mallouk, T. E., & Bard, A. J. 1994, "Immobilization of Dna on An Aluminum(Iii) Alkanebisphosphonate Thin-Film with Electrogenerated Chemiluminescent Detection", *Journal of the American Chemical Society*, vol. 116, no. 18, pp. 8386-8387

Yates, D. E., Levine, S., & Healy, T. W. 1974, "Site-Binding Model of Electrical Double-Layer at Oxide-Water Interface", *Journal of the Chemical Society-Faraday Transactions I*, vol. 70, pp. 1807-1818

Yeow, T. C. W., Haskard, M. R., Mulcahy, D. E., Seo, H. I., & Kwon, D. H. 1997, "A very large integrated pH-ISFET sensor array chip compatible with standard CMOS processes", *Sensors and Actuators B-Chemical*, vol. 44, no. 1-3, pp. 434-440

Zayats, M., Kharitonov, A. B., Katz, E., & Willner, I. 2001, "An integrated relay/nitrate reductase field-effect transistor for the sensing of nitrate (NO3-)", *Analyst*, vol. 126, no. 5, pp. 652-657

Zayats, M., Lahav, M., Kharitonov, A. B., & Willner, I. 2002a, "Imprinting of specific molecular recognition sites in inorganic and organic thin layer membranes associated with ion-sensitive field-effect transistors", *Tetrahedron*, vol. 58, no. 4, pp. 815-824

Zayats, M., Raitman, O. A., Chegel, V. I., Kharitonov, A. B., & Willner, I. 2002b, "Probing antigen-antibody binding processes by impedance measurements on ion-sensitive field-effect transistor devices and complementary surface plasmon resonance analyses: Development of cholera toxin sensors", *Analytical Chemistry*, vol. 74, no. 18, pp. 4763-4773

Zazzera, L. & Evans, J. F. 1993, "In-Situ Internal-Reflection Infrared Study of Aqueous Hydrofluoric-Acid and Ultraviolet Ozone Treated Silicon(100) Surfaces", *Journal of Vacuum Science & Technology A-Vacuum Surfaces and Films*, vol. 11, no. 4, pp. 934-939

Zisman, William A., Fowkes, Frederick M., Kendall, Award Symposium, American Chemical Society.Division of Colloid and Surface Chemistry, and American Chemical Society.1964"Contact angle, wettability and adhesion : the Kendall award symposium honoring William A. Zisman, sponsored by the Division of Colloid and Surface Chemistry,

at the 144th Meeting of the American Chemical Society, Los Angeles, Calif., April 2-3, 1963"Washington, [D.C.] : American Chemical Society

PUBLICATIONS

1. Detection of DNA hybridization by a field-effect transistor with covalently attached catcher molecules, **Y. Han**, A. Offenhäusser, S. Ingebrandt, Surface and Interface Analysis, 2006 vol. 38, no. 4, pp. 176-181
2. Surface activation of thin silicon oxides by wet cleaning and silanization, **Y. Han**, D. Mayer, A. Offenhäusser, S. Ingebrandt, Thin Solid Films, 2006 no. 510, pp. 175-180
3. Electronic Detection of Nucleic Acid Molecules with a Field-Effect Transistor, S. Ingebrandt, **Y. Han**, M.-R. Sakkari, R. Stockmann, O. Belinskyy, and A. Offenhäusser, Proceedings of the MRS 2004 Fall Meeting, Semiconductor Materials for Sensing, ed. S. Seal, M.-I. Baraton, C. Parrish, and N. Murayama Mater. Res. Soc. Symp. Proc. 828, Warrendale, PA , 2005, A6.9.
4. Detection of layer-by-layer adsorbed polyelectrolytes by means of field-effect-based capacitive EIS structures, T. Kassab, **Y. Han**, A. Poghossian, S. Ingebrandt, A. Offenhäusser, M.J. Schöning, Biomedizinische Technik, 49 (2),2004, 1034.
5. Fully Electronic Detection of Nucleic Acid Molecules with a Field-Effect Transistor Array, S. Ingebrandt, **Y. Han**, O. Belinskyy, F. Uslu, A. Offenhäusser, Biomedizinische Technik, 49 (2), 2004, 1002.
6. Markierungsfreie DNA-Detektion mit silizium-Feldeffektsensoren-Messeffekte oder Artefakte?, Micheal J.Schöning, Marzam H. Abouzar, **Yinhua Han**, Sven Ingebrandt, Andereas offenhäusser, Arshak Poghossian, 13. ITG-/GMA-Fachtagung Sensoren und Messsysteme 2006, Freiburg/Breisgau, 13th-14th March, 2006
7. Synthesis and luminescent properties of europium (III) schiff base complexes covalently bonded to silica xerogels, Yan Luo, **Yinhua Han**, Jun Lin, Journal of luminescence, 2006, in press
8. Luminescence and energy transfer of organically modified silica xerogels (OMSX) doped and undoped with Eu^{3+} and Tb^{3+}, **Yinhua Han**, Jun Lin, Journal of Solid State Chemistry, 171 (2003) 396–400
9. Photoluminescence of organic-inorganic hybrid SiO_2 xerogels, **Yinhua Han**, Jun Lin, Hongjie Zhang, Materials Letters, 54 (2002) ,389-396
10. The research on the luminescence properties of SiO_2 xerogels, **HAN Yinhua**, LIN Jun, Chinese Journal of Luminescence, 2002, 23(3)296-300
11. Photoluminescence of Silica gel, **HAN Yinhua**, LIN Jun, ZHANG Hongjie, Chinese Chemistry Online, 2001,64(7),
12. Process in luminescent films prepared by sol-gel process, Lin Jun, Pang Mao-lin, **Han Yin-hua**, et al., Chinese Journal of Inorganic Chemistry, 2001,17(2), 153-160
13. Reducing the value of COD in slop using modified bauxite, **Han Yinhua**, Mao Shizhong, Zheng Songzhi, Chinese Journal of Changchun University of Science and Technology, 30, SUP. 2000,68-70

Forschungszentrum Jülich
in der Helmholtz-Gemeinschaft

50 Jahre / Zukunft

Jül-4227
August 2006
ISSN 0944-2952